Airfoil separation control using tension-activated kirigami metasurfaces

An exploratory aerodynamic investigation into the art of kirigami

Master Thesis of Aerospace Engineering

E.S.J. Overbosch

Delft University of Technology

Airfoil separation control using tension-activated kirigami metasurfaces

An exploratory aerodynamic investigation into the art of kirigami

by

E.S.J. Overbosch

Student Name	Student Number
E.S.J. Overbosch	XXXXXXX

Instructor: T. Michelis
Faculty: Faculty of Aerospace Engineering - Flow physics & technology

”There is no royal road to science, and only those who do not dread the fatiguing climb of its steep paths have a chance of gaining its luminous summits.”

Karl Marx

Preface

This thesis marks the conclusion of a long period of learning at Delft University of Technology. Having done both my bachelor's degree and my master's degree, it has been an incredible journey full of learning on a personal level, and even more full of learning on an academic level (though, nowhere near enough to satisfy my curiosity). From learning the ins-and-outs of aircraft design, to diving deep into all the niches of fluid dynamics, to writing the most outlandish scripts in various programming languages, I relished every second of it. If there is one lesson that stood out above all, is that learning never stops, nor do I ever hope it will.

The hard work that culminated in to the present work did not manifest in a mere vacuum. It is through the inspiration, dedication and support of the people around me that truly led to the completion of this Master's degree. People who deserve so much more praise than the acknowledgements made on this page, but for now, this will have to do.

For this, I would first like to express my gratitude to the professors and supervisors that taught me along the way, but in particular to my thesis supervisor Dr. Theo Michelis who, despite his eternally full plate of work as a professor, always manages to find the time to help out and advise his students, making efforts to stay involved with their projects and to shape understanding of the ~~subjects under his rule~~, students under his guidance. Evidently, he also instills a healthy dose of sarcasm in each of them. In summary, his approachability and cooperative, supervision style has been instrumental in maintaining motivation and inspiration throughout the thesis project. His skills as both a supervisor and an educator come highly recommended.

This appreciation further extends to the rest of the people at the low-speed lab. With an incredibly friendly and approachable culture, there was always a professor, lab technician, researcher, PhD, or fellow master student that was able and willing to lend a hand. I have rarely seen a working environment with such knowledgeable and passionate, yet down-to-earth people. I am particularly grateful for all the fellow students in the master thesis room, who always provided plenty of distraction and conversation whenever focus ran out on a sunny friday afternoon.

Having mentioned the tremendous personal growth, this particular challenge might have seemed insurmountable at times were it not for the group of people that were there along the way. To my friends from my study, the university and beyond, I owe you for the relentless passion you have shown me in whatever you do, given the tremendous inspirational effect it has had on me. Having people around with which I could share a mutual passion for all things engineering, mathematics, science, and programming was a tremendous driving force to keep exploring, to keep learning, to keep challenging myself on both an academic level and personal level, helping me persevere through every setback. You have shown me that doing justice to curiosity is useful, rewarding and, god forbid, fun.

Lastly, to all my close friends, from the Netherlands to Yorkshire, from Austria to Hungary, and every other corner of Europe who I have celebrated with, debated with, laughed with and confided in: I am endlessly grateful for your compassion and friendship and hope to keep it up for years to come. To my girlfriend, and my family; my brother, sister, mum and dad, I am eternally indebted for their unconditional love and support. It has been a privilege growing up with you. You have all inspired me with your individuality, unique attitudes and fierce determination in staying true to yourself and the values you believe in.

Abstract

Passive turbulent separation control methods are often associated with additional parasitic drag. Kirigami metasurfaces provide potential for a deployable device that exhibits out-of-plane deformation upon in-plane extension, resulting a full 3D geometry. Following a literature survey, it was found that the use of kirigami in flow control is not widely studied, and requires further attention. The present thesis investigates the structural design requirements of a kirigami flow control device, and explores its effectiveness as a turbulent separation control device on a wind turbine airfoil in a wind tunnel.

The kirigami was designed using a FEM model, which was validated using laser scans of a vinyl-cut kirigami model. A strong agreement was found between the FEM and the laser scans in the deployment height of the kirigami under various in-plane extensions. In accordance with findings from literature, this also highlighted non-uniformity effects in the kirigami. These were alleviated using rounded rectangular cut-outs in the strips on each end of the kirigami device. A final kirigami design was formulated for the wind tunnel set-up with a deployment height of $1.4mm$, matching the height scale of sub-BL-scale vortex generators ($h/\delta = 0.1 - 0.3$). When deployed, the kirigami design covers the airfoil from $x/c = 0.55$ to 0.7. Two devices were tested using these parameters: one with a circular reference shape and one with a triangular reference shape.

The kirigami was tested on a 2D wing with a DU96 airfoil in an open-jet wind tunnel. The airfoil was varied from 6 to 20 degrees in steps of 2, each setting measured at freestream velocities from $10m/s$ to $30m/s$ in steps of 5. The flow characteristics of the trailing-edge separation region were measured using 2D planar PIV, measured on the centreline of the 2D wing, along with pressure probes spaced along the chord on the wing surface. The experiment revealed that the effect of the kirigami device on the separation region strongly depends on angle of attack. At low angles (6-10°), kirigami aggravated separation, leading to both increased reverse flow intensity as well as an increased size of the separation region. At 12 and 14°, the kirigami was successful in reducing separation, leading to reduced reverse flow, a smaller separation region, as well as reduced backflow. At higher angles of attack, the kirigami was fully submerged in the separation region ($h/\delta = 0.05$), and its effects on the flow vanished. The data of the separation controlled cases were indicative of significant reductions in drag, with the relative momentum deficit in the wake being reduced by up to 7%. The lift remained unaffected as no significant modifications to the pressure distribution were observed under the influence of the kirigami.

Observation of data concluded that the kirigami does not enhance mixing in the boundary layer, so the device does not function as a vortex generator. Instead, it was theorised that the kirigami functions as a blockage for the flow near the surface, leading to local favourable pressure gradients. An alternative theory was that the kirigami could function using a 'roller-bearing' flow effect that eliminates the zero-slip boundary condition on the flow over the kirigami. However, no evidence was found for either of these theories. Instead, a more plausible theory is that the kirigami functions as a reistance to the backflow near the surface, leading to reduced momentum transfer upstream.

Contents

Nomenclature

Abbreviations

Abbreviation	Definition
AoA	Angle of Attack
APG	Adverse Pressure Gradient
BL	Boundary Layer
FEM	Finite-Element Method
FOV/FoV	Field of View
PIV	Particle Image Velocimetry
RANS	Reynolds-Averaged Navier-Stokes
TBL	Turbulent Boundary Layer
VG	Vortex Generator
ZPG	Zero Pressure Gradient

Symbols

Symbol	Definition	Unit
B	Logarithmic wall law parameter	[-]
C_{l_α}	Lift curve slope	[-]
c	Chord length	[m]
c	Kirigami strip length	[m]
c_s	Kirigami strip cut edge distance	[m]
D	Drag	[N]
E	Young's Modulus	[Pa]
e	Vortex generator device length	[-]
$f_{\#}$	Aperture	[m]
H	Shape factor	[-]
h	Laser scanner height	[m]
h	Vortex generator/kirigami device height	[m]
k_s	Equivalent sand grain roughness	[m]
k_s^+	Roughness Reynolds number	[-]
L	Aerodynamic reference length scale	[m]
L	Vortex generator pair intermediate spacing	[m]
L_x	Kirigami element horiztonal width	[m]
L_y	Kirigami element horiztonal width	[m]
M	Distance from the wall to maximum RMS velocity fluctuations	[m]
N	Ensemble size	[-]
N	Number of laser scan profiles	[-]
N_x	Number of kirigami element pairs in x	[-]
N_y	Number of kirigami element pairs in y	[-]
n	Surface-normal coordinate	[m]
p	Static pressure	[kg/m^2]
p_0	Total pressure	[kg/m^2]
p_e	Boundary layer edge static pressure	[kg/m^2]
R_{ij}	Reynolds stress with components i and j	[m^2/s^2]

Symbol	Definition	Unit
Re	Reynolds number	[-]
r_s	Kirigami strip cut corner radius	[m]
s	Surface-aligned coordinate	[m]
t	Time	[s]
Δt	Frame separation	[s]
U	Flow velocity	[m/s]
U_e	Boundary layer edge velocity	[m/s]
U_0	Outer layer mean velocity	[m/s]
U_∞	Freestream velocity	[m/s]
u_e	Exit velocity at the control volume boundary	[m/s]
u_n	Velocity component along surface-normal coordinate n	[m/s]
u_s	Velocity component along surface-aligned coordinate s	[m/s]
u^+	Velocity in wall coordinates	[-]
u_σ	Uncertainty velocity at 1σ	[m/s]
u_τ	Friction velocity	[m/s]
v	y-component of velocity	[m/s]
v^*	Friction velocity (alternative)	[-]
w_s	Kirigami element slit width	[m]
ΔX_{VG}	Streamwise distance between VG device and baseline separation	[m]
x_{sep}	Separation point	[m]
x_{probe}	Wake measurement location	[m]
y^+	Wall distance in wall coordinates	[-]
Δy	Kirigami device extension	[m]
z_{max}	Maximum deployment height on the centreline of the kirigami device	[-]
Δz	Spanwise VG device spacing	[m]
α	Geometric angle of attack	[rad]
α_{eff}	Effective angle of attack	[rad]
α_{geom}	Geometric angle of attack	[rad]
β	Clauser pressure gradient parameter	[-]
β	Vortex generator device angle	[deg]
ε_x	Mechanical strain in x	[-]
ε_y	Mechanical strain in y	[-]
γ	Kirigami cut angle	[rad]
γ_{pu}	Backflow coefficient in x-direction	[-]
γ_{pv}	Backflow coefficient in y-direction	[-]
Γ	Circulation	[m^2/s]
Δ_x	Kirigami strip cut gap in x	[m]
Δ_x	Kirigami strip cut gap in y	[m]
δ	Boundary layer thickness	[m]
δ_x	Kirigami element spacing in x	[m]
δ_y	Kirigami element spacing in y	[m]
δ_ω	Shear layer thickness (based on vorticity)	[m]
δ^*	Displacement thickness	[m]
δ_{99}	Boundary layer thickness (99% velocity cond.)	[m]
θ	FOV angle w.r.t. tunnel	[rad]
θ	Momentum thickness	[m]
κ	Logarithmic wall law parameter	[-]
μ	Dynamic viscosity	[kg/(ms)]
μ	Mean	
ξ	AoA correction factor	[-]

Symbol	Definition	Unit
Π_{wake}	Amount of momentum in the wake measured at x_{probe}	[kg m^2/s^2]
ρ	Density	[kg/m^3]
σ	Normal stress	[Pa]
σ	Standard deviation	[Pa]
τ	Viscous shear stress	[kg/m^2]
τ_w	Viscous wall shear stress	[kg/m^2]
ν	Kinematic viscosity	[m^2/s]
ν	Poisson ratio	[-]
ϕ	FOV angle w.r.t. airfoil	[rad]
χ	Backflow coefficient	[-]
χ_0	Reference backflow coefficient	[-]
ω_n	Shear stress with respect to surface-normal coordinate	[1/s]

1

Introduction

Flow separation is one of the most fundamental themes in the field of aerodynamics. This viscous phenomenon's effects on a flow regime are drastic, and the presence of flow separation in the physical world is near enough universal. First properly studied in the 20th century, [1] this phenomenon plays a crucial, yet typically undesirable, role in modern technology. Flow separation phenomena pose a limitation in the upscaling of wind energy for the energy transition [2]. It is also the physical mechanism behind the majority of cases of in-flight loss of control (LOC-I), which is by far the leading cause of fatal accidents in general aviation [3]. However, its relevance also goes back to ancient technology and daily life objects: flow separation is, for example, instrumental in the functioning of a teapot spout [4].

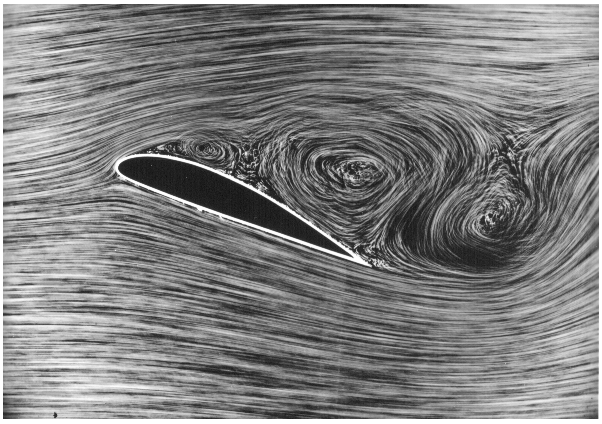

Figure 1.1: Flow separation in action: streamlines stop following the surface and break away (Photo by DLR, 1915)[1]

In aircraft design, flow separation limits the lift over an airplane wing, which in turn drives performance parameters such as maximum take-off weight, controllability and general safety. An example of what flow separation looks like over an aircraft wing is shown in Figure 1.1[1]. In the automotive industry, minimising flow separation is instrumental in reducing drag and/or increasing downforce. [5]. Drag on road vehicles directly impacts fuel economy [6], which further illustrates how intrinsic yet constricting the concept of flow separation is in design problems. It is therefore only natural that extensive research efforts have been, and are still being put towards controlling and delaying flow separation.

The most classic example of separation control, in the form of vortex generators, was fashioned just after world war II by Taylor [7], who showed that flow separation in diffusers can be reduced by applying vortex generators. Further applications include delaying separation to enhance aircraft wing lift, adapt flow properties to manage wing-buffet, and reduce afterbody drag of aircraft fuselages [8]. Figure 1.2[2]

---

[1] https://upload.wikimedia.org/wikipedia/commons/f/f2/1915ca_abger_fluegel_%28cropped_and_mirrored%29.jpg

[2] https://www.aopa.org/news-and-media/all-news/2017/august/flight-training-magazine/vortex-generators

shows an example of these vortex generators on an aircraft wing. The drawback of vortex generators is that they generate additional parasitic drag. Furthermore, vortices break down after time into complex flow structures [9]. As a consequence, such devices are not universally applicable in flows involving separation, but are instead the subject of broader trade-offs in the product's performance during the design phase.

Figure 1.2: Vortex generators on the leading edge of an aircraft wing[2]

To mitigate this issue, a deployable variation of separation control might be preferable. As an application in aircraft design, for example, this would allow the pilot or aircraft control systems to extend and retract the vortex generators on the wing, such that these devices are only active during critical phases of flight (take-off and landing), or to generally combat stall. Relevant research campaigns have already occurred to this end [10], but generally come with major drawbacks involving the actuation of these devices in the form of technical complexity, weight and structural compromise.

This issue might be tackled by using tension-activated kirigami metasurfaces. This novel concept involves applying a tension load to a 2D sheet with specifically defined slots cut out, so as to create out-of-plane deformations, resulting in a full 3D geometry. These devices provide a particularly appealing opportunity for flow control due to the significantly simplified actuation mechanism. At first glance, one might immediately see the resemblance between this geometry and shark scales, or an array of vortex generators. In fact, several scientific studies have already been done in the field of kirigami-based flow control. However, the coverage of these studies is limited, and significant knowledge gaps need to be bridged before these can be applied in practice. The present research aims to contribute to this field and lay the groundwork for further studies in kirigami separation control.

This thesis will set out to investigate how effective a specific type of tension activated kirigami sheet is at statically controlling the flow separation on a lifting surface from a flow physics perspective. This will be done by designing an experiment based on the identification of knowledge gaps in a literature study. This literature study is done in chapter 2. This is followed by a research plan in chapter 3 based on the literature findings from the preceding chapter. Then, a chapter follows on the structural design of kirigami devices for flow control in chapter 4. The actual aerodynamic experiment is set-up and discussed in chapter 5. The conclusions to the research can be found in the final chapter, chapter 6.

2

Background

Origami (折り紙) is the art of paper folding. The word comes from the Japanese Ori, meaning folding, and Kami (paper). Although it is famously a Japanese tradition, its origin dates back to 7th century China. A more versatile variation of Origami is kirigami (切り紙), which is the art of both cutting and folding paper (kiri meaning ”to cut”). Whereas Origami only allows folding of the sheet, kirigami also involves cutting to create more complex geometry. Both techniques can be used to create artworks, such as those in Figure 2.1a[1] and Figure 2.1b [2].
The use of kirigami in engineering is a relatively novel idea, with research papers only emerging in the late 2000s. The geometric concept has since spread into a wide range of topics, including solar power, optics, ventilation, novel structural applications and several more[11][12][13] [14][15][16]. However, kirigami is still a foreign concept within the field of aerodynamics. Before analysing how it might be used in aerodynamics, an understanding of what kirigami encompasses and how it works is required. This chapter will present the necessary background on kirigami, including different types and the structural mechanics behind it.

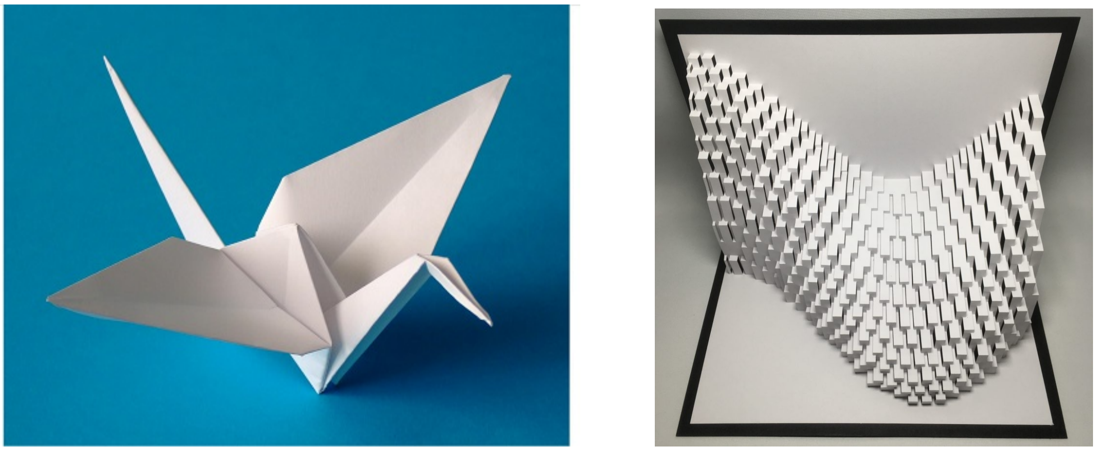

(a) Origami[1] **(b)** kirigami[2]

Figure 2.1: Examples of art in Origami and kirigami

2.1. Types of kirigami

In engineering research, parallels are often drawn between kirigami and meta-materials, in the sense that they both exhibit structural/material properties that could otherwise not be found in nature. One such property in particular that is of interest in aerodynamic control are geometric changes of a thin

---

[1] https://www.librarieshawaii.org/event/make-your-own-origami-cranes/

[2] https://mag.lexus.co.uk/kirigami-7-amazing-artworks-made-entirely-from-paper/

sheet under load. These properties do not necessarily represent material properties, so in literature, the term ”Metasurface” is typically more common. Adapting these behaviours could be done in a way that involves in-plane deformations [17], as shown in Figure 2.2. However, these have limited potential in the context of turbulent separation control.

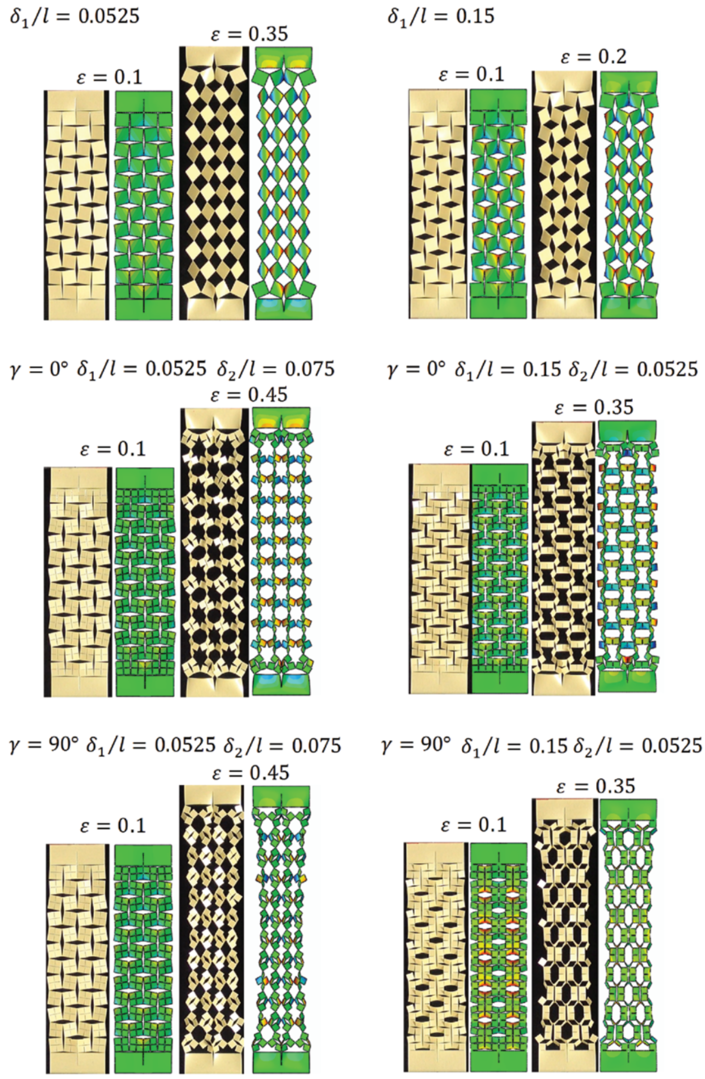

Figure 2.2: Extension of various 2D kirigami patterns [17]

What is more interesting is the option for out-of-plane deformations in kirigami. This can be achieved through buckling of elements in the surface created by staggered cut patterns. By using a slit-pattern, the individual elements buckle and rotate to form arch patterns under in-plane tension, as shown in Figure 2.3. With additional cuts, these can be fully extended to turn the sheet into a honeycomb structure [18]. These patterns are more interesting for aerodynamic flow control. Gamble et al. [19] have already attempted to use this slit pattern to control flow over an airfoil with limited results.

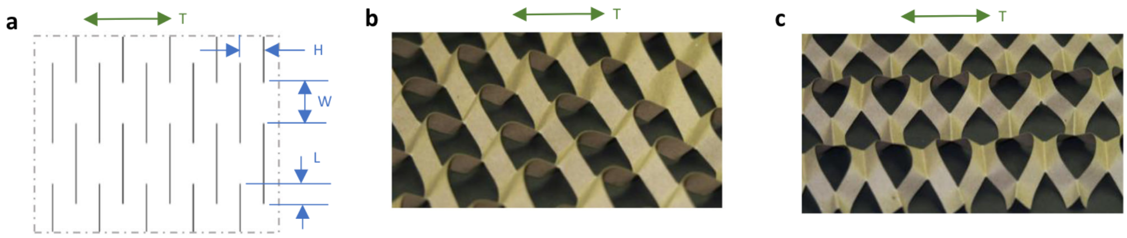

Figure 2.3: Linear cut/slit pattern kirigami [18]

Certain symmetric thin shapes can also result in out-of-plane deformations under load. Triangular cut patterns, trapezoids or arcs result in more defined, scale-like protrusions under tension, as shown in Figure 2.4. This mechanism has been studied under various applications in science, such as actuated crawl and shoe grips [20] [21]. This geometry has also been researched as flow control for a shedding cylinder [22].

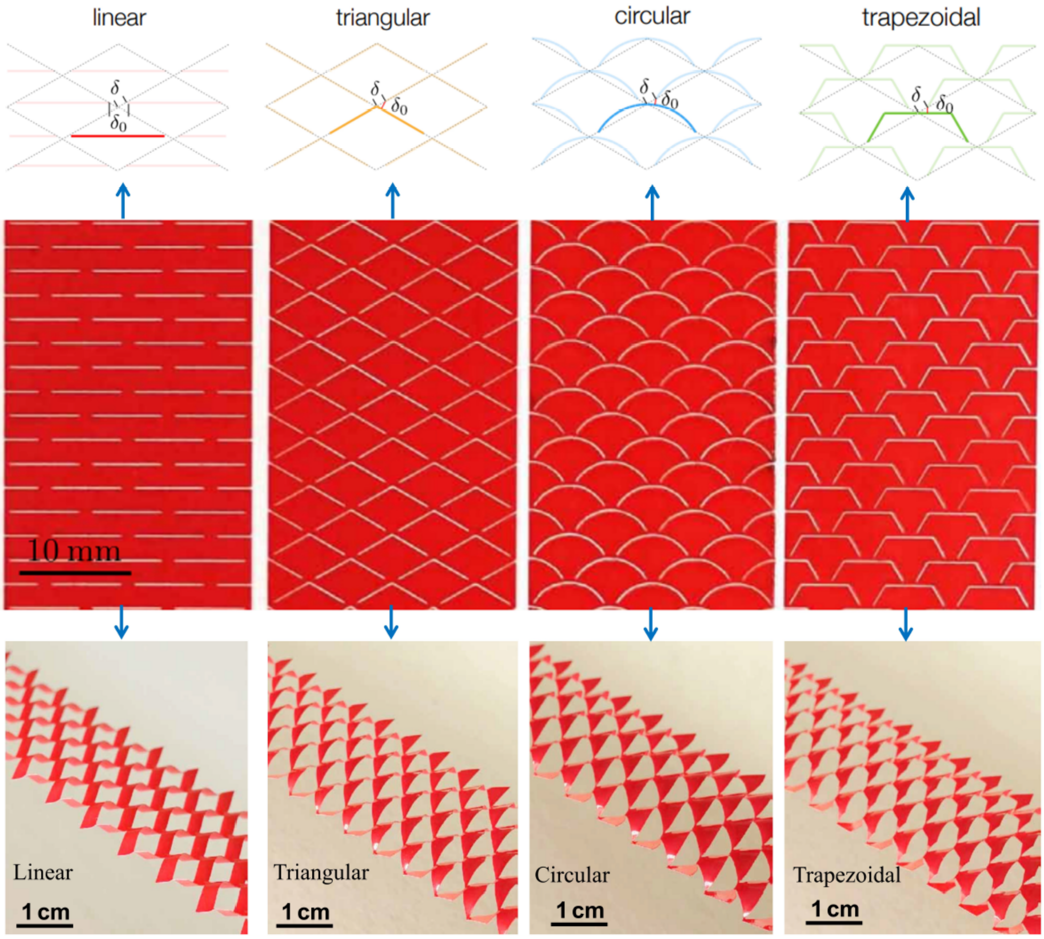

Figure 2.4: Symmetric kirigami cut patterns [20]

2.2. Structural mechanics of kirigami

The structural mechanics of kirigami metasurfaces is quite complex, and involves non-linear structural effects. However, Amin [23] provides a simplified explanation based on linear mechanics.
Figure 2.5 shows the stress distribution around a linear slit discontinuity in a thin sheet [24]. Right next to the discontinuity, strong compression stresses are found. Amin models the kirigami surface right next to the discontinuity as a thin beam in compression, and shows that a thin structure such as this is far

more likely to buckle under compression than to display linear compression [23]. The reason given for this is that the bending energy for a thin structure under compression is much lower than the stretching energy.

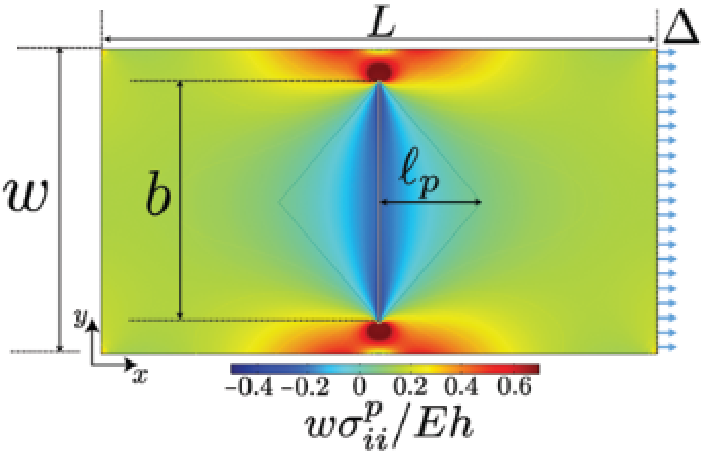

Figure 2.5: Stress distribution around a slit discontinuity in a thin sheet [24]

Thus, the main structural mechanism that allows 3D kirigami elements to appear is transverse buckling next to the material discontinuity due to transverse compressive stresses that emerge under sheet tension. This mechanism relies on the assumption that the bending energy is much greater than the stretching energy [23]. This requires the material to be thin, and that there are no other contributions that affect the behaviour of the bending energy.

When properly designed, the out-of-plane deformation of kirigami elements is bistable, also known as ”snap-through” behaviour [25]. It is therefore not guaranteed that all kirigami elements pop out in the same direction. This is an important aspect for the design of kirigami elements, as having a uniform pop-up direction is necessary. Two methods to guarantee this is either to apply an initial load in the desired direction [26], or through material imperfections or intentional asymmetries on one side of the material [23] [27].

One noteworthy aspect of these kirigami devices is that they do not deploy completely uniformly, particularly near the start and end of the device. Figure 2.6 shows an undeployed triangular front appearing at the top and bottom boundaries of the device. This has significance as, for aerodynamic applications, deployment that approaches uniformity is more desirable.

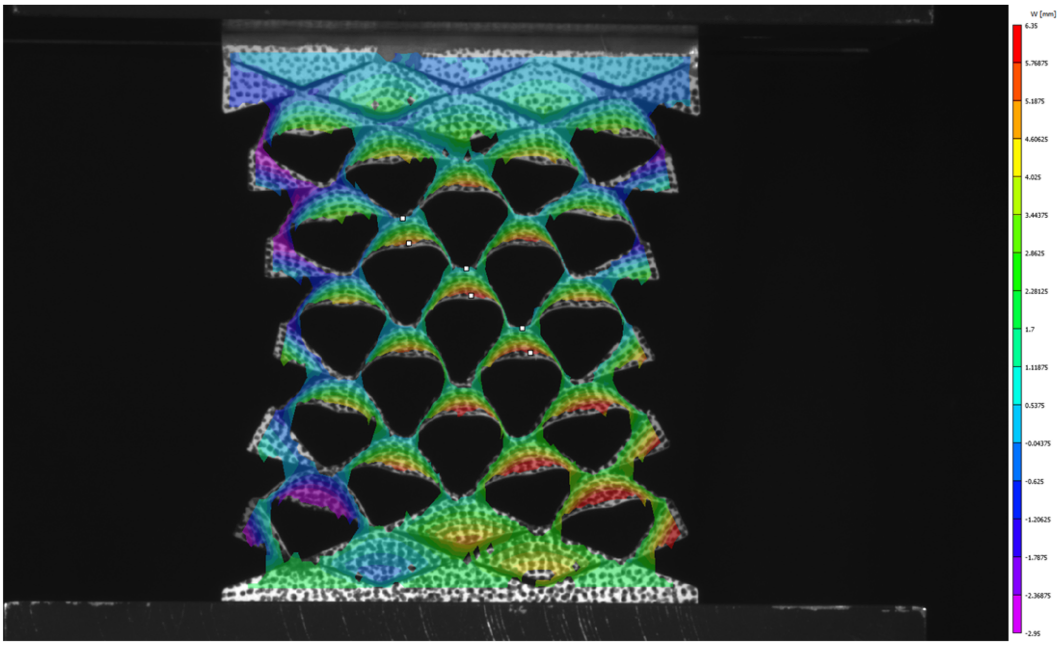

Figure 2.6: Deployed kirigami device showing the non-uniformity near the upper and lower boundaries [23]

The degree of out-of-plane deformation of the kirigami depends on the geometry of the cuts and the degree of in-plane extension of the device. This is quantified by Amin in Figure 2.7 [23], using Digital Image Correlation measurements. The displacement was normalised by the diagonal length of the triangular cut shape.

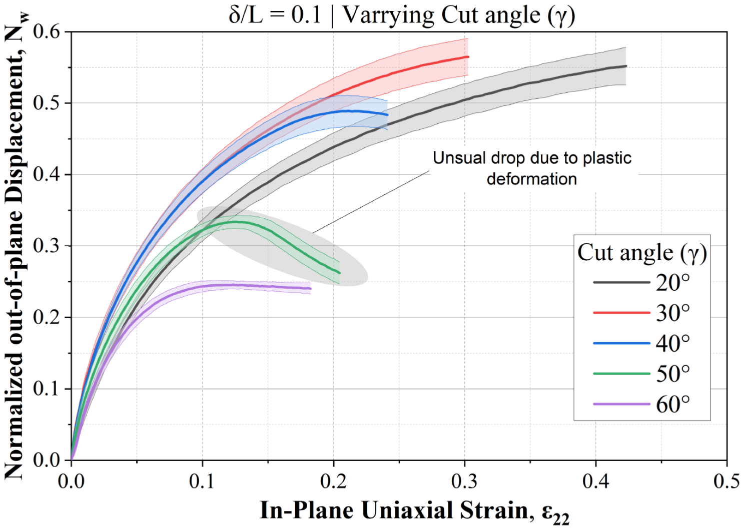

Figure 2.7: Non-dimensional Out-of-plane displacement of kirigami elements under relative in-plane extension for various cut angles of a triangular kirigami device [23]

The effect of the cut angle γ appears to determine the maximum deployment of the kirigami. This deployment height is maximised at lower angles of around 20 to 30 degrees. Beyond this, the maximum deployment drops off due to plastic deformation.

This deployment has also been modelled for flow control purposes using FEM, as shown in Figure 2.8 [22]. The only data that was available from this study was the deployment measured against in-plane loads. The figure shows how out-of-plane deployment increases with element size. It also highlights the effect that different cut shapes have on the stiffness of the deployment, with triangular being the stiffest.

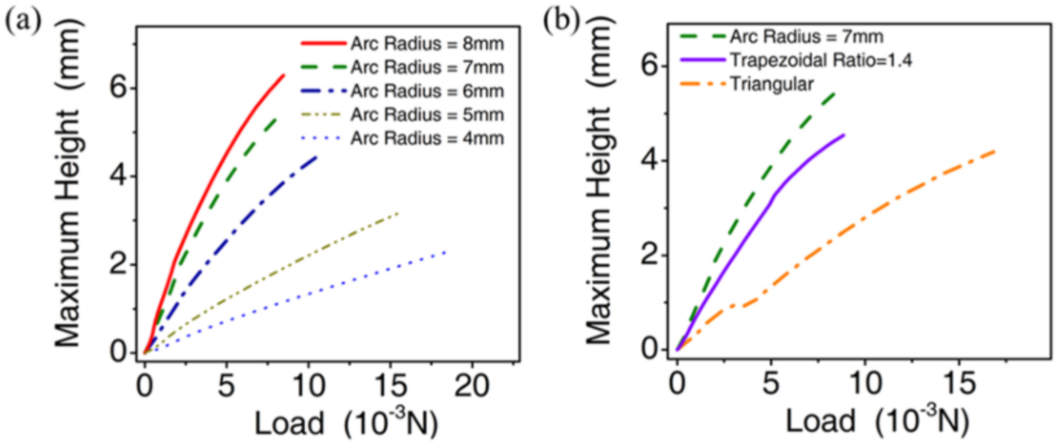

Figure 2.8: Non-dimensional Out-of-plane displacement of kirigami elements under relative in-plane force a) for various cut angles of a circular kirigami device, b) for different cut shapes[22]

2.3. Boundary Layers

In order to exercise control on flow separation, a fundamental understanding of the underlying physics is a minimum requirement. This section will give a structured overview of the physics that drive separation, and a description of different phenomena surrounding separation. The most important concept in the context of separation is the boundary layer.

In essence, separation is an effect characterised as the flow near a surface ceasing to follow that surface, and succeeded by a breaking away from it [28] [29]. Although reverse flow effects due to adverse pressure gradients can also occur away from a surface (such as wake bursting [30]), separation is typically associated with near-surface flows. Separation on the surface cannot only occur under an adverse pressure gradient, but also requires viscous surface flow interactions. This warrants a discussion on the concept of boundary layers

2.3.1. Fundamental concept of a boundary layer

The boundary layer is characterised as a layer of viscous flow near a surface. Its properties were described for the first time in 1904 [31]. To relate the influence of the viscosity to the total flow, the Reynolds number is defined as shown in Equation 2.1. It is composed of a reference velocity U, a reference length L, and the density ρ and dynamic viscosity μ of the fluid, which can be combined into one kinematic viscosity ν.

$$Re \equiv \frac{\text{inertial forces}}{\text{viscous forces}} = \frac{\rho U L}{\mu} = \frac{UL}{\nu} \tag{2.1}$$

The viscous flow is bounded at the wall with a zero slip and a tangential flow condition. This results in a variable velocity gradient between the freestream and the surface. At large Reynolds numbers, this gradient vanishes after just a small distance away from the wall. This thin viscous layer is what is defined as the boundary layer. Examples of typical boundary layer profiles are shown in Figure 2.9.

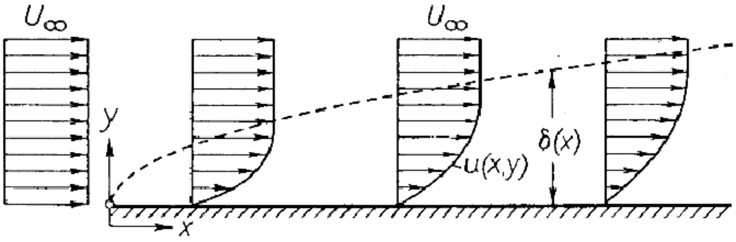

Figure 2.9: (Laminar) boundary layer profiles of a flow over a flat plate [32]

The existence of the boundary layer due to viscosity also results in shear stress due to friction on the surface. An elementary law of fluid friction stress exists in the form of Equation 2.2 [32].

$$\tau = \mu \frac{du}{dy} \tag{2.2}$$

The wall shear stress is obtained by taking du/dy at the wall (y=0). The equation demonstrates a proportional relation between the shear stress and the boundary layer velocity gradient.

2.3.2. Mathematical description of a boundary layer

A mathematical description can be found by analysing the continuity equation (conservation of mass), momentum equation (conservation of momentum) and energy equation (conservation of energy). With the assumption that the flow is incompressible (valid at low Mach numbers), the energy equation can be decoupled from the velocity field. Furthermore, body forces are neglected. For boundary layer analysis, the focus lies on the two equations shown in Equation 2.3 and Equation 2.4 [33].

$$\nabla \cdot \mathbf{U} = 0 \tag{2.3}$$

$$\rho \frac{D\mathbf{U}}{Dt} = -\nabla p + \mu \nabla^2 \mathbf{U} \tag{2.4}$$

These equations hold true for general incompressible flows. To investigate how boundary layer properties relate to separation, one can make simplifications to the equations by applying further assumptions. The equations can be non-dimensionalised and simplified for 2D flows according the convention in White [33], while ignoring temperature differences of the wall. This scaling is based on the fact that the vertical terms (v and y) scale with the Reynolds number where other terms scale with unity [33]. This gives the new form of the equations, shown in Equation 2.5 and Equation 2.6 [33]. The non-dimensionalisations are as follows: $x^* = \frac{x}{L}$, $y^* = \frac{y}{L}\sqrt{Re}$, $t = \frac{tU}{L}$, $u^* = \frac{u}{V}$, $v^* = \frac{v}{U}\sqrt{Re}$ and $p^* = \frac{p-p0}{pU^2}$.

$$\frac{\partial u^*}{\partial x^*} + \frac{\partial v^*}{\partial y^*} = 0 \tag{2.5}$$

$$\frac{\partial u^*}{\partial t^*} + u^* \frac{\partial u^*}{\partial x^*} + v^* \frac{\partial u^*}{\partial y^*} = -\frac{\partial p^*}{\partial x^*} + \frac{1}{Re}\frac{\partial^2 u^*}{\partial x^{*2}} + \frac{\partial^2 u^*}{\partial y^{*2}} \tag{2.6}$$

This non-dimensionalisation reveals the dependency of the momentum viscous flows on the Reynolds number. It also shows that the continuity equation is entirely scalable using reference values. As mentioned before, boundary layers are a direct result of very high Reynolds numbers. Using the assumption $Re \to \infty$, and assuming a steady flow, several more terms vanish, and the momentum equations reduce to Equation 2.7 [33].

$$u^* \frac{\partial u^*}{\partial x^*} + v^* \frac{\partial u^*}{\partial y^*} = -\frac{\partial p^*}{\partial x^*} + \frac{\partial^2 u^*}{\partial y^{*2}} \tag{2.7}$$

These equations are more commonly used to model laminar boundary layers than turbulent ones due to the absence of unsteady terms. Furthermore, an absence of the pressure gradient in y means that the pressure gradient in x becomes equivalent to the external pressure gradient ouside the boundary layer [33]. For turbulent boundary layers, the Reynolds Averaged Navier Stokes (RANS) equations should be applied. These equations are essentially a time average of the navier stokes equations, obtained by splitting the velocity into a time averaged, and a fluctuating component, i.e. $U_i = \overline{U_i} + U_i'$. Taking the time average of the navier stokes equations for similar assumptions and boundary conditions as the aforementioned equations then yields the RANS equations for boundary layers, shown in Equation 2.8, and Equation 2.9 [33].

$$\frac{\partial \overline{u}}{\partial x} + \frac{\partial \overline{v}}{\partial y} = 0 \tag{2.8}$$

$$\overline{u}\frac{\partial \overline{u}}{\partial x} + \overline{v}\frac{\partial \overline{u}}{\partial y} = \frac{1}{\rho}\frac{\partial \overline{p}}{\partial x} + \nu\frac{\partial^2 \overline{u}}{\partial y^2} - \frac{\partial \overline{u'v'}}{\partial y} \tag{2.9}$$

Equation 2.9 shows an almost identical relation as for Equation 2.7, except for an additional turbulent stress term, accounting for an extra source of momentum. This term is based on any type of velocity fluctuation (including turbulent mixing), which means that, in a (time-averaged) turbulent boundary layer, more momentum is mixed in the flow where fluctuations are higher, as compared to laminar boundary layers. This means the shear term τ consists of a viscous stress and a Reynolds stress.

2.3.3. Boundary layer thickness and parameters

The influence of viscosity vanishes further from the surface. A boundary layer therefore has a certain 'thickness' to it. Multiple definitions for this thickness exist, as the boundary layer thickness is not straightforwarldy defined due to the continuous nature of the velocity profile.

The most intuitive definition of thickness is the 99% velocity condition δ_{99}. This is defined as the y-coordinate where the velocity profile reaches 99% of the external velocity i.e. $.99U_e$ [32]. This parameter has no specific physical meaning, but attempts to make a distiction between the region of dominating viscous influence from the region with negligible viscous influence. When δ is used as the boundary layer thickness in this thesis, it refers to the 99% velocity condition δ_{99} unless otherwise specified.

A more rigorous method for defining the thickness is the displacement thickness δ^*. This thickness is based on the amount of fluid that is displaced away from the wall. More specifically, it is defined as show in Equation 2.10 for a given x-coordinate [32].

$$U_e\delta^* = \int_0^\infty (U_e - u)dy \tag{2.10}$$

This equation equates the velocity deficit in the boundary layer as opposed to the external flow with an equivalent mass flow deficit if the boundary layer were a step function with the step location at $y = \delta^*$ and a step size from 0 to U_e. More specifically, it tells us how far the streamlines of the outer flow are displaced by the boundary layer [32]. This definition is therefore practical for determining equivalent inviscid contours for flows around bodies or profiles, where inviscid calculation can be applied e.g. in airfoil panel codes.

An alternative to the displacement thickness is the momentum thickness θ. This has a very similar definition to the displacement thickness, but instead uses a momentum deficit, rather than a mass deficit. This is defined as Equation 2.11

$$U_e^2\theta = \int_0^\infty u(U_e - u)dy \tag{2.11}$$

This definition is typically used to determine momentum effects of the near-wall viscosity. Specifically, it can be related to overall friction and drag in laminar boundary layers through integral methods [33]. The displacement and momentum thickness can be applied to both laminar and turbulent boundary layers, although for the latter, time averaged velocities should be applied [33].

Both the momentum and the displacement thickness can be related in a single parameter, the shape factor H. This factor is defined by their ratio, that is, $H = \frac{\delta^*}{\theta}$, and typically varies from 1.3 to 2.5 for turbulent flows [33]. This parameter is an indication of the shape of the velocity profile, and can also be used as a measure for how prone a boundary layer is to separation.

2.3.4. Classical turbulent boundary layer scaling & fundamentals

Due to the unsteady nature of turbulence, scaling of the boundary layer typically only involves the mean flow. To achieve this scalability, several similarity laws and scales have been proposed throughout history.

As shown earlier, the shape of the boundary layer is a direct function the pressure gradient. Clauser [34] proposed the use of what is now known as the Clauser pressure gradient parameter, defined as in Equation 2.12

$$\beta = \frac{\delta^*}{\tau_w}\frac{dp}{dx} \tag{2.12}$$

This parameter is typically used for pressure gradient characterisation in turbulent boundary layers (such as in Herring [35]), although alternatives have been proposed on occasion [36].

The turbulent boundary layer itself is composed of three parts [33]. These are the *Viscous Sublayer*, the *Outer Layer* and the *Overlap Layer*. A diagram of this structure can be found in Figure 2.10[3].

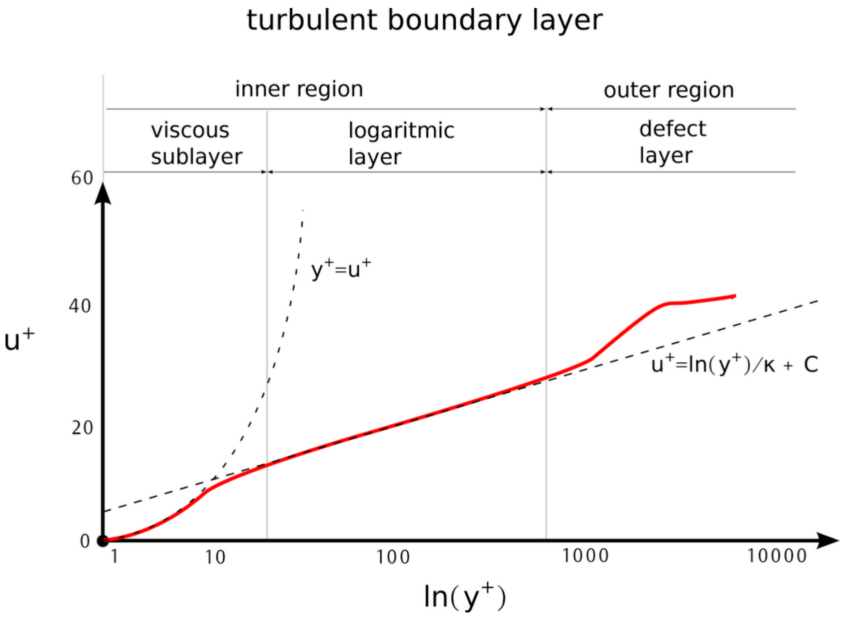

Figure 2.10: The conceptual structure of a turbulent boundary layer[3]

In the Viscous Sublayer, viscous shear is the dominant type of shear. In the Outer Layer, turbulent shear dominates (Reynolds stresses). The intermediate Overlap Layer connects the sublayer and the outer layer. For the inner layer, the following variables are postulated to be of significance (Equation 2.13 [33]. Note that none of these are freestream parameters.

$$\overline{u} = f(\tau_w, \rho, \mu, y) \tag{2.13}$$

For the outer layer, one can use the velocity defect to postulate relevant variables, as shown in Equation 2.14 [33]

$$U_e - \overline{u} = f(\tau_w, \rho, y, \delta, \frac{dp_e}{dx}) \tag{2.14}$$

For the overlap layer, a compatibility equation is specified between the inner and outer layer to smoothly merge the two, such that $\overline{u}_{inner} = \overline{u}_{outer}$ [33].

For these parameters, the velocity is nondimensionalised by the ”friction velocity”, defined as in Equation 2.15

$$u_\tau = \sqrt{\frac{\tau_w}{\rho}} \tag{2.15}$$

---

[3] https://www.cfdsupport.com/openfoam-training-by-cfd-support/node342.html

For the viscous sublayer, Von Kármán [37] used the parameters in Equation 2.13 to compose the so-called *law of the wall*, shown in Equation 2.16.

$$\frac{\overline{u}}{u_\tau} = f\left(\frac{yu_\tau}{\nu}\right) \tag{2.16}$$

Similarly, for the outer layer, a *velocity defect law* is proposed [33], shown in Equation 2.17. For these function, sometimes the Rotta-Clauser length scale Δ is used instead of δ [36].

$$\frac{U_e - \overline{u}}{u_\tau} = g\left(\frac{y}{\delta}, \beta\right) \tag{2.17}$$

For the overlap layer, the two velocity laws are set equal, which results in a logarithmic relation for both profiles [33], Equation 2.18 for the viscous sublayer and Equation 2.19 for the outer layer.

$$\frac{\overline{u}}{u_\tau} = \frac{1}{\kappa} ln\left(\frac{yu_\tau}{\nu}\right) + B \tag{2.18}$$

$$\frac{U_e - \overline{u}}{u_\tau} = -\frac{1}{\kappa} ln\left(\frac{y}{\delta}\right) + A \tag{2.19}$$

The parameter A typically varies with the pressure gradient β, and should stay constant under constant β, according to Clauser [34]. However, according to Coles and Hirst [38], κ and B are constant at $\kappa \approx 0.41$ and $B \approx 5.0$.

Figure 2.11 shows the validity of the overlap law, and the variation of outer flow. For convenience, $\frac{\overline{u}}{u_\tau}$ and $\frac{yu_\tau}{\nu}$ are redefined to u^+ and y^+, respectively. These represent the wall coordinates. Alongside the overlap law, the figure also shows typical shapes of the inner layer and outer layer. The inner layer is typically modelled with power laws.

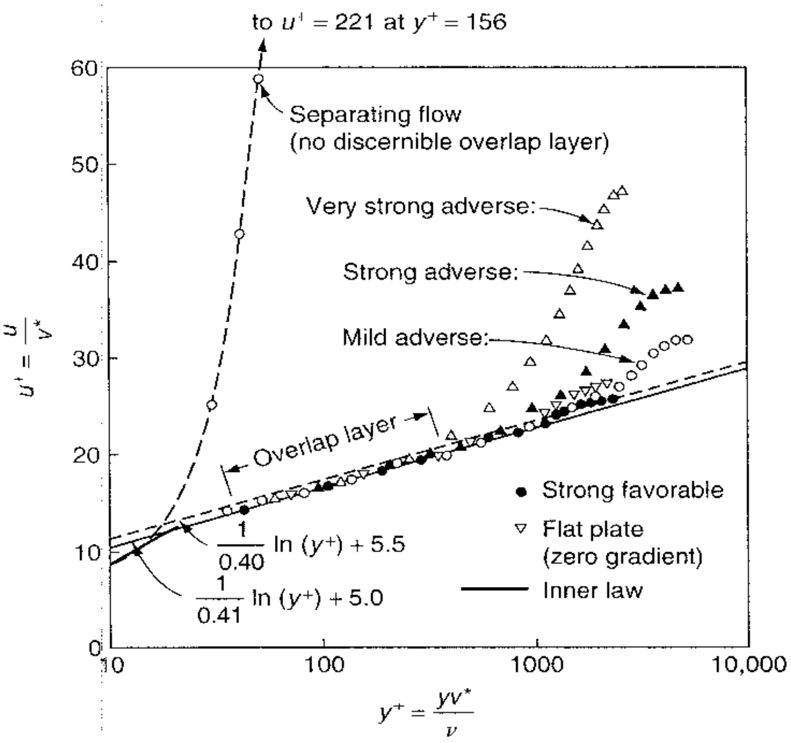

Figure 2.11: Velocity profiles of turbulent boundary layers in log wall coordinates [33]

The figure also shows that the overlap layer appears to vanish for flow separation, which is of particular interest to this study. In fact, Perry & Schofield [39] suggests that in adverse pressure gradients boundary layers close to separation, the log law of the overlap layer is closer to a "half-power distribution".

2.4. Boundary layer separation

The concept of the boundary layer has established the phenomenon of deceleration of fluid near the wall. Upon excessive deceleration, the flow in the boundary layer might be reversed. Flow reversal leads the surface flow into a condition where the streamlines no longer follow the surface and steer away from it, along with the near-wall flow typically being replaced by a region of recirculation. This is what is generally recognised as separation. The actual mechanism of boundary layer separation happens under specific conditions, and depends on several variables and circumstances, which are all described in this section, along with some of the phenomena in turbulent separation.

2.4.1. Onset of separation and the separation point

As mentioned before, flow separation is essentially the result of of flow reversal in a boundary layer. The pressure gradient plays a key role in this, which can be shown by analysing Equation 2.7. By imposing the boundary conditions of $\mathbf{V} = 0$ at the wall, the equation in question is reduced to Equation 2.20

$$\frac{\partial p^*}{\partial x^*} = \frac{\partial^2 u^*}{\partial y^{*2}} \tag{2.20}$$

In fact, Equation 2.20 shows that the curvature of the boundary layer velocity profile at the wall is directly determined by the pressure gradient in the laminar boundary layer. Flow reversal in a boundary layer is only achieved when both the velocity and the shear become zero. Mathematically speaking, for a boundary layer, this can only happen if the velocity profile curvature at the wall is positive in sign. This shows that separation in a laminar boundary layer occurs specifically in a positive, or adverse pressure gradient (APG). The point where this flow reversal occurs can be defined as the separation point, and is equivalent to the wall shear stress (as defined in Equation 2.2) reaching zero, *i.e.* $\tau_w = 0$.
Due to the similarity between Equation 2.7 and Equation 2.9, and the fact that $\frac{\partial \overline{uv}}{\partial y}$ is zero at the wall [29], the same conclusion holds for a time-averaged turbulent boundary layer. However, due to the unsteady nature of turbulent separation, the shear and the streamwise velocity fluctuate significantly over time. This means that the instaneous separation point is not contained to a singular streamwise location. In fact, flow reversal can occur for a fraction of time in streamwise locations in the turbulent boundary layer that would not typically be considered separated [40]. This calls for an alternative measure of turbulent boundary layer separation.

For this, one can use the fraction of time in which the wall tangential flow direction is negative. First introduced in the work of Simpson as γ_{pu} [40] [41], this quantity was later named the *backflow coefficient* χ. This report will mostly adhere to the former symbolic convention γ_{pu} This fraction indicates what type of separation state is present at that location. Simpson [40] distinguishes four different levels of turbulent separation onset. Incipient Detachment (ID) occurs where $\chi = 0.01$, Intermittent Transitory Detachment (ITD) happens for $\chi = 0.20$, and then finally, Transitory Detachment (TD) occurs when $\chi = 0.50$. Additionally, "Detachment" (D) is defined such that the time averaged wall shear stress is zero *i.e.* $\overline{\tau}_w = 0$. According to Simpson, it can be concluded that this coincides with the point where Transitory Detachment is found [40].

2.4.2. Anatomy of turbulent separation

Extensive research has been done on the characteristics of turbulent separation regions, particularly by Simpson et al. [40][41]. The experiments involved in these studies give an idea of the characteristics of turbulent separation.
Velocity measurements clearly show the formation of a recirculation region in the mean flow. This is shown in Figure 2.12, which also shows the locations of the previously mentioned separation regions (based on the backflow coefficient), including the coincidence of mean flow reversal with Transitory Detachment. Sandborn and Liu found correlations for the location of what they define as intermittent separation and fully developed separation [42].
The mean velocity profiles measured in these experiments corroborate the vanishing of the mean velocity curvature at the separation point. These quintessential turbulent separation profiles are shown in Figure 2.13a. The law of the wall and corresponding skin friction estimation are still applicable for the profiles where no yet backflow exists (*i.e.* $\chi = 0$) [41].

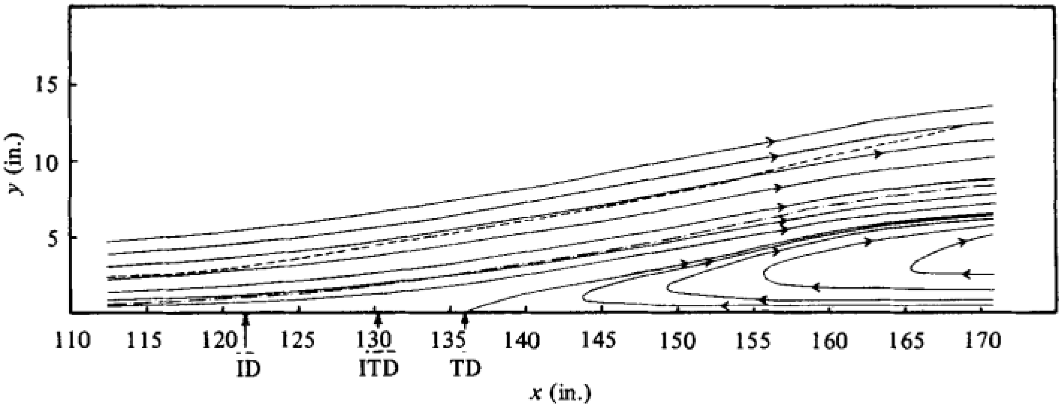

Figure 2.12: Mean streamline flow pattern for turbulent separation in the experiment of Simpson [41], including boundary layer edge and displacement thickness (dashed and dash-dotted line respectively)

Similar profile measurements exist for the Reynolds stress in the separating boundary layer, shown in Figure 2.14. These show that the Reynolds stresses are roughly maximum in the middle of the boundary layer, and reduce to zero towards the wall. This is consistent with the aforementioned inner-outer layer distiction established in turbulent boundary layer scaling. This pattern holds up for separation, although the peak intensity of the Reynolds stresses decrease significantly as separation develops.

Although Figure 2.12 implies that flow is carried all the way back from far downstream, Simpson suggests that these ”do not respresent the pathlines for the elements of fluids”, and that the backflow is ’supplied’ more locally [41]. To complete the discussion, and gain a more detailed account of the backflow, similar profiles are plotted for the backflow in Figure 2.13b. These figure, shows that the peak backflow occurs relatively close to the wall, with backflow initiating before mean flow detachment occurs

For these distributions, similarity can also be applied [41] according to an empirical formula [43], which relates $\frac{\chi-\chi_0}{1-\chi_0}$ to $\frac{y}{M}$, where χ_0 is a reference value, and M is the vertical distance from the wall to the location of maximum root mean square streamwise velocity fluctuations. Similiarity also exists for the wall-normal flow counterpart of the backflow coefficient (γ_{pv}) [41].

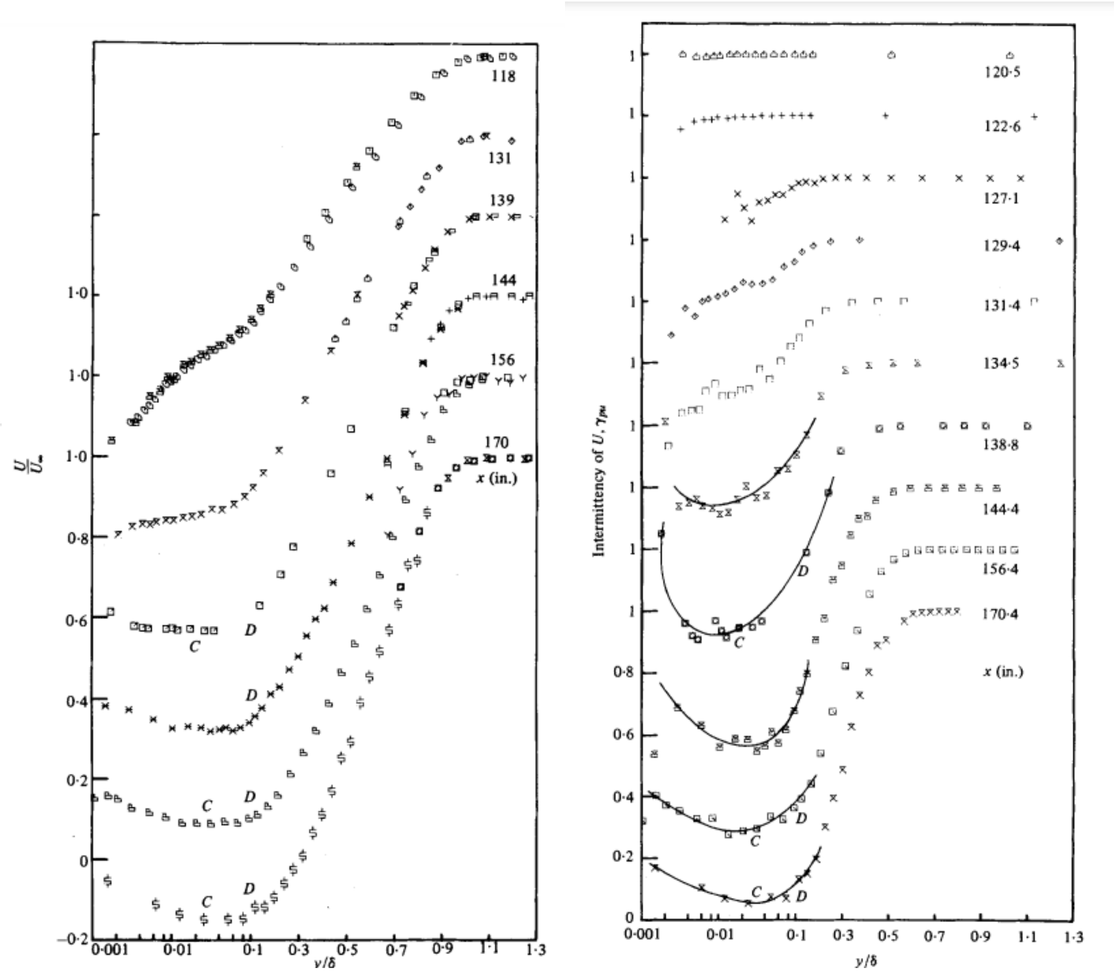

(a) Velocity profile

(b) Backflow coefficient

Figure 2.13: Mean boundary layer velocity profiles for turbulent separation in the experiment of Simpson [41], with logarithmic height scale and displaced velocity scales for each measurement point

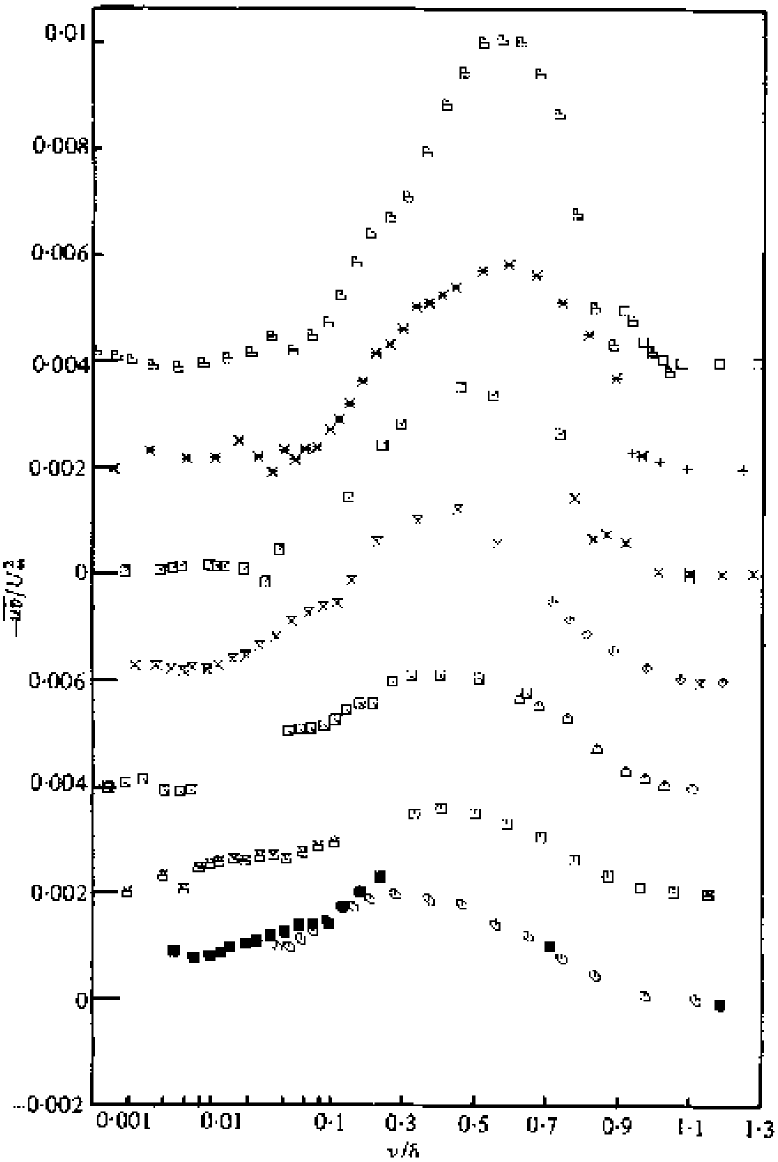

Figure 2.14: Mean boundary layer Reynolds shear stress profiles for turbulent separation in the experiment of Simpson [41], with logarithmic height scale and displaced velocity scales for each measurement point

2.5. Vortex generators

The next few sections delve into the strategies and mechanisms employed to manage and mitigate separation phenomena.

It was established in the previous sections that the decrease in near-wall momentum that is responsible for separation is driven by a combination of a pressure gradient and viscosity effects near the wall. The combination of the two ultimately enables flow reversal. Notwithstanding straightforward pressure gradient design [29], the natural approach for separation control is therefore to add more momentum near the wall, either through active addition or passive mixing. Active techniques constitute boundary layer suction/blowing or wall heating/cooling [29]. These active techniques often require extra energy input and/or complex devices integrated with the aerodynamic surface. Passive devices, on the other hand, require no extra energy input. The most prevalent example of this is through swirling flow, generated by devices such as vortex generators. These aim to create more mixing between the inner boundary layer and the high momentum outer flow.

Vortex generators (VGs) are perhaps the most archetypical form of separation control. First tested by Taylor in 1947 [7], VGs have been the topic of decades of research. Various different types of VG will be highlighted, as well as the underlying physics.

2.5.1. Parameterisation and scaling of vortex generators

The geometric design of a vortex generator does not only involve an reference shape. Each shape can also be subjected to scaling based on specific parameters involving both geometry and spacing of the vortex generators. An overview will be given on the typical parameters used and how scaling is applied to these parameters.

Lin [8] uses the following comprehensive set of parameters to fully describe a varied set of vortex generators: device height, device length, device angle, spanwise device spacing and streamwise distance between VG trailing edge and baseline separation. Respectively, the symbols for these are h, e, β, Δz, and ΔX_{VG}. For counter-rotating vortex generators, an additional parameter is required for the spacing inbetween a pair of vortex generators, L. Of these, the dimensional parameters are typically non-dimensionalised with respect to h. These parameters have been subjected to sensitivity studies by Godard & Stanislas [44], although no general theory exists for the design of these vortex generators, and the optimal design depends on the context.

Another important parameter in this context is the boundary layer thickness δ. The scaling of the generator must always be in proportion to the boundary layer, thus $\frac{h}{\delta}$ is typically used as a nondimensionalisation. The order of magnitude of this scale is twofold. Clasically, the most effective scale is when the height of the vortex generator matches the boundary layer i.e $\frac{h}{\delta} \approx 1$ [45]. However, the recent work of Lin [8] [46] has shown that similar effectiveness can be achieved with sub-boundary layer-scale vortex generators, i.e. $\frac{h}{\delta} \sim 0.1 - 0.3$, whose low-profile nature have the added benefit of lower parasitic drag. The tips of VGs of this scale impinge on the log layer of the boundary layer instead of the outer layer [8]. Figure 2.15 shows a conceptual sketch that compares how the boundary layer profiles are modified under the influence of streamwise vortices from both BL-scale and sub-scale vortex generators.

The figure shows a similar pattern to that of Figure 2.19 in the sense that momentum is moved from the upper side to the lower side of the boundary layer. However, the sub-δ scale VGs remove significantly less momentum away from the wall to achieve an increased shear near the wall, which demonstrates their reduced effect on parasitic drag.

2.5.2. Vortex generator types

VGs come in a variety of shapes. Their aim is to generate vorticity through pressure gradients or deformation of vortex lines. This vorticity can be either of streamwise or spanwise nature. The aim of this vorticity is to create a macro-mixing effect in the flow such that ”the near-wall momentum is increased through the momentum tranfer from the outer (free-stream) flow” [8]. A one-by-one analysis of several VG type of interest (as they appear in literature) will point out which type is responsible for what type of vorticity.

Vane-type in co-rotating configuration

The most straightforward form of generating vortices is with vane type vortex generators. These were originally studied in the late 40s/early 50s, in the form of ”small airfoils of rectangular planform mounted normal to the surface”, and are typically mounted in an array [7] [48]. Recent research points out that

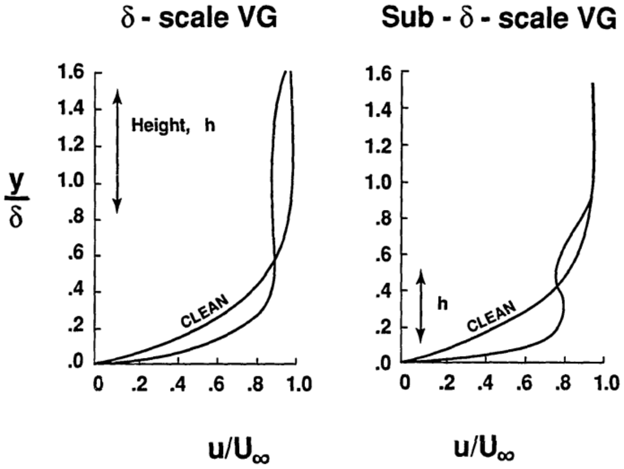

Figure 2.15: Conceptual modified boundary layer velocity profiles due to conventional vortex generators vs sub-BL vortex generators [47]

vane-type VGs are the most effective type to delay flow separation (in incompressible scenarios). [8] [44]. Whether the vane is mounted at a positive or negative angle determines the rotation direction of the vortex. This can be exploited to either have an array of vortices rotating in the same direction (co-rotating) or vortices alternating direction with each vane (counter-rotating). Diagram of this distinction can be found in Figure 2.16, Figure 2.17 and Figure 2.18. This specific section focuses on the co-rotating arrangement.

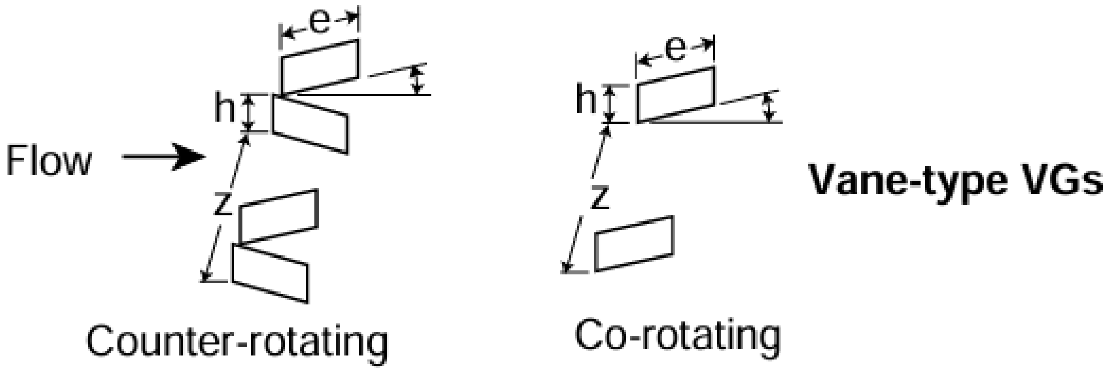

Figure 2.16: Counter-rotating vs co-rotating vane-type VGs [8]

Vane type vortex generators create strong streamwise vortices [8]. This allows for continuous mixing downstream of the vortex generator in the mean flow. The vortex is generated through the pressure difference on the finite surface of the vane, comparable to a wing tip vortex. To this end, different shapes can be used, although the most commonly encountered in literature are the rectangular (see Lin [46]) and the triangular (delta) vanes (see Ashill [49]). The co-rotating vortices have proven to be highly effective at delaying separation [8] and cover a larger downstream range than the counter-rotating versions, owing to the fact that they stay attached to the surface for longer [46] [44].
Momentum transfer between each vortex pair happens both towards the wall, and away from the wall [44]. This is highlighted in Figure 2.17. The drawback of these devices is that they are highly sensitive

to spacing, as the opposing momentum transfers between each vortex pair could cancel eachother out with insufficient spacing, reducing effectiveness [44]. Another effect that can happen is that the collection of vortices have spanwise movement due to induction [44].

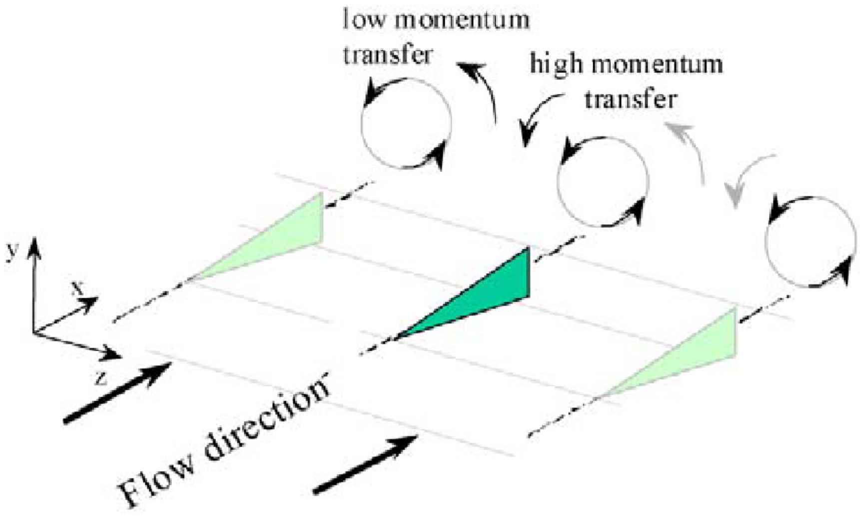

Figure 2.17: Momentum transfer for co-rotating vortex generators [44]

Counter-rotating vane-type vortices

Counter-rotating vortex generators, as described earlier, focus on creating alternating vortices with opposite direction, as shown in Figure 2.16. These were developed in tandem with the co-rotating vortex generators. The principle is mostly the same, except that now, inward and outward momentum transfer alternates between vortex pairs, as shown in Figure 2.18. As a result, the effect of both vortices magnify each type of momentum transfer, and some have found that counter-rotating vortex generators are more effective [44] [46]. However, it was also found that this depends on flow conditions and vortex placement [46].

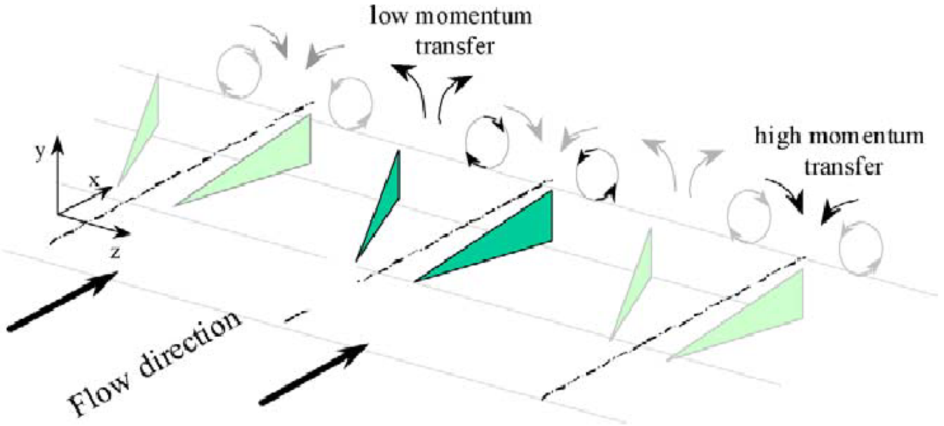

Figure 2.18: Momentum transfer for counter-rotating vortex generators [44]

The drawback of counter-rotating vortex generators is that the streamwise lifespan of the vortex is much more limited due to the mutual induction lifting the vortices away from the wall, as this negates the near-wall mixing [44] [50]. This effect is once again sensitive to spacing of the generators. Rather than

equidistant spacing, vortices can also be paired in both ”common-up” and ”common-down” arrangement [50] and then spaced by pairs (z-parameter in Figure 2.16).
Velocity profiles measured in literature give a consistent image of the effect of vortex generators on the velocity profile. Measurements show that momentum near the wall is increased significantly, resulting in a much larger shear at the wall (see [46] [51]), and therefore a stronger resistance to separation. An experimental example is shown in Figure 2.19. A similar pattern is also shown in Figure 2.15.

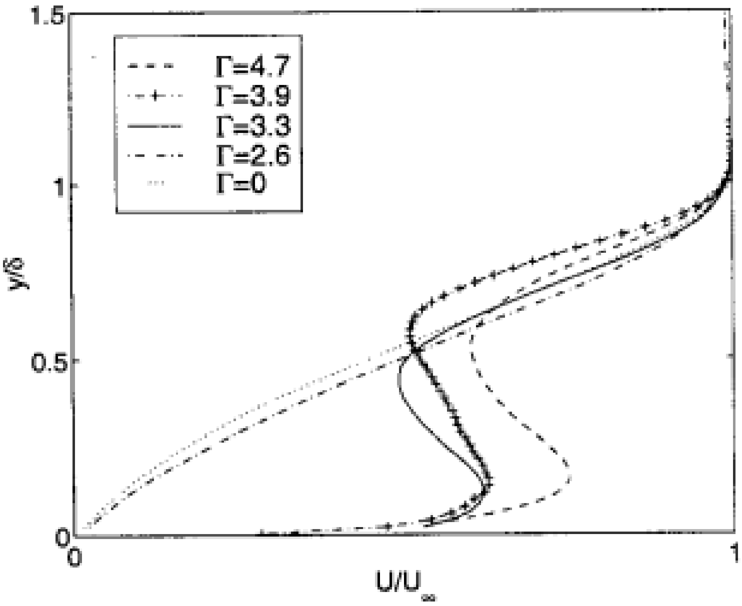

Figure 2.19: Experimental modified boundary layer velocity profiles due to counter-rotating vortices of different vortex strengths [51]

The figure clearly shows that significant momentum is added towards the wall and removed from near the boundary layer edge. As a result, the shear $\frac{\partial u}{\partial y}$ is also significantly increased, which helps to prevent separation.

Wedge/microramp vortex generators

Wedge style vortex generators are triangular solids raised away from the surface at a certain angle. They can either face towards the flow (forwards wedge), or away from the flow (backwards wedge), as shown in Figure 2.20. Their presence in literature is more significant in the category of shock-boundary layer interaction and shock induced separation (see [52] [53]), although they also show the capability for separation control in sub-sonic conditions [49].
The fluid dynamics of a forward wedge-shape are fairly well understood. A diagram is shown in Figure 2.21 based on the experimental work of Babinsky [53]. Apart from a primary vortex pair, secondary vortices are also generated, along with a horseshoe vortex. The applicability of this model in low-speed context is an assumption, as the literature surrounding this involves high-speed aerodynamics.
Furthermore, the downstream development of the primary vortex pair results in lift-up from the surface which creates characteristic hairpin vortices (cite 2 or 3 papers), which eventually break down into vortex rings and decay, as shown in Figure 2.22.

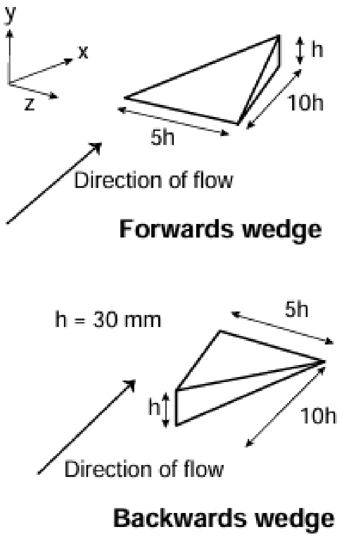

Figure 2.20: Wedge-style vortex generators [49]

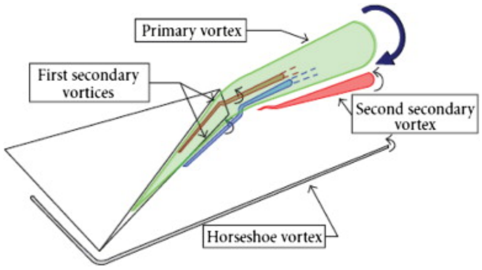

Figure 2.21: Vortices around a wedge-style vortex generator [53] [54]

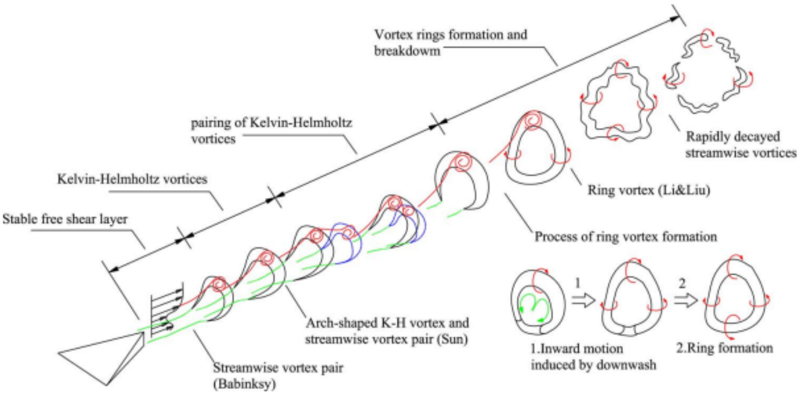

Figure 2.22: Hairpin vortex generation due to a wedge vortex generator [55]

Consequently, the vortex strength as measured by circulation decays much faster downstream than for vane-type vortex generators, as per the data of Ashill [49].

Other types

Other notable types of vortex generators found in literature are the trapezoidal tab and the hemispherical bump.

Similarly to the wedge VG, the trapezoidal tab is a shape protruded at an angle from the surface. However, the tab exists as a thin surface rather than a solid. The downstream result of this tab is a combination of hairpin vortices and streamwise counter-rotating vortices (common-up) [56]. Figure 2.23 gives both a sketch of the geometry of the trapezoidal tab and the vorticity generated by it.

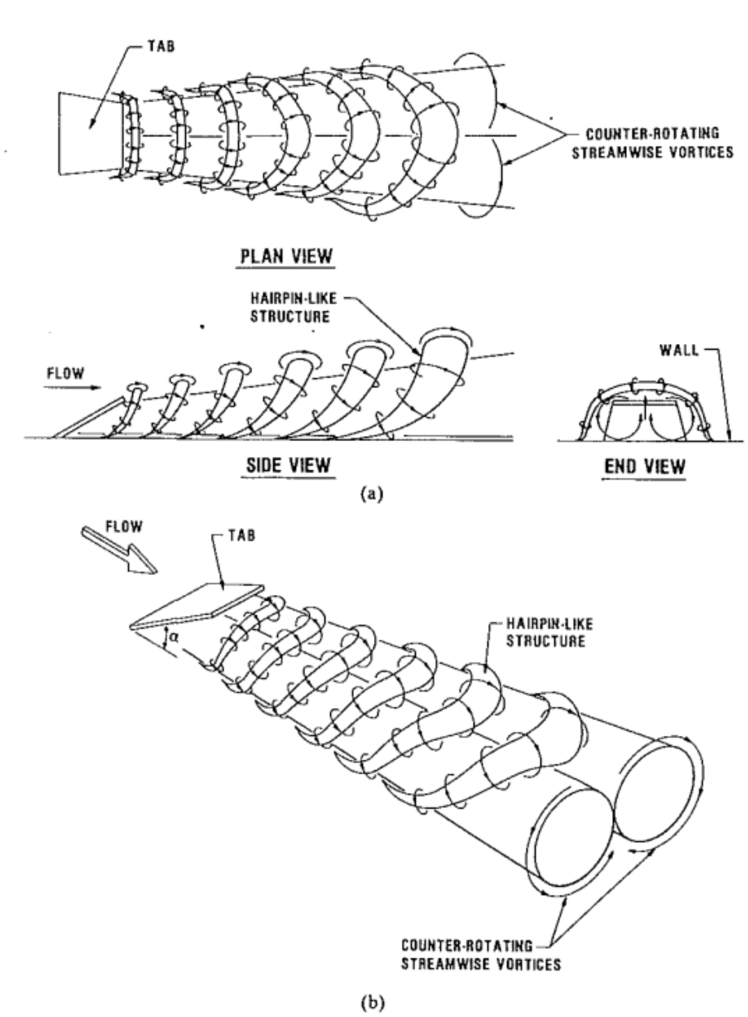

Figure 2.23: Vortex pattern generated by a trapezoidal tab vortex generator [56]

The hemispherical generator is simply a hemisphere on a surface. The pressure gradients over this body is still capable of generating downstream vorticity. This vorticity once again appears in the form of hairpin vortices, but also a 'standing vortex' that is akin to a horseshoe vortex [57]. If the hemispherical shape is extended into a teardrop shape, this standing vortex is eliminated. See Figure 2.24 for a sketch.

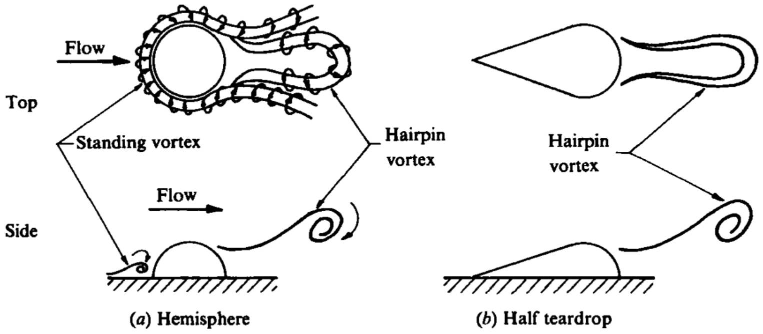

(*a*) Hemisphere

(*b*) Half teardrop

Figure 2.24: Vortex pattern generated by a hemispherical vortex generator [56]

Spanwise vortex generators (cylinders)

Rather than streamwise vortices, vorticity can also be generated in spanwise direction. An example of this is through the use of spanwise cylinders, which can exercise boundary layer separation control. The net effect of this shedding is the introduction of large-scale wake turbulence in the freestream [58]. These cylinders can have comparable, albeit decreased effect on the delay in separation and cause more drag [46].

2.5.3. Effect of repeated vortex generators

Vortex-generating geometry can be repeated for improved effectiveness. Presumably, a repetition of the vortex generator with the same sense of vorticity reinforces the vortex strength. One approach to this is by making a repeated, waving wall, as done by Kuethe [59]. The other approach is simply to repeat a vortex generator, referred to as a doublet. Doublet vortex generators are of particular interest as they most closely resemble the kirigami geometry that is used in this thesis project. These have been studied extensively by Lin [47] [46] [60], and shown to be effective when applied as sub-boundary layer scale VGs. The effect is slightly lower than that of vane-type vortex generators [8].

2.6. Shark skin

Separation control can also be in the form of geometry covering the entire surface. One example of this was mentioned earlier in subsection 2.5.3, being the concept of Kuethe vortex generators. Another, more influential example from nature, is shark skin. The skin of a fast-swimming shark has been known to reduce drag, partially through the prevention of flow separation over the fins. A brief discussion will follow on how this shark skin works as a separation control method.

The most iconic example of shark skin is that of the *Isurus Oxyrinchus* mako shark. The scales or denticles responsible for flow control are shaped like hands, or hammers, which can change their angle of attack up to 50 degrees [61], as shown in Figure 2.25. The lay-out of these scales resembles an array, which varies across the body, as shown in Figure 2.26.

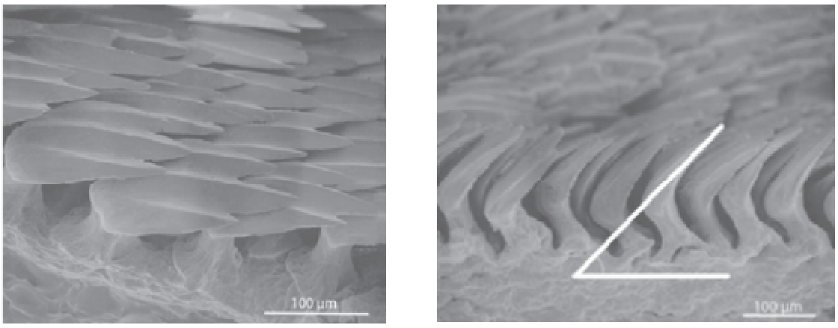

Figure 2.25: Side view of the shark skin scales of the *Isurus oxyrinchus* mako [61]

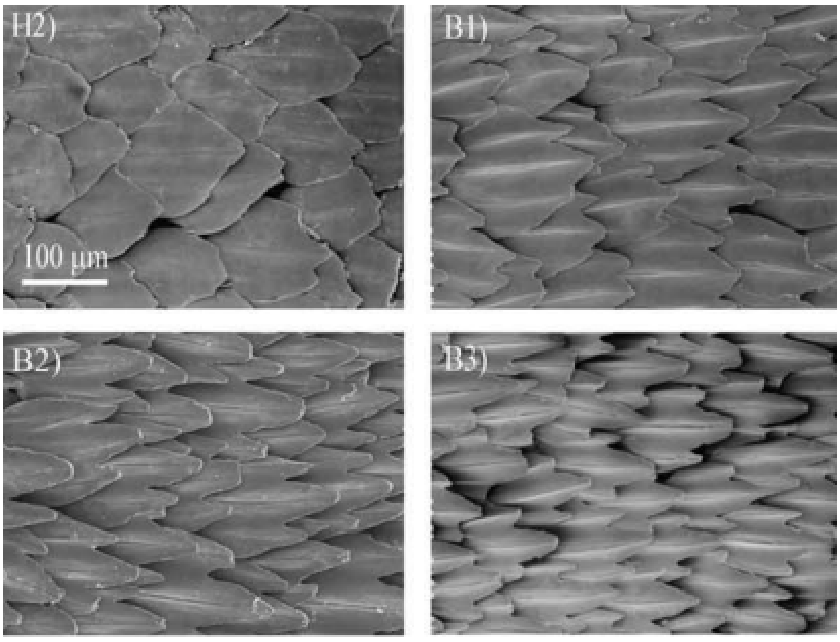

Figure 2.26: Top view of the shark skin scales of the *Isurus oxyrinchus* mako at several locations on its body [62]

Early research proposes that shark skins simply work as vortex generators, where at an angle of attack, each denticle produces a counter-rotating (common up) streamwise vortex pair [63], according to wind tunnel tests with air as a fluid. It should be noted that these conclusions were drawn from laminar boundary layer experiments. Another proposed mechanism is that flow reversal actuates the denticles, which disrupts the flow reversal [61].

The protruding, repeated geometry of shark skins bears mutual resemblance to the concept of tension-activated kirigami surfaces. Moreover, more recent work into laser-cut biomimetic fish skins have an even stronger likeness to kirigami surfaces [64]. These surfaces could serve as inspiration for the design of kirigami surfaces for this experiment, although they are activated by surface curvature rather than tension-activated. Examples can be found in Figure 2.27.

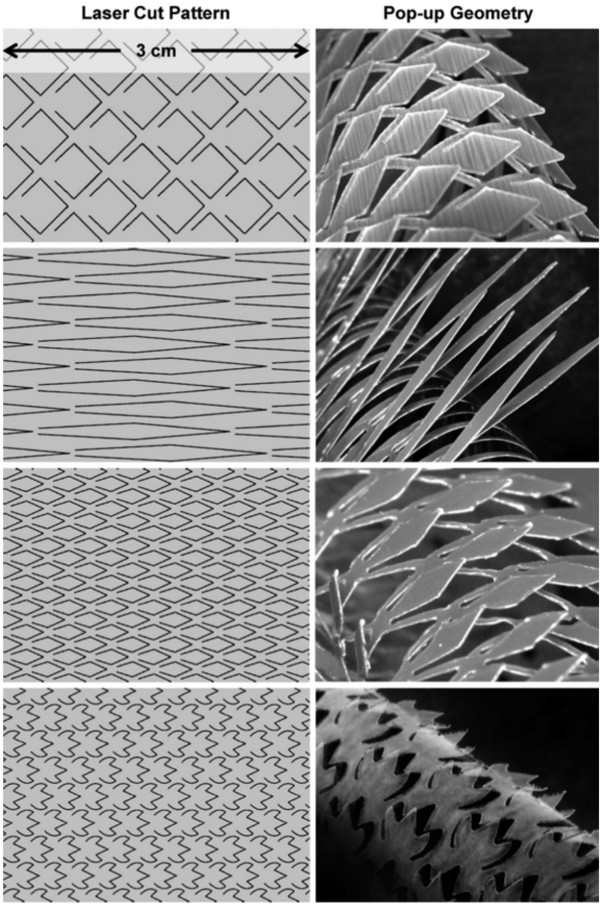

Figure 2.27: Examples of biomimetic fish skins used by Lauder et al. [64]

2.7. Roughness

Another example of whole-surface geometry affecting the flow is roughness. Roughness is characterised as a form of surface texture, specifically as ”geometrical irregularities with a high frequency”, and it is typically a result of some damage mechanism to the surface, or accretion of material on the surface [65]. Shark skin and zig-zag strips could also be classified as roughness. It is therefore reasonable to also consider the possibility of a kirigami metasurface to function as such.

One form of roughness-based separation control that is widely used involves either global or localised roughness on the surface, which enhances disturbances in a laminar boundary layer in an adverse pressure gradient, leading to earlier transition to turbulence [66] [67]. However, in turbulent boundary layers, the roughness has a more nuanced effect. The presence of roughness results in a modification to the ZPG boundary layer profile, in the form of a momentum deficit in an additional sublayer (the ’roughness sublayer’)[65]. The presence of surface roughness in turbulent separation, therefore, is adverse, resulting in larger separation regions [68], which can be attributed to this momentum deficit [69].
Similar to vortex generators, roughness is generally also characterised by a height with respect to the surface. Since this height is ambiguous in the case of an arbitrary roughness profile, the height is measured by an ”equivalent sand grain roughness” k_s, which is based on similarity between flows over an arbitrary roughness and a uniform sand grain roughness of height k_s [65] [70]. The turbulent separation experiment of Wu & Piomelli [69] was performed at a roughness height of $\frac{k_s}{\delta} = 0.07$. The actual scaling of roughness happens using the roughness reynolds number $k_s^+ = \frac{k_s u_\tau}{\nu}$. This parameter defines 3 regimes of roughness as it increases. First, hydraulically smooth, which is fully embedded in the viscous sublayer and has little effect on the boundary layer. Then, transitionally rough, which protrudes into the viscous sublayer and partially destroys it. Lastly, fully rough exceeds the scale of

the viscous sublayer and has the most disruptive impact, completely replacing this viscous sublayer by turbulence[65].

2.8. Other passive separation control methods

Reviews such as Gad-El-Hak[29] mention various other, less common passive separation control methods through turbulence amplification, using vortex shedding from rails or transverse cylinders, or helmholz resonators. Of more interest in the context of kirigami, however, is the work of Howard & Goodman [71] [72] [73]. This involves repeated transverse grooves in the aft section of a bluff body, resulting in significant drag reductions. The repetitive nature of these grooves have parallels to an array of kirigami metasurface elements. Along other more elementary mechanisms such a boundary layer transition and shedding of vorticity, one of the hypothesised flow mechanism is that the grooves function as a 'roller bearings', implying that recirculation in the grooves locally eliminates the zero-slip condition[72], which would reduce shear stresses at the wall.

2.9. Kirigami flow control

The concept of kirigami structures being applied to flow control is still in an early stage. In fact, only two examples in scientific literature exist where kirigami was directly applied as a separation control device. Considering the lack of data, both experiments therefore carry significant relevance for the current project.

2.9.1. Cylinder wake control

Kirigami flow control was applied on a cylinder by Wen et al. [22] in the context of vortex shedding. This is, as of yet, the only paper that has attempted such an application.
The aim of this research was to use adaptive kirigami devices to mitigate, reduce, or remove vortex shedding from a cylinder, which is a phenomenon that is driven by (laminar) separation. This involved an experiment carried out in an open-loop wind tunnel, employing PIV to measure the flow. The cylinder operates in the subcritical reynolds number regime for vortex shedding, so the boundary layer is presumably laminar. Figure 2.28 shows how the kirigami elements are applied to a cylinder, and highlights the deployability of these kirigami devices. The kirigami used are the triangular, circular and trapezoidal cuts that display out-of-plane deformation (These are shown in Figure 2.4).

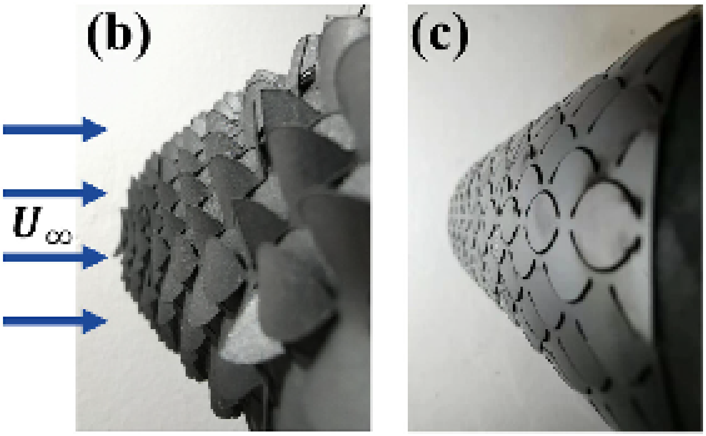

Figure 2.28: kirigami (circular, out-of-plane deformation) on a flow control experiment, deployed and undeployed state in the experiment of Wen et al. [22]

The research concluded that loads on the structure induced by vortex shedding can be mitigated in a subcritical regime (laminar boundary layer with periodic vortex shedding [22]). The particular mechanism for this that emerges from the presented data is by moving the shedding vortices further away from the cylinder, although no load measurements are presented to back this up. Figure 2.29 however, shows that the (asymmetric) vortex shedding of a clean cylinder is pushed further away from the cylinder when the kirigami is applied to the surface. The kirigami also results in a decrease in turbulence in the wake region of the cylinder, show in Figure 2.30.

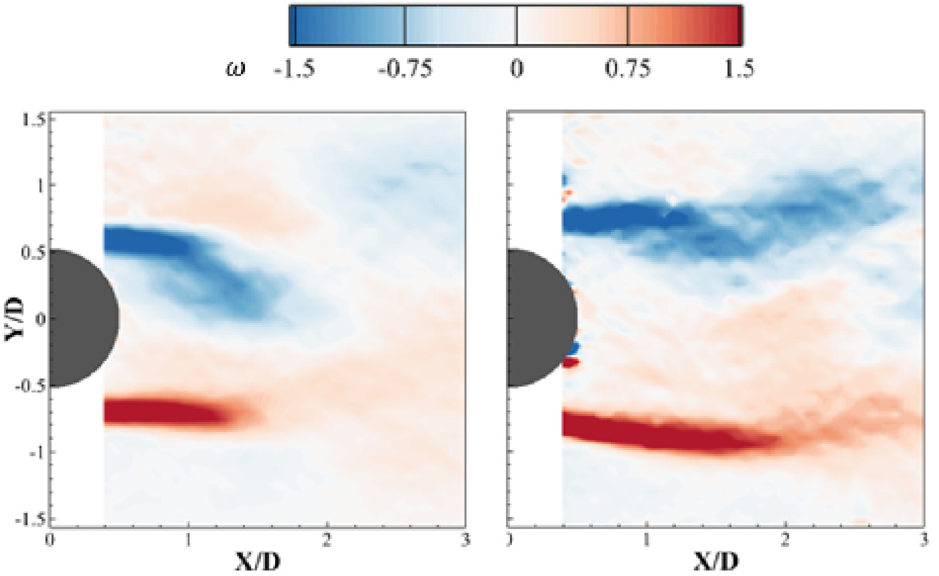

Figure 2.29: Comparison of instantaneous vorticity fields of a clean cylinder vs cylinder with circular kirigami [22]

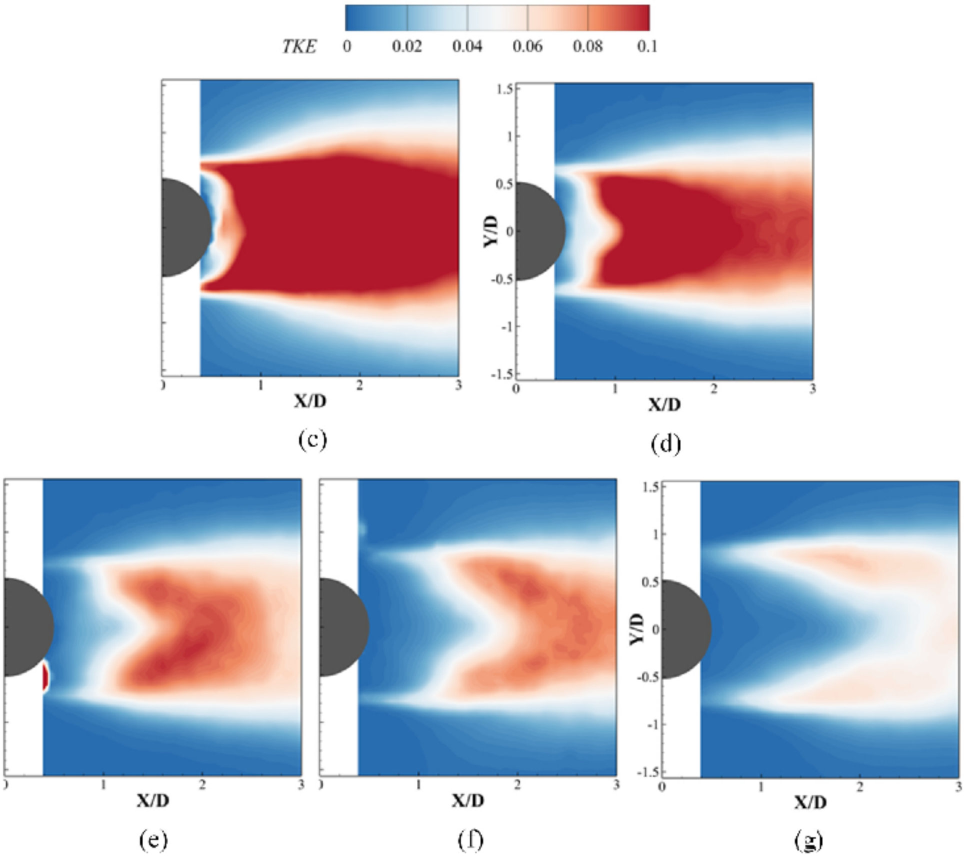

Figure 2.30: Comparison of mean turbulence kinetic energy of a clean cylinder vs cylinder with circular kirigami [22]. c.: clean cylinder, d. to g.:cylinder with circular kirigami of increasing height (ascending order)

Furthermore, the author observed that ”The shedding vortices are controlled to lose their alternate periodic patterns, but with more symmetrical shedding patterns." [22]. Further evidence for the decrease in shedding by kirigami structures is found in the significant decrease in the eigenvalues of the primary POD modes of the measured flow field. No investigation was done into the working mechanisms in the flow generated directly generated by the kirigami structures.

The available data also provides some insight into the effect on flow separation around the cylinder. Figure 2.31 shows the mean velocity fields around the cylinder.

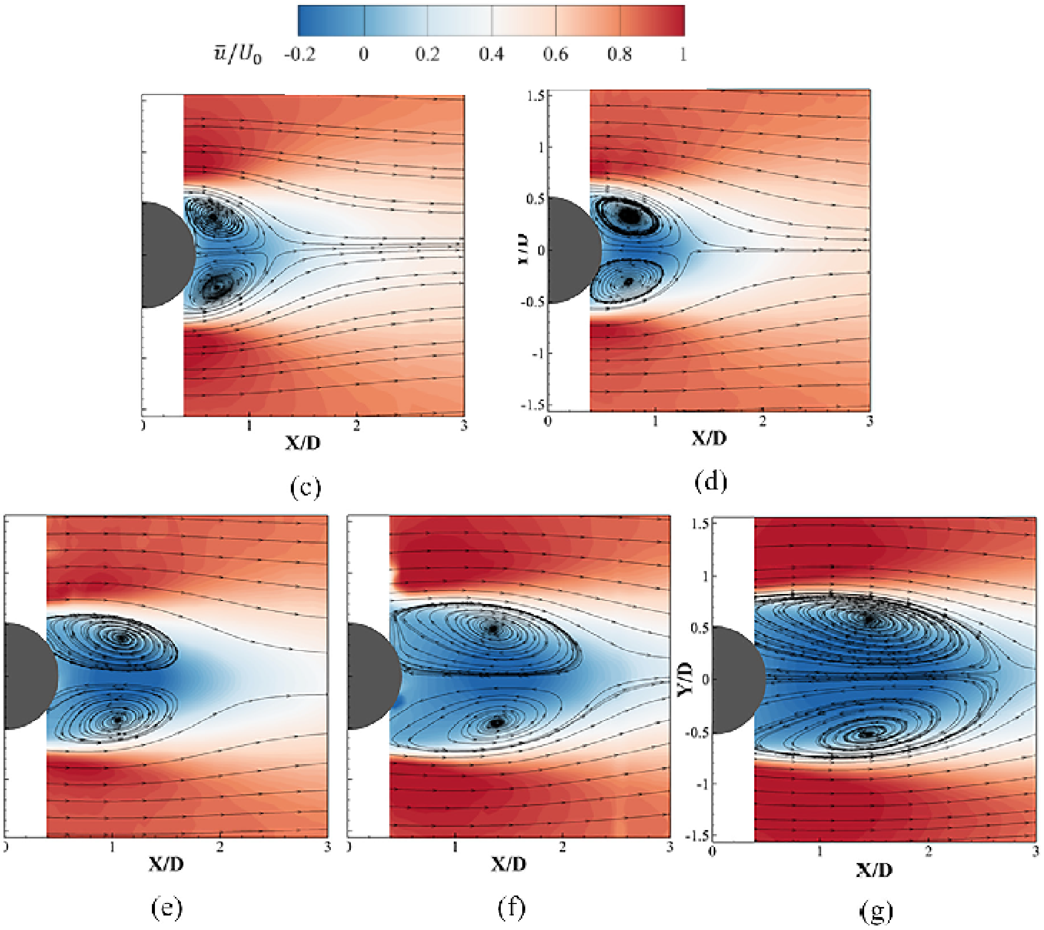

Figure 2.31: Comparison of mean velocity fields of a clean cylinder vs cylinder with circular kirigami [22]. c.: clean cylinder, d. to g.:cylinder with circular kirigami of increasing height (ascending order)

It is clear that the deployment of kirigami exacerbates the separation on the cylinder. The recirculation region in the mean flow extends continuously with larger kirigami elements, up to roughly 3 times the size of the clean case. This provides a potential explanation for the significant decrease in turbulence intensity, since, as per the findings of subsection 2.4.2, where it showed that unsteady phenomena (Reynolds stresses) reduce inside the core of separation region. In turn, the consistent increase in turbulence is also further evidence that the main mechanism at work is the exacerbation of separation.

2.9.2. Airfoil separation control with kirigami

Gamble et al. [19] is, in similar fashion to the previously discussed paper, the only known case that has attempted to apply kirigami as a flow control method on a lifting surface i.e. airfoil. The research attempts to provide kirigami separation control on a NACA0012 airfoil with a laminar boundary layer, and aims for overall drag reduction in stall conditions for long range UAV. This was carried out as an experimental campaign in a wind tunnel with chord Reynolds numbers around 200,000. The airfoil lifting properties were measured using force balances, which includes lift, drag, and yaw moments.

The experiment uses slit based out-of-plane kirigami metasurface (see Figure 2.3, Figure 2.4) that covers the entire airfoil in a static case at various deployment heights. The application is shown in

Figure 2.32. The production method used is laser cutting on a thin polyamide foil, adhered to the airfoil with double-sided tape. The dimensions of the kirigami structure were applied such that it maximised the size of the kirigami elements.

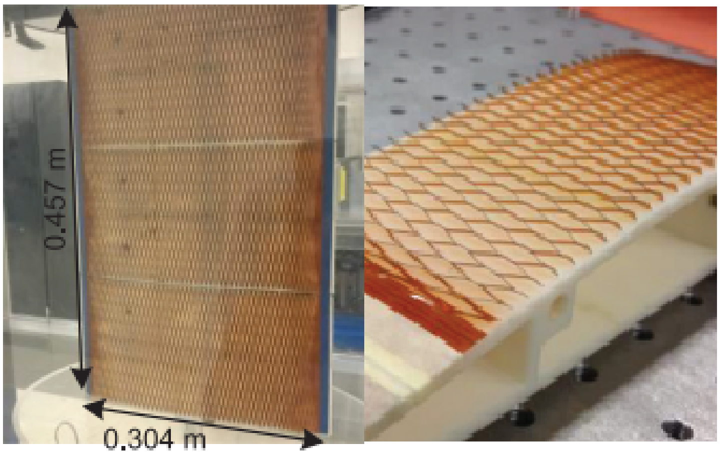

Figure 2.32: kirigami applied to an airfoil for separation control [19]

The resulting force curves can be found in Figure 2.33. The kirigami geometry of Gamble et al. was evidently unable to increase the maximum lift coefficient of the airfoil. With increased deployment, the lift over the airfoil decreases for all angles of attack. This includes a decreased maximum lift coefficient, although the stall angle at which this occurs is slightly delayed. A comparison is drawn by the author of this paper between this effect and the effect of trip strips on airfoils.

The deployment of the kirigami also appears to increases drag for most of the angles of attack. However, in the separation region of the drag curve, the drag is slightly reduced as compared to the clean configuration. This combination leads to a local positive effect on the L/D for 13 degrees angle of attack. The effect are therefore limited. This research is limited in its analysis of the flow mechanisms generated by kirigami that affect the separation on the airfoil.

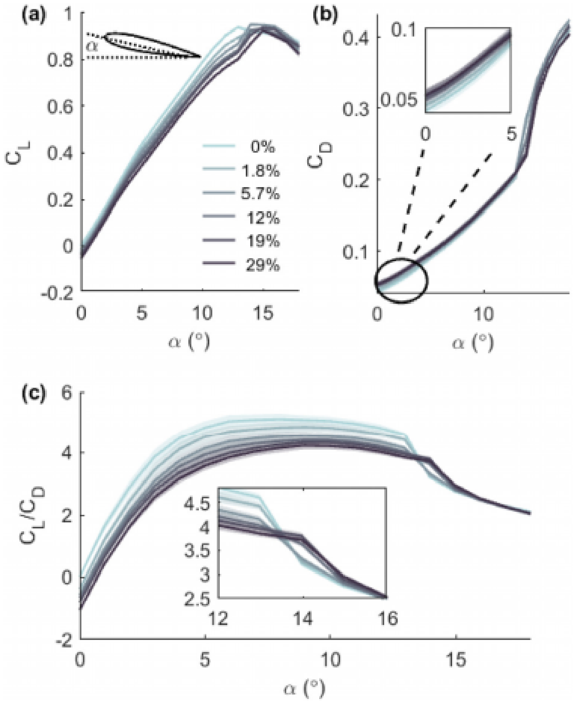

Figure 2.33: Aerodynamic force curves of the NACA0012 airfoil with kirigami deployed on the surface to varying degrees. [19]

2.10. Wind tunnel corrections

Any attempt at wind tunnel testing will introduce several discrepancies with a freestream case. A freestream benefits from far-field, uniform boundary conditions. In a wind tunnel, the boundary conditions are much closer towards the airfoil, which introduces a variety of errors in the measured forces on the wind tunnel model. A brief overview of these corrections will be given from literature. Since the experiment is carried out in an open section, the focus will be on open-jet corrections. Although open jets do not suffer from the same problem that a solid wall test section does, the boundary conditions are still different, in the form of a finite-width incoming flow and a finite distance from the model to the upstream nozzle and the downstream collector. The corrections mentioned below only concern 2D measurement set-ups for an open-jet. Since there is no distinct downstream collector in the experimental set-up, corrections pertaining to this will also be omitted.

2.10.1. Solid blockage and jet expansion

This effect is described by Mercker & Wiedemann. Continuity in the pressure field demands that the pressure at the jet boundary is equal to that of the ambient pressure. With the added presence of a solid model in the flow, this leads to curvature in the jet boundary streamlines, leading to an expanded jet. Due to mass continuity, this leads to a reduced flow velocity and thus reduced dynamic pressure at the model [74].

2.10.2. Nozzle blockage & jet deflection

The finite distance from the nozzle also poses issues. The presence of a model results in modification of the nozzle outflow. The positive pressure on the model leads to a positive pressure region that can extend into the nozzle. This results in a deceleration in some part of the nozzle, meaning that other parts accelerate due to continuity, resulting in non-uniform outflow [74]. Another effect is that proximity to the nozzle causes the streamline curvature around the object to extend into the nozzle, resulting in a further expanion of the jet [74]. Both of these affect the drag coefficient through reduction of the dynamic pressure at the model.

2.10.3. Wake blockage

The displacement of the flow by the wake also introduces bockage. Wake blockage is said to have a limited influence and is typically corrected using simplified models, i.e. a source at the wing trailing edge [75]. These methods are typically based for low angles of attack, so in order to account for largely separated flows, this is expanded upon by Maskell for separated 3D flows [75][76]. This is done by scaling the source according to the drag. Note that the method proposed by Maskell is relevant for closed sections as limited information was found on wake blockage for open sections. It is assumed that wake blockage will have the same effect on the flow as the solid blockage, apart from it being a direct function of the drag.

2.10.4. Lift interference

The jet boundary also imposes alternative boundary conditions on the flow. The condition imposed along the jet boundary is that of a zero pressure gradient. This boundary condition is then modelled in the method of images to obtain the effect that this has on the upwash at the model [77]. This results in an upwash gradient at the wind tunnel model, which in turn changes the effective angle of attack of the model with respect to the geometric attack. The method of images provides correction formulas for the angle of attack [77]. However, the correction can also be determined by correlating the measured pressure results to those of a panel code. This method was used by a study using the same experimental setup as that of the present research [78]. This method yields a correction ratio between the geometric and the effective angle of attack. However, these methods are either inviscid or have highly simplified modelling of viscous effects such as turbulent separation. The data from the latter method exemplifies that the ratio between effective and geometric angle of attack deviates from the correction ratio at high angles of attack [78].

3

Research plan and scope

3.1. Identification of research opportunities

The conclusions gathered from the literature survey in the previous chapter can serve as inspiration for a novel method of separation control. A specific type of kirigami exists that exhibits out-of-plane deployment of scale-like elements upon the application of in-plane extension, resulting in a full 3D geometry. When the extension is released, it returns back to a flat plane upon release. The deployable nature of the device provides opportunities for flow control, given that surface geometry can theoretically be modified on command.

The individual kirigami elements resemble wedge-style vortex generators, which are typically used for separation control in turbulent boundary layers. The streamwise vortices mix the outer flow with the boundary layer flow, which increases momentum near the wall and delays separation. These were also found to work in repeated configurations. The fact that vortex generators are also associated with increased parasitic drag, gives the kirigami device potential as a deployable application that only controls separation when needed.

Such a device can only be designed for practical application if a strong basis of knowledge exists on their exact fluid characteristics. Existing literature can conjecture toward this, but further testing needs to be done to expand upon the knowledge base around this topic. The present research focuses on designing an experiment to contribute to this goal in an exploratory manner, and lay a foundation for more in-depth research. Before the experiment itself can be designed, an overview of the most relevant knowledge gaps is given in the next section.

3.2. Assessment of the current state of knowledge

In the literature study, several aspects of both kirigami and turbulent separation were studied. It seems that, although kirigami-related topics (including flow control) are on the rise, the technology is still far too novel to consider an established discipline within aerodynamics. To the author's best knowledge at the time of the present research design, the use of kirigami as a flow control method only exists in two papers. Both papers present data relevant to kirigami separation control, but ultimately fall short of conclusions towards its efficacy in a more generalisable sense. The analysis around fluid dynamics around kirigami devices is furthermore limited in scope, and requires a larger, more targeted sample size with proper scaling definitions. Thus, toward the working hypothesis that kirigami metasurfaces can provide significant separation control through defined mechanisms, no formal evidence as yet exists. As such, the basis upon which this hypothesis will rest, is conceptual extrapolation in the form of drawing parallels between the geometry of kirigami metasurfaces and other flow control methods. The most eminent knowledge gaps are specified in the following paragraphs.

As highlighted, one of the main gaps of knowledge in the literature is the absence of investigation on the fluid dynamics directly around the kirigami. As evident from this literature survey, various geometries influence the separation region in different ways. The question is how kirigami modifies the separation on the airfoil, and whether this matches any known control mechanism. This should also include an explanation on how this translates to changes on the separation region and whether separation control occurs. PIV will be used to investigate only the separation region. Any characteristics of the flow around the kirigami will be inferred from these results, rather from directly measuring the flow near the device.

In terms of the design of kirigami elements, the effects of scale and shape are also undocumented. Although literature shows various results on the effect of the shape of kirigami, scale is not varied, or adapted to flow conditions in a substantiated way. These investigations on kirigami flow control are therefore inconclusive on the generalised efficacy of kirigami. More substantiated approaches to the scaling and shaping of kirigami surfaces should therefore encapsulate more of, and a more meaningful part of the design space of kirigami. Thus, toward the further exploration of this design space, questions need to be answered on the effect of the scaling of the kirigami devices on the airfoil, as well as the shape. Typically, separation control devices such as vortex generators are scaled with respect to the boundary layer, so the investigation into scaling of kirigami devices will also happen as such. To this end, investigating turbulent and roughness scaling with PIV is simply not feasible nor practical at the present time, both due to the lack of scaling laws for TBL flows in adverse pressure gradients as well as the lack of spatial resolution needed to capture the shear stress needed to calculate u_τ.

Although work on the structural design behind kirigami is more plentiful, the specific requirements for an aerodynamic application warrants more attention to design aspects. Along with this, some structurally and/or design-oriented questions should be asked. In particular, it was found that for flow control devices, the height normal to the surface is the most commonly used, and most influential scaling parameter. Although both FEM simulation and experimental testing of the out-of-plane deployment exist in literature independently, they have not been used in tandem to validate the use of FEM for this purpose. The first question is therefore whether the type of kirigami required for this test can be modelled well in FEM, so that it can be used as a design tool. The next question pertains to how adjusting the kirigami device geometry influences deployment uniformity, which is necessary to ensure spanwise uniformity for the 2D flow experiment.

The aforementioned deployability is one of the key features of interest of kirigami devices. Despite this, for the aerodynamic investigation, the kirigami devices will be tested in a static way without any form of actuation; deployment design and testing is out of scope.

The last matter to be addressed is the higher level relevance of the project. Separation control is of importance due to its striking influence on the forces of the object in the flow. By measuring the lift and drag of the airfoil, more of the emergent properties of the separation control method, and consequently, its value as a practical application will come forward.

3.3. Methodological approach

The project will be conducted experimentally in a wind tunnel. This is the conventional approach in separation control literature. This makes sense as numerical and theoretical models are insufficient for turbulent separation prediction and control, although these are improving at a rapid rate. This will be complemented by PIV to analyse the 2D flow field on the centreline of the wing. The model that will be used is a 2D wing with a DU96-W180 airfoil with trip strips to induce a turbulent boundary layer over the entire airfoil. This is due to the fact that vortex generators typically operate in turbulent boundary layers, based on the research highlighted in the literature study.

3.4. Research questions

The knowledge gap is condensed into several research questions, so as to delimit a clear scope for the project. These are as follows:

Research question 1: How do tension-activated kirigami metasurfaces affect the flow separation on a DU96 airfoil in a wind-tunnel?

- Sub-question 1: How does the mean flow in the separation region of the airfoil change when a deployed kirigami meta-surface is applied to the upper surface?
- Sub-question 2: How do the dynamics of the separation region of the airfoil change when a deployed kirigami meta-surface is applied to the airfoil upper surface?
- Sub-question 3: What flow mechanism allows kirigami to influence the separation region?
- Sub-question 4: What is the difference in effect on separation between circular and triangular kirigami cut shapes?
- Sub-question 5: What kind of scaling should be used for kirigami in the context of turbulent separation control?
- Sub-question 6: What is the effect of deploying a kirigami device on the lift and drag of the airfoil in separated flow conditions?

Research question 2: What steps need to be taken to structurally design a kirigami metasurface suitable for separation control?

- Sub-question 1: To what extent can FEM analysis effectively model the deployment height of the kirigami metasurface?
- Sub-question 2: What kirigami geometry is required for uniform deployment?

Upon these research questions, a research project can be built to advance the knowledge on kirigami flow control methods, which can subsequently lay the foundation for future research projects in this field.

4

Design of Kirigami devices for flow control

In aerodynamics, geometry design is one of the core activities of the field. Even just small-scale geometric deviations can have drastic effects on the flow field. It is therefore imperative that the geometry of the kirigami devices is chosen with great care. This chapter will highlight some of the key necessities for kirigami devices in a fluids context, the challenges in obtaining the geometry that meets these requirements, and the steps taken to come to a satisfactory design.

4.1. Structural design methodology

This section presents the methodology behind the structural design of the kirigami. This will be presented in two-fold: First, the definition and production of a kirigami device is discussed. This is followed by the derivation of the properties of the material used in the production of the devices. Then the laser-scan setup will be explained, which is finally followed by the FEM methodology.

4.1.1. Prerequisites for FEM validation

The FEM will be used primarily to obtain an ’extension curve’ of the kirigami device. Specifically, this will model the element extension height against the in-plane extension, so that the device can be designed to scale with the boundary layer. Alongside the required geometry, which will modelled in CAD software, it also requires input on the material properties. To ensure a proper comparison, material testing will be performed to obtain these. Furthermore, to then validate the FEM results, validation data is required. This will be obtained using a laser scanner, which will be used to obtain samples of the extension curve from a real-world version of the kirigami device under the same amounts of extension.

4.1.2. Geometry and production

Almost any material sheet can be turned into a kirigami metasurface. The only thing required is that the surface is thin and/or flexible enough to allow buckling along the cut-out elements, and that a production method is at hand which can accurately create the necessary cut-out pattern. On the other hand, the material does require some stiffness or thickness to retain its deployed shape under load.

Based on availability and ease-of-use, a vinyl cutter was selected as a production tool to convert vinyl-like sheets into kirigami metasurfaces. The vinyl cutter is a GCC Jaguar V J5-61(LX). The sheets used were adhesive polymer sheets compatible with the vinyl cutter, whose thickness is 115μm (excluding adhesive layer). The exact material is unknown, so material testing, as described in subsection 4.1.3, will be performed to quantify the properties of interest of the material. A vinyl cutter allows quick, accessible production of kirigami devices, and gives access to precise geometries. The vinyl cutter requires vector graphics file as input that define the cutlines. This format is built using a specific kirigami geometry parameterisation in CAD software.

Parameterisation

The parameterisation of the kirigami is as follows. First, a reference shape should be selected, which in the present research is either a triangle or a circular arc, but could for example, also be a trapezoid (see Figure 2.4). This reference shape requires 3 points to define, as shown in Figure 4.1. Figure 4.2 uses a circular arc and will serve as an example. This shape is then scaled horizontally and vertically using two parameters (L_x and L_y). This was chosen over the use of the cut angle γ, as used in literature (see section 2.2), as this parameter is only straightforward for triangular kirigami. However, it can be related to the current parameterisation through Equation 4.1.

$$tan(\gamma) = 2\frac{L_y}{L_x} \tag{4.1}$$

These elements are then laid out in a staggered-array pattern with two additional parameters for x and y spacing (δ_x and δ_y). Additionally, a slit width w_s is used to add a perpendicular offset to the reference shape, which are then connected through semicircles at the endpoints. This is done to reduce stress concentrations at the edges and prevent tearing under high loads.

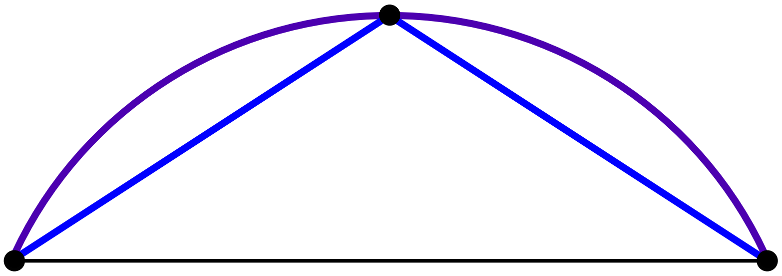

Figure 4.1: Example of a circular and triangular reference shape based on 3 points

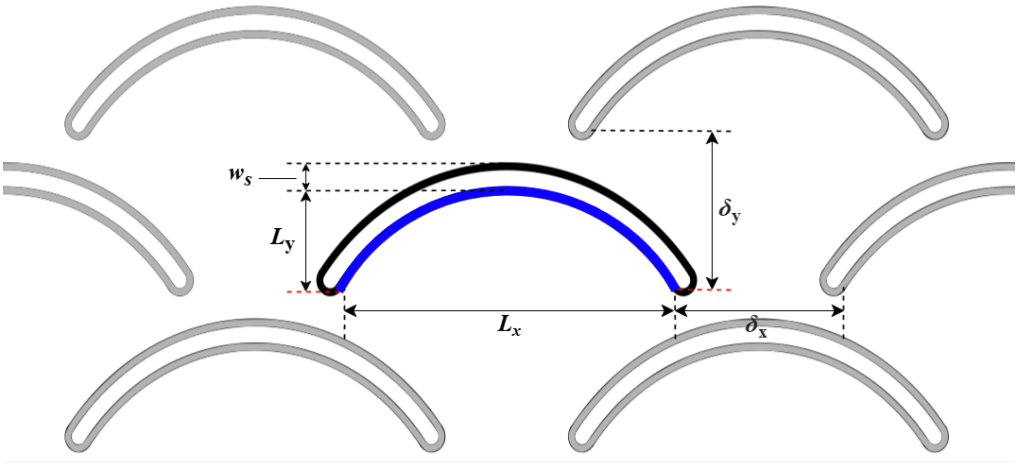

Figure 4.2: Parameterisation of kirigami geometry based on a circular reference shape

Lastly, based on the spacing parameters, the staggered array is built on the parameters N_x and N_y. This is done by making a rectangular pattern of staggered pairs of elements. What defines a staggered pair is highlighted in red in Figure 4.3. Since N_x indicate the number of pairs in x-direction, an extra column of elements is added by default at the edge of the material boundary, so that half-elements are included on each side of the geometry (indicated in blue in Figure 4.3). The number of elements in x-direction is then equal to $2N_x + 1$ and in y, $2N_y$. The staggered element of the last pair is always trimmed in half. The total length of the geometry in the y-direction is appended by a solid 'strip' with length c. The element parameterisation is visualised for a circular arc reference shape in Figure 4.2. Note that the term 'aspect ratio' is sometimes used in this report to describe this geometry. The exact terminology that is used is as follows: 'pattern aspect ratio' refers to N_y/N_x, and 'element aspect ratio' refers to L_y/L_x. The element aspect ratio directly scales with cut angle γ.

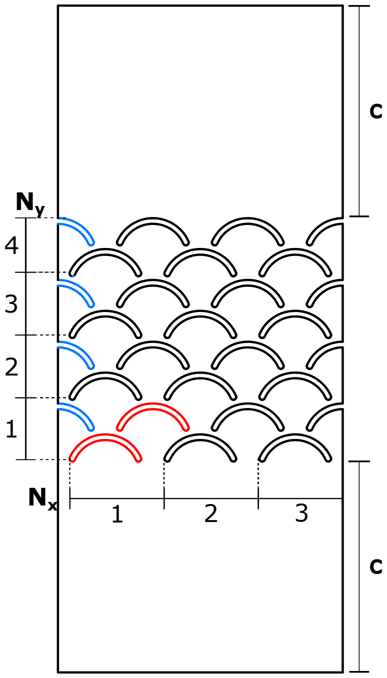

Figure 4.3: Parameterisation of circular kirigami layout with $N_x = 3$ and $N_y = 4$. Blue indicates the 'default column'. Red indicates how a single staggered pair of elements is defined

Alternative production methods

An alternative production method was attempted by producing kirigami by laser-cutting thin steel sheets: one 0.3mm thick and one 0.03mm thick. The 0.3mm was produced successfully. However, the stiffness of the 0.3mm sheet was too high, and did not allow for transverse buckling of elements under tensile loads, and required extremely high forces to even show any sign of deformation. The 0.03mm thick sheet failed to be produced due to the heat of the laser causing strong deformations in the geometry, and part of the geometry being welded to the base plate.

4.1.3. Material testing

Since third-party materials are used for the vinyl cutter, it is unknown what exactly the properties of the material are, and whether it is vinyl or not. The FEM requires the Young's Modulus and the Poisson ratio to be defined, so samples of the material will be subjected to a tensile test. This test is done in two-fold: one externally to measure the stiffness, and one in-house to measure the poisson ratio.

The tensile test is performed on a high aspect ratio strip targeting the measurements of $20mm$ x $150mm$ for the in-house measurement and $4mm$ x $20mm$ for the external measurement. Half of the samples are cut from the sheet at a 90° angle to the other half (with the groups labeled as H and V), which enables testing for isotropy. This strip is clamped between the static and extension test fixtures of a Universal Testing Machine (UTM) (seeFigure 4.5. For the in-house testing, the samples are marked with a diamond-pattern of circumpunct-style markers, as shown in Figure 4.4. This is used for visual tracking of the sample deformation, through which the poisson's ratio can be determined by tracking the distance between the horizontal points, and the distance between the vertical points. The poisson ratio is then calculated using the ratio of strains tied to these displacements, as shown in Equation 4.2.

$$\nu = -\frac{\varepsilon_x}{\varepsilon_y} \tag{4.2}$$

Using this set-up, the machine then gradually displaces one of the test fixtures to which the sample is clamped at a uniform rate until the test is terminated. The termination of the tests happens when it is determined that the sample is deforming in the plastic deformation region. The load cell of the UTM provides the force data for each of these deformations.

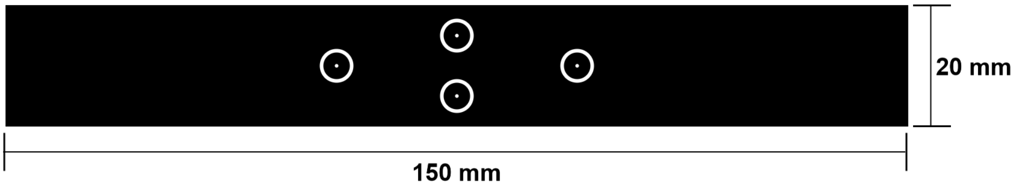

Figure 4.4: Scaled diagram of the tensile test material sample with markers

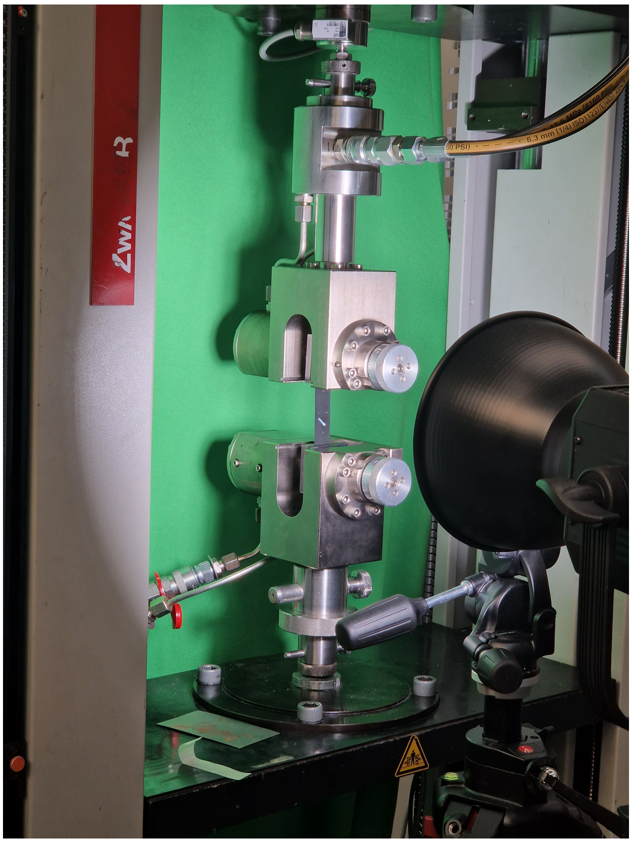

Figure 4.5: Photo of a sample in the UTM test set-up for the in-house test

Young's modulus

Figure 4.6 shows the stress-strain curves of the external test.

The curves show a relatively good overlap, showing that the test data is reliable. The vertically cut strips seem to display a slightly larger stiffness in the elastic region, and a slightly lower one in the plastic region. Table 4.1 shows the measured Young's moduli based on the average slope of the elastic region, from which it is evident that the material stiffness is not entirely isotropic. However, for the purposes of

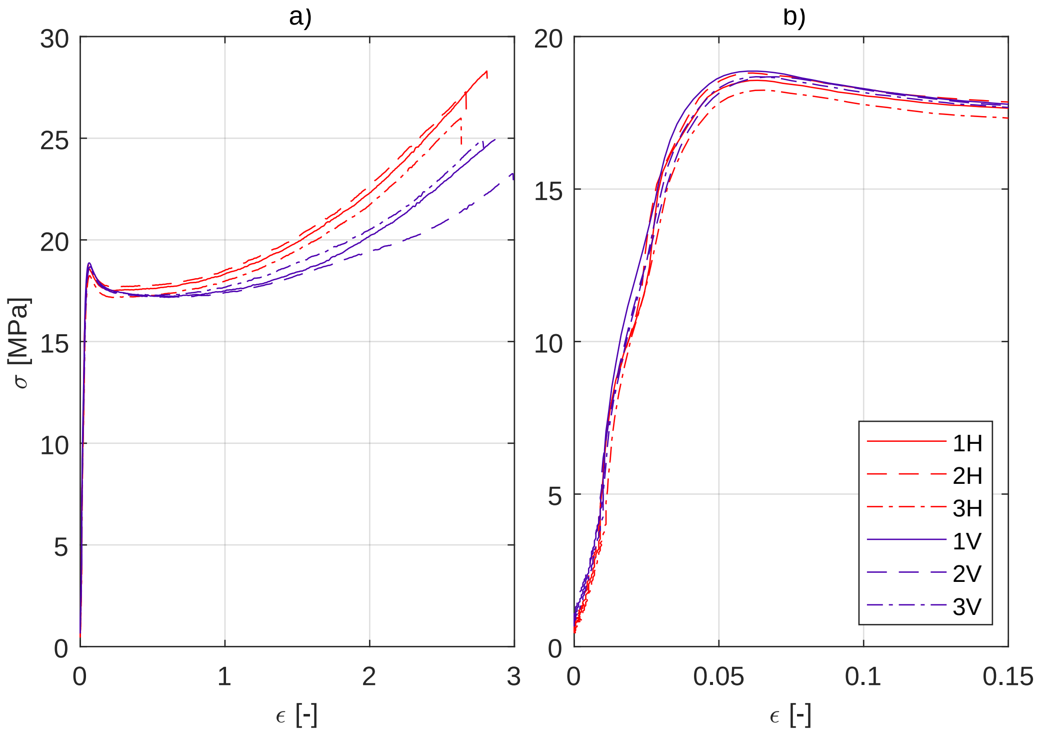

Figure 4.6: Stress-Strain curve of the external material test at a) full size, b) zoomed in to the elastic and yielding region

this thesis, the 15% difference between the horizontal and vertical stiffness will be considered negligible, implying an isotropic material, and an average Young's Modulus of $E = 300$ MPa will be assumed.

E moduli [MPa]	H	V
1	267.73	330.96
2	298.47	285.75
3	259.68	350.74
mean	275.26	322.48

Table 4.1: Measured young's moduli of tensile test

The values given by the external testing were obtained by fitting a line between the origin and the peak stress in the elastic-yield region (right figure on Figure 4.6). However, the typical approach is to fit a curve only to the elastic region. This might result in some error, although it will be assumed that for the FEM, only a rough approximation is required of the young's modulus.

Poisson ratio

The poission ratio could not be determined by tracking the horizontal markers, due to large warping of the marker shape compared to the relatively small horizontal displacements. Instead, the markers were used as a reference to track the vertical location of the horizontal centreline of the strip, and the edges of the strip at this vertical location were instead used to determine the horizontal strain. The vertical strain could still be measured by tracking the position of the vertical markers.

The resulting strains from the horizontal and vertical tracks appear to show a good, consistent linear fit for the equation $-\epsilon_x = \nu\epsilon_y$, where ν is the Poisson ratio. This is shown for the four test cases in Figure 4.7.

Using the slope of these linear fits, the poisson ratio is determined. The results are shown in Table 4.2. A poisson ratio rounded to $\nu = 0.46$ will be used for the purposes of this thesis.

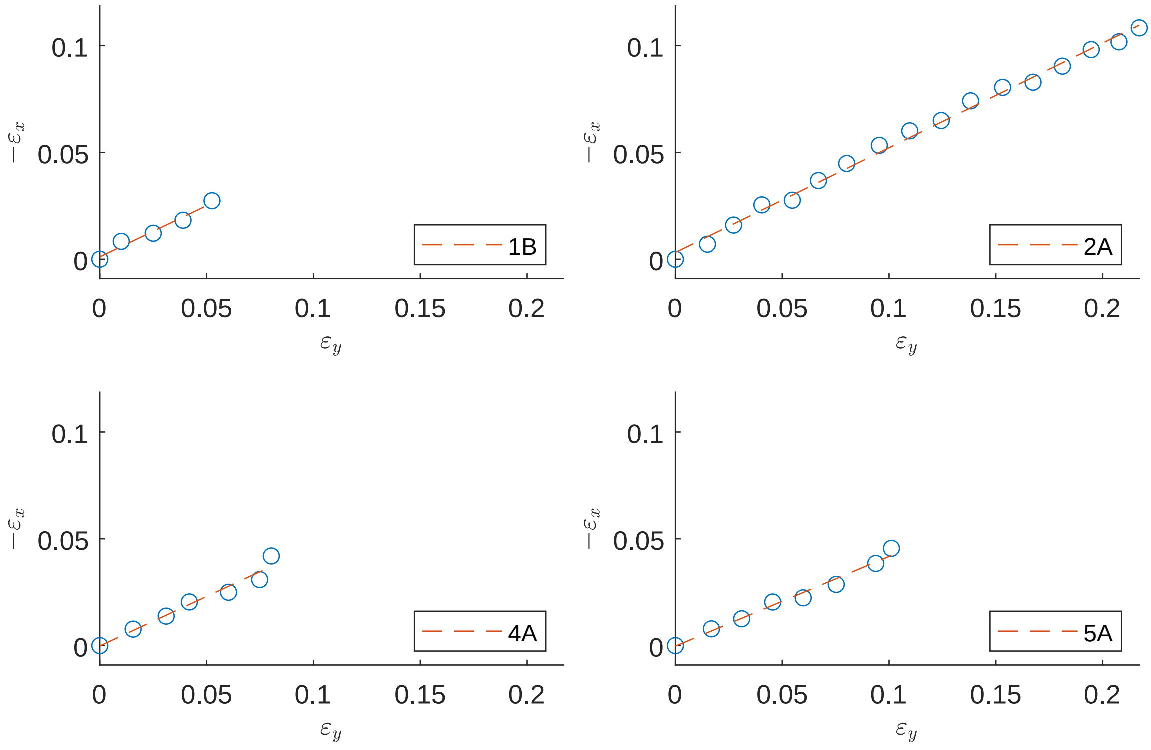

Figure 4.7: Strain plots resulting from the tensile test visual tracking

ID	1B	2A	4A	5A	$\mu \pm \sigma$
ν **[-]**	0.4794	0.4901	0.4634	0.4197	0.4632 $\pm$ 0.031

Table 4.2: Poisson ratios determined from visual tracking

4.1.4. Laser scanning

In order to validate the results of the FEM and obtain the deployment height of any kirigami devices used during the experiment, some measurement technique is required. For this, a laser scanner is used, specifically the scanCONTROL 30x0[1]. The scanning methodology in question uses laser triangulation, which involves projecting a laser beam onto a surface, and capturing the light by an sensor that is offset from the emitter (see Figure 4.8, taken from SICK sensor intelligence[2]). The distance between the emitter and the surface is determined by the angle between the incoming and outgoing beam. Triangulation-based scanners only work in a limited range, but for the small deployments heights of the kirigami in the present research, this range will be sufficient.

Experimental set-up

The laser scanner is mounted on a horizontal 1-axis traverse system, which is in turn mounted to an ISB-beam structure that allows height adjustment of the scanning axis so that the entire geometry is within the scan range (indicated by h in Figure 4.9). h needs to be between 77.5mm and 92.5mm for the scanner in question. The laser scanner is only capable of scanning the surface height and width on a single transverse line, so in order to obtain a full 3D geometry of a planar scan, the traverse moves the laser scanner along the kirigami (the 'scan direction'), perpendicularly to this line to sweep across the entire geometry (see Figure 4.9). The kirigami is attached by each end to the top of a bench vise, to allow for controlled extension of the geometry.

---

[1] `https://www.micro-epsilon.com/2d-3d-measurement/laser-profile-scanners/scancontrol-30x0/`

[2] `https://www.sick.com/media/docs/9/39/539/product_information_laser_triangulation_sensors_dt20_hi_od_value_od1000_od_mini_od_max_od_precision_od5000_en_im0053539.pdf`

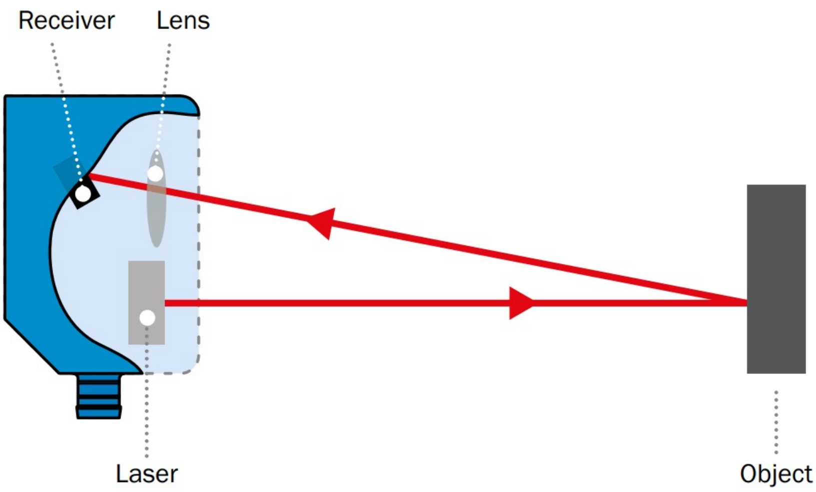

Figure 4.8: Diagram of triangulation-based laser scanner[2]

Post-processing

The resulting data comes in the form of individual height profiles with their respective x-location and a profile number N for each y-location in the scan direction. If the profile rate is constant, the y-coordinate can be derived from the profile rate and the traverse speed. However, when the profile rate is variable, the ratio between y and profiles needs to be derived from the geometry itself. This can be done by taking the profile number difference at two points with a known y-spacing. When the total extension length of the kirigami with a solid strip is known, the assumption is made that the stiffness of the strip under tension is much larger than that of the kirigami geometry. This implies that the extension of the total device is equal to the extension of the kirigami geometry, the range of which is fully included in the scan results.

Furthermore, the resulting scan geometry is not always straight (either tilted to the side or having a slope downwards along the scan direction). The z-coordinate is also not calibrated to a reference value. This is corrected for by selecting two y-locations known to be on a flat plane, preferably locations where z varies little and where the resulting z coordinate serves as a sensible reference for extension (e.g. on the kirigami strip). At each of these locations, the z-coordinate is averaged across x to obtain a reference z-coordinate. The reference x-coordinate for each point is set the centreline of the kirigami geometry (not to the centreline of the scan geometry). Using these two reference points, the geometry is first translated such that one of the points is the origin, and then the geometry is rotated around the origin such that both points are on $z = 0$.

4.2. Finite-element method

A Finite-Element Method (FEM) analysis uses numerical simulation of structural mechanics to approximate real structural deformations. This allows for swift access to a wide range of designs and detailed results without the material cost or the labour required for production. This is done using external software, COMSOL Multiphysics.

4.2.1. Simulation set-up

The simulation is performed using a stationary shell model. For the shell model, the geometry is derived from a cross-section of the solid geometry imported from CAD, to which a 'thickness and offset' operation is applied. Both of these are then modelled with a linear elastic material, i.e. $\frac{d\sigma}{d\varepsilon} = const.$. Although some plastic deformations were observed on physical kirigami models upon releasing larger extensions, the assumption is made that a linear elastic material is sufficient for modelling the behaviour and the extension height of the kirigami.

Four unique boundary conditions are then applied to a symmetric kirigami model after the geometry has been trimmed at its symmetric axis: One 'fixed constraint' boundary condition on one edge of

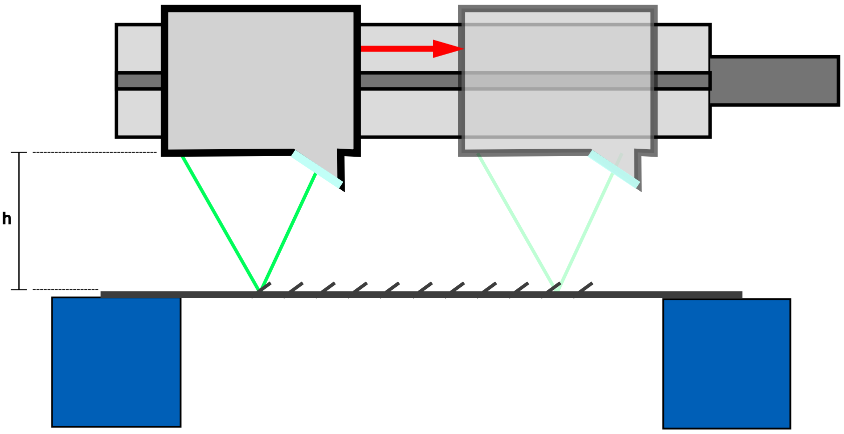

Figure 4.9: Scanner set-up

the kirigami extension direction, one ’fixed displacement’ on the opposite edge to the fixed constraint, a symmetry condition on any edge that emerged from the symmetric geometry trimming, and a free boundary condition on any remaining edge. Additionally, due to the bistable nature of kirigami elements, the solver could converge to any solution involving any combination of elements being either deflected up or downward. Since only two of these solutions are interesting (either all upward or all downward), some additional boundary conditions are imposed. One method is to simply apply gravity to the whole domain, creating a bias to one side. This gravity is applied at the first step and its strength is tapered off to zero in the first few extension steps. Additionally, when using gravity alone does not lead to convergence, a point force is applied in these first few steps to the apex of every kirigami element, forcing them to deploy in one direction.

The geometry is discretised using a triangular mesh with quadratic serendepity discretisation for the solid mechanics model, and a quadrilateral mesh with quadratic discretisation for the shell model. The system is then solved using the MUMPS algorithm, fully coupled. Some damping factor is recommended to prevent significant overshoots of the solution, along with a relatively large number of iterations.

4.3. Kirigami design results

This section presents the results of the kirigami design steps undertaken in this chapter. First, the validation of the FEM is presented. Then, a design approach to improve deployment uniformity is discussed. Lastly, a final design of the kirigami device for the wind tunnel experiment is proposed.

4.3.1. Deployment height

The use FEM to model the deployment height of the kirigami, must first be validated for the present kirigami use cases. The results of these simulations are shown in Figure 4.10 and Figure 4.11, where the FEM results are compared to the laser scan results. Figure 4.10 shows the normalised peak deployment height on the centreline of the kirigami model versus the in-plane extension of the kirigami. This peak value is what will be used as the reference device height h in this report.

The FEM shell model deployment height overlaps closely with the laser scanned model for both the circular and the triangular kirigami case, even with these being of different L_x thus evidently provides a close approximation of the real life case.

The general behaviour of the kirigami seems to consist of a steep deployment gradient for smaller ex-

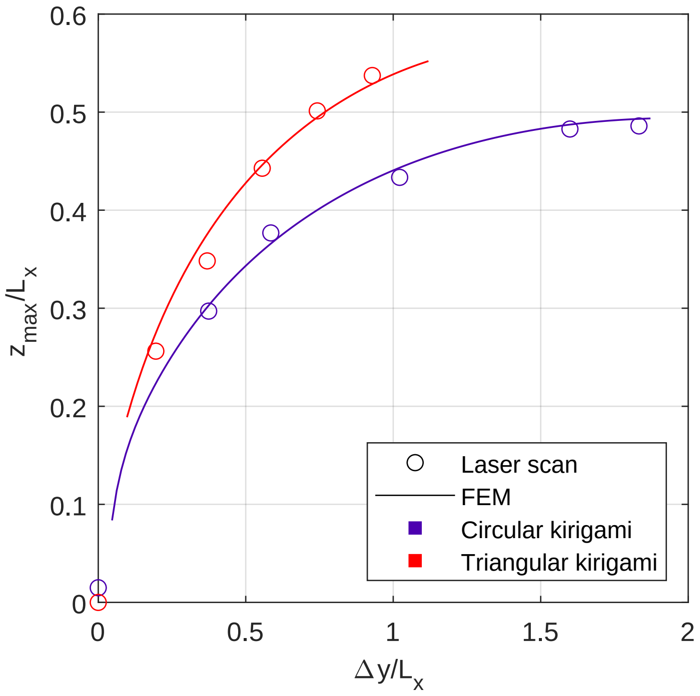

Figure 4.10: Deployment curves of the kirigami FEM simulations compared to real-life laser scanned models

tensions, which flattens off for larger extensions. It seems that, for this element aspect ratio, it appears that z_{max}/L_x is in the order of 0.5 for large extensions. Although a larger sample is required to generalise this similarity, this assumption will suffice for the purposes of obtaining a first-order estimate of deployment height. The behaviour of the curve also resembles the measurements from literature in Figure 2.7 [23], with the maximum slope of deployment happening at the start of the extension, and a gradual stagnation at higher extensions. Both results also are of similar order of magnitude in deployment height for larger extensions.

Additionally, to observe whether FEM can predict the deployment and deformation behaviour of the kirigami, a 2D contour plot of the kirigami deployment height is shown in Figure 4.11. The figure shows both the simulated kirigami and a laser scanned testpiece at the same extension length (note: the limited span shown in the figure is due to limitations on the laser scan width).

The figure shows a striking similarity between the FEM model and the real-life case. It successfully models both the contraction and deformation of the kirigami lay-out, as well as the topology of individual elements. The simulation gives a good representation of the general deployment pattern of the kirigami. This figure also confirms that all simulated elements have deployed in the same direction, as intended. The same does not hold for the laser scanned samples, where some of the elements have deployed in the opposite direction, which demonstrates the bistable nature of the kirigami elements.

One noteworthy observation from the 2D layout is the strong contraction resulting from the buckling of the kirigami elements, in tandem with the significant non-unform deployment front at the start and end of the kirigami. The free edges on the side of the kirigami play a crucial role in providing the elements the degree of freedom to buckle by propagating transverse deformation to the neighbouring elements. The drawback of this mechanism however, is the fact that the elements at the start and end are not subjected to this same propagation of deformation from the edges, resulting in triangular front of various levels of constrained deployment. It can also be observed that the deployment height tends to drop off toward the edges.

Both of these effects might prove troublesome for reliable deployment at pattern aspect ratios smaller than 1, where the free edges are unable to fully propagate towards the middle. This results in significant non-uniformity in deployment heights and in the elements' shapes and positions in deformed kirigami lattice, particularly at the centreline, where all the aerodynamic measurements will be performed (see subsection 5.2.2). To alleviate this, a solution is proposed along an underlying hypothetical cause in

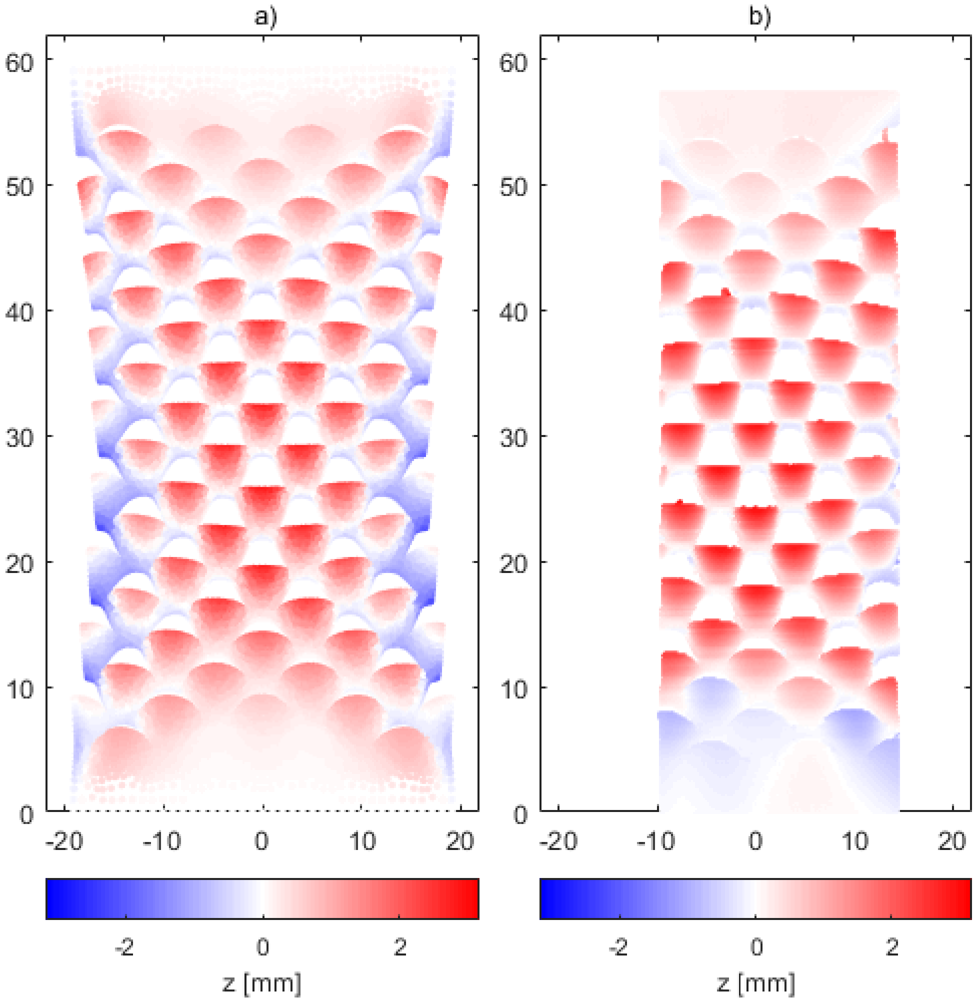

Figure 4.11: 2D comparison of the out-of-plane deployment of: a) the FEM simulated kirigami and b) A laser-scanned sample of the same kirigami geometry, both at an extension of $\Delta y = 6.6mm$.

subsection 4.3.2.

4.3.2. Deployment uniformity

To alleviate the non-uniformity in the deployment, the underlying cause is identified in this section, and a design modifications is proposed.

It is hypothesises that the solid strip at the start and end of the kirigami is strongly constrained in buckling. This comes both from its own stiffness as well as from typical fixed constraints that occur near this area, whether this is an artificial FEM boundary conditions, or a real life physical restraint, such as clamping, or adhesion to an underlying surface. This buckling constraint propagates towards the rest of the kirigami, resulting in restricted buckling of kirigami elements near the strips. Conversely, if either the strip is allowed to buckle more, or the buckling resistance is removed altogether, the deployment might be much more uniform. One way to achieve the former is to move the fixing constraint infinitely far away from the kirigami, such that the material near the kirigami is unaffected by this restriction. However, this is not practical in real applications, so a more promising method is to cut slots out of the kirigami strip, as shown in Figure 4.12.

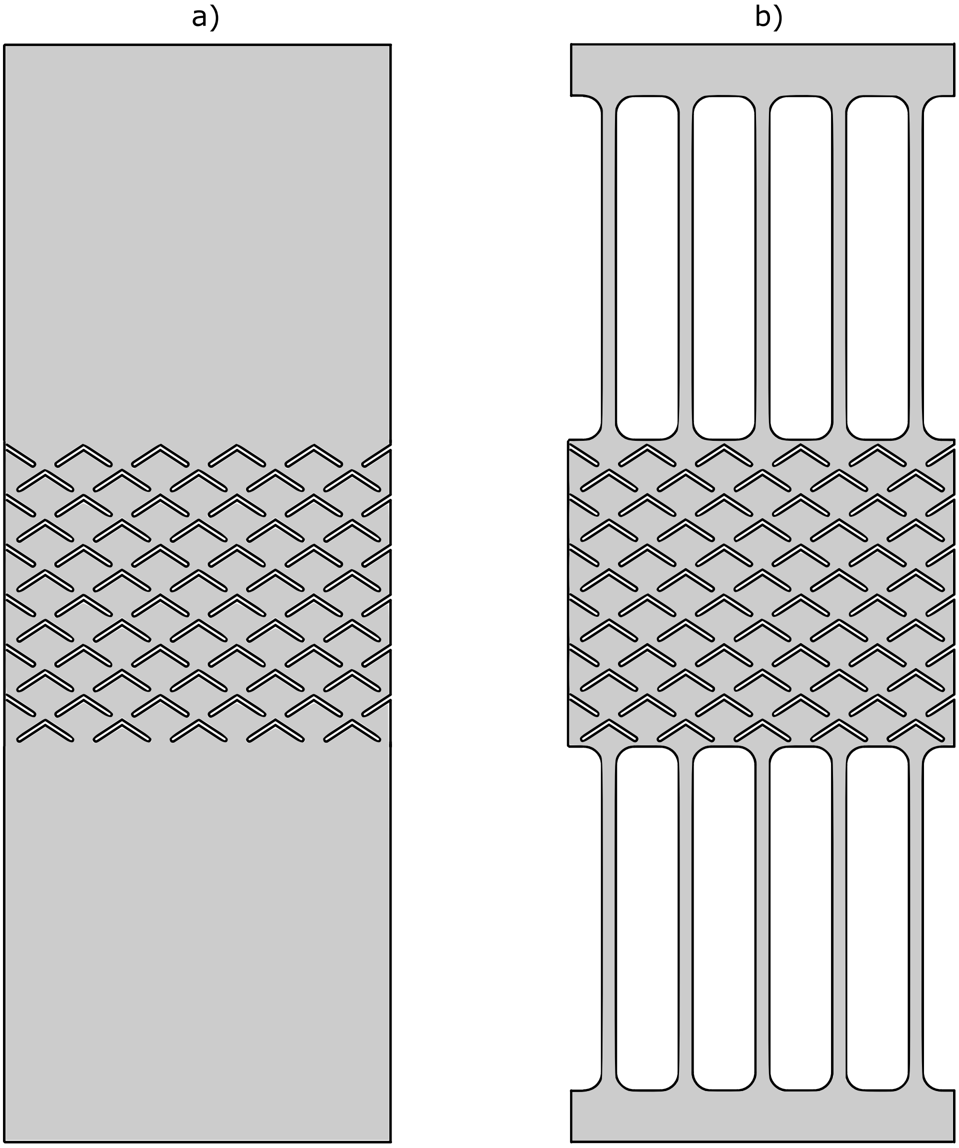

Figure 4.12: An example of strip cuts in a triangular kirigami device, showing one device a) without and b) with strip cuts

The strip cuts are made using cut rounded rectangular shapes. These strip cuts can be parameterised based on 4 parameters. The first step is to place an pattern of rectangles with their centreline collinear to that of the first staggered row of kirigami elements. These rectangles are placed at a distance c_s from the starting edge of the kirigami strip, and a distance Δ_y from the first row of elements. These rectangles are spaced apart at a distance Δ_x. The corners of the rectangles are rounded using a radius r_s. This parameterisation is visualised in Figure 4.13.

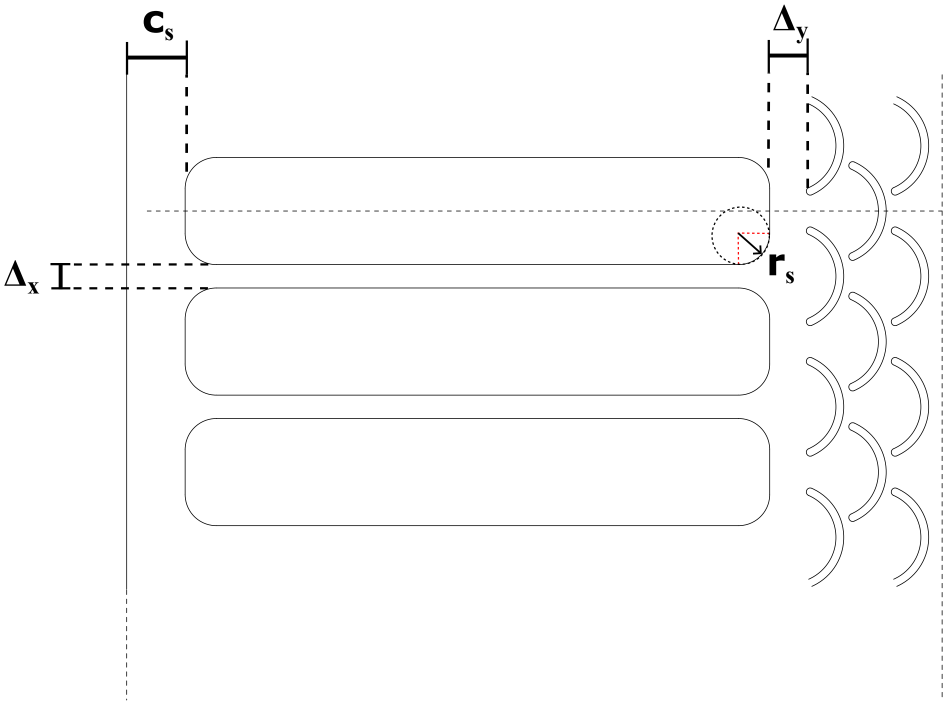

Figure 4.13: Parameterisation of the strip cut geometry

This allows for the remaining material strips inbetween the rectangular cutouts to free move transversely upon extension of the kirigami device, as opposed to the strip having to overcome its own transverse buckling resistance. This also enables the effect of faraway clamping to be much more effective. Figure 4.14 shows a FEM simulation of the same two triangular kirigami geometries, one with strip cuts and one without. The buckling resistance of the model without strip cuts is modelled by having a fixed boundary condition right before the start of the kirigami geometry.

The solid strip case shows excessive contraction and non-uniformity, whereas the case with strip cuts shows strong uniformity, showing the effectivity of the strip cuts in tackling the problem at hand. The case with strip cuts shows a complete absence of the triangular non-uniform front that is exhibited by the solid strip case and the cases in Figure 4.11. To support this effectiveness with a quantitative comparison, the peak deployment height of each element on the centreline for the above geometries is plotted for both cases in Figure 4.15.

In this figure, the uniformity enabled by the strip cuts becomes more apparent. The deployment peaks of the case with strip cuts exhibits a much flatter distribution than the one without. A side-effect that becomes evident from this figure is the increased deployment height, which is presumably due to the additional freedom for elements to buckle that the strip cuts enable.

Another note-worthy side-effect is that the remains of the strip at the start of the kirigami exhibit an oscillatory buckling pattern (see $y \approx 47.5mm$ in Figure 4.14b). Although this would theoretically create additional surface geometry that could have an effect on the flow, in practice it was observed that these can be flattened or cut away once the kirigami was glued onto a surface.

Although not formalised in the current results, it was observed in practice that, on production pieces with very low pattern aspect ratios and strip cuts, this uniformity persisted across the entire span of the kirigami geometry. This proves that strip cuts are an extremely effective and practical technique to design unformly deployed kirigami metasurfaces for aerodynamic purposes.

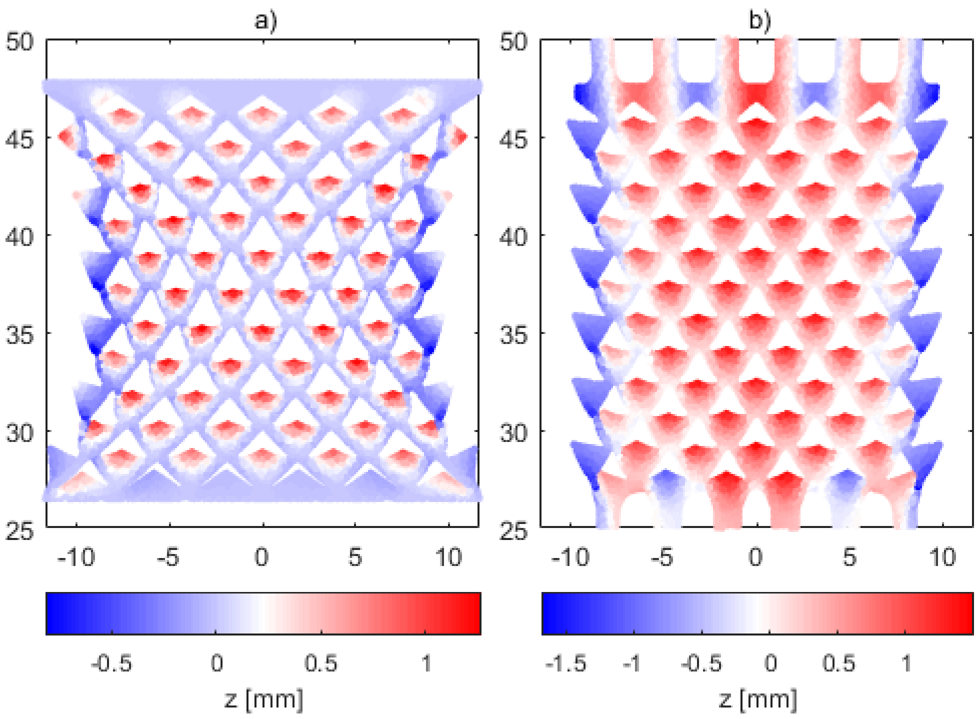

Figure 4.14: 2D FEM comparison of the out-of-plane deployment height of the same triangular kirigami device at the same y-extension with: a) A fixed boundary constraint near the start and end of the kirigami and b) A fixed boundary constraint at the end of the kirigami strip with strip cuts

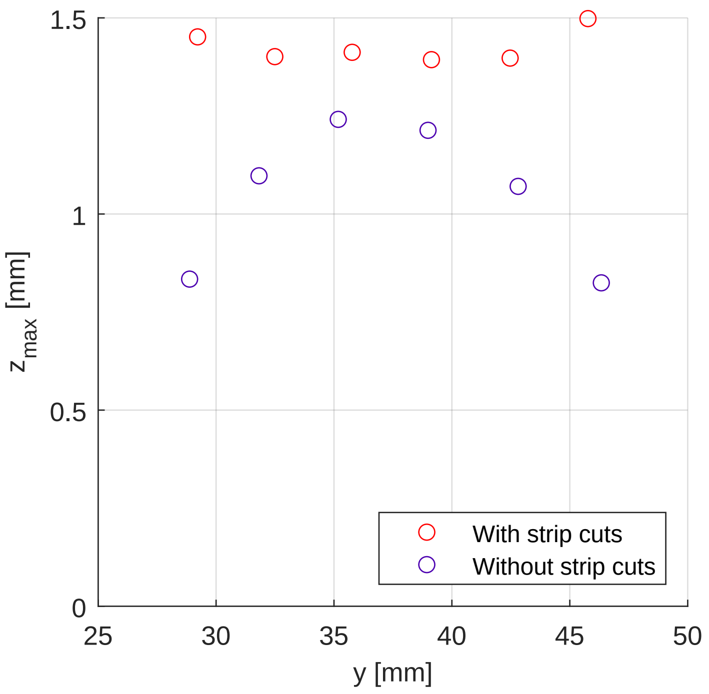

Figure 4.15: Deployment peaks of individual kirigami elements on the centreline of FEM-simulated kirigami geometry with and without strip cuts

4.3.3. Final design

With the conclusions gathered from the FEM, along with some other design considerations, a final design for the experiment was put together.

Proper 2D testing necessitates spanwise flow uniformity, which is why the number of elements in spanwise direction will be such that the width of the kirigami device will be equal to the width of the 2D wing (400mm). Since the aim is to study the effects of a localised device (like a vortex generator), as well test a variation of spacings between the separation point and the chordwise location of the kirigami, it makes sense to keep the number of elements in chordwise (x)-direction of the kirigami as limited as possible. A low surface coverage is also desirable to minimise any adverse effects of the kirigami on separation in case it functions like a roughness and results in a momentum deficit. Choosing too few elements results in issues with deployment, so a balance was struck of 6 element pairs in x-direction, which results in about $0.15c$ surface coverage.

The spacing of elements (gap size) was manually tuned to ensure unrestricted deployment of the elements without breaking. These are set specifically such that the linear vertices of the triangular elements are on the same diagonal line (as is done in past kirigami studies using the same geometry). Past research using the same airfoil with boundary layer tripping has approximated the boundary layer thickness on the airfoil at the trailing edge to be in the order of 10-15mm for low to medium angles of attack[79]. With this in mind, an element width L_x of $4.3mm$ (as was used for some of the proven test pieces made with the vinyl cutter) was deemed sufficient to target the scale of micro-vortex generators of $h/\delta = 0.1 - 0.3$. The sharpness of the kirigami apex is preferably maximised so that it is more similar to the more acute angles used for wedge-style vortex. However, this also affects deployability (see section 2.2). Deployment is maximised at a cut angle of 30 degrees [23], so L_y was chosen to be just over 30 degrees. The final designs are shown in Figure 4.16

Parameter	**Circular Kirigami**	**Triangular Kirigami**	**Unit**
Element width (L_x)	4.3	”	mm
Element length (L_y)	1.4	”	mm
Element spacing (x) (δ_x)	2.4	”	mm
Element spacing (y) (δ_y)	2.18	”	mm
Slit width (w_s)	0.5	0.4	mm
Number of Element pairs (x) (N_x)	6	”	-
Number of Element pairs (y) (N_y)	45	”	-
Solid strip length (c)	35	”	mm
Strip cut edge width (c_s)	4.5	”	mm
Strip cut offset (Δ_y)	1.2	”	mm
Strip cut spacing (x) (Δ_x)	0.5	”	mm
Strip cut corner radius (r_s)	1.6	”	mm
Deployed extension (Δy)	4.6	”	mm

Table 4.3: Final design parameterisation of the kirigami geometry

Figure 4.16 shows the full geometry of the unextended kirigami device.

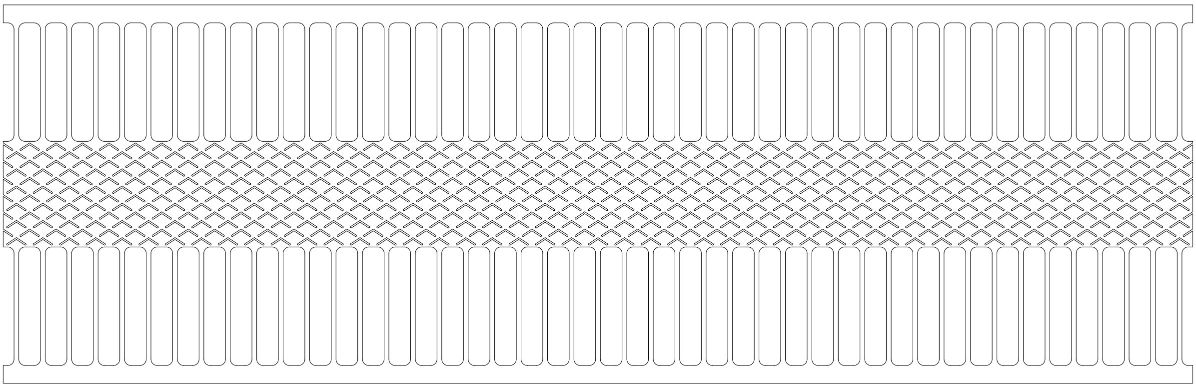

(a) Triangular

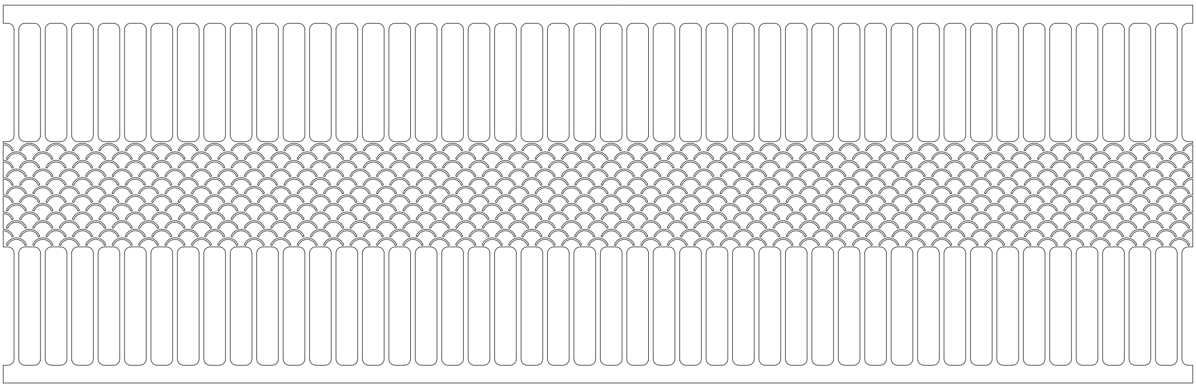

(b) Circular

Figure 4.16: Final designs of the kirigami geometry

5

Turbulent separation control using Kirigami

With a structural design completed, the aerodynamic characteristics of kirigami can be tested in the wind tunnel, where its capabilities in separation control were assessed. First, a baseline overview of the airfoil and its separation characteristics will be given, followed by an assessment of a comparison of the airfoil separation characteristics for specific cases of interest. Lastly, several hypotheses for the changes in separation will be described, based on the data available.

5.1. Test plan

In the wind tunnel experiment in question, two parameters can be controlled to set specific flow conditions: the tunnel flow velocity U_∞ and the geometric angle of attack of the airfoil α_{geom}. Varying these parameters implicitly varies the pressure gradient $\frac{dp}{dx}$ on the airfoil and the Reynolds number Re, which in turn affect boundary layer thickness δ and the separation point x_{sep}. In varying these parameters, a large design space can be studied for potential separation control effects.

The geometric angle of attack α_{geom} was varied between 6 degrees and 20 degrees to capture the full spectrum of stall on the airfoil, from no separation to full separation. Each angle of attack is measured at a U_∞ from $10m/s$ to $30m/s$ for a total of 40 cases. For each tunnel velocity, the angle of attack is varied in ascending order to prevent hysteresis effects. This process is done for a clean configuration, a configuration with the circular kirigami and a configuration with the triangular kirigami.

5.2. Experimental set-up

5.2.1. Wind tunnel model

Airfoil

The model used for the aerodynamics part of the experiment is a 2D wing with a DU96-W-180 airfoil, a 200mm chord, and a span of 400mm. Its cross-section is shown in Figure 5.1.

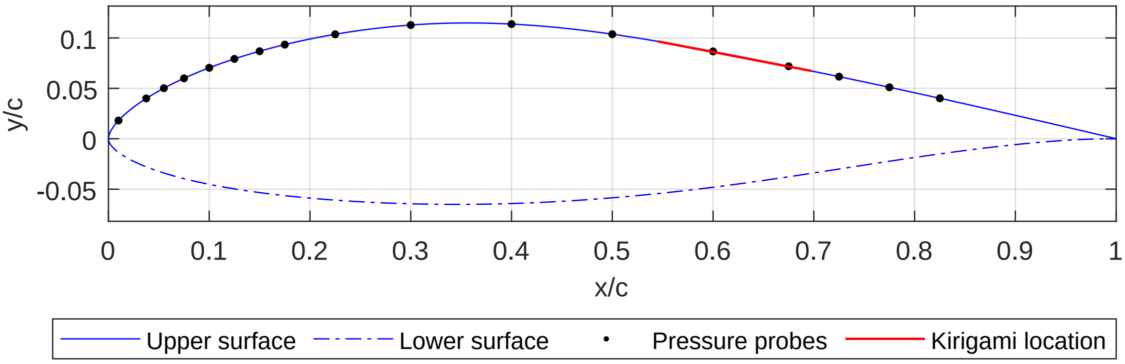

Figure 5.1: DU96-W-180 airfoil used in the experiment with available pressure taps and kirigami placement

The airfoil was chosen partly due to availability, but also due to its thickness and flat aft upper surface. To ensure a turbulent boundary layer, even at low Reynolds numbers, the boundary layer was tripped by means of a zig-zag strip near the trailing edge. The flat aft upper surface of the airfoil allows for easier application of the kirigami surface.

Figure 5.2 [79] shows the characteristic pressure distribution around the DU96 airfoil. Due to the relatively small leading-edge radius, a sharp suction peak is observed, that quickly decreases, briefly resurges to a secondary suction peak as the curvature of the airfoil increases again, and then recovers with a relatively constant pressure gradient.

To measure how the kirigami affects this pressure distribution, the airfoil is equipped with pressure taps on both the upper surface and lower surface. The upper surface probes will be used to characterise the airfoil's pressure profile that leads to separation. The pressure taps are connected to pressure probe which record a time-averaged pressure for each tap over 30 seconds. To account for the more significant peaks in pressure near the leading edge, ressure taps at $x/c < 0.2$ are connected to a probe with a measuring range of $\Delta p = \pm 2.5\ kPa$, whereas taps at $x/c > 0.2$ were connected to a probe with a range of $\Delta p = \pm 600\ Pa$. The measurements are done over a period of 30 seconds, which results in a time-averaged pressure for each probe.

Kirigami placement

Based on the range of angles of attack, a large variation of separation points (measured as point of TD: Transitory Detachment near the surface) will be observed. In early observations during the test, it was observed that this variation of separation point occurs between $0.36 \leq x/c \leq 1.0$ for all tunnel velocities (see Figure 5.15), so the choice was made to place the kirigami somewhere in the middle of this range. Specifically, the start of the kirigami structure was placed 93mm from the trailing edge, measured along the upper surface. This corresponds to a start and end point of respectively $0.55c$ and $0.70c$ and is indicated in red in Figure 5.1. This start and endpoint are defined as the chord-wise bounds of the actual kirigami structure, meaning it excludes the strip. Note that due to this placement, some pressure taps might be covered up and not function as intended.

The kirigami was extended to a length of $100.45mm$ by adhering the extreme edges of the strips to a bracket with the adhesive side outwards, and then placing it at the abovementioned location on the airfoil such that the centre of the kirigami was aligned with the centre of the wing, with the apices of the deployed kirigami elements pointing downstream. Note that due to the bistable nature of the kirigami elements as a result of the isotropic material, some elements need to be pushed manually to deploy in the correct direction.

To minimise interference of the strips, these were cut off as close as possible to the deployed kirigami lattice, and removed from the airfoil surface. The adhesive surface of the vinyl-like material was sufficient to keep the kirigami structure deployed in place.

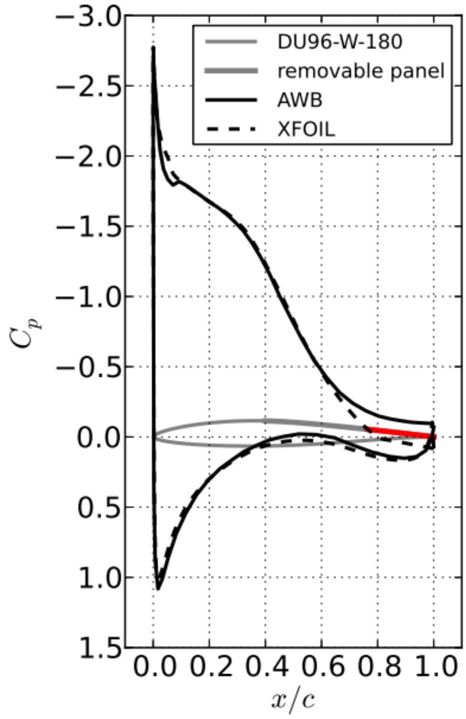

Figure 5.2: Characteristic pressure distribution around a DU96-W-180 airfoil at moderate angle of attack based on wind tunnel tests (AWB) and panel simulations (XFOIL) by Suryadi & Herr[79]

5.2.2. Wind tunnel hardware set-up

Wind tunnel

The tunnel used was the A-Tunnel facility at the Low-speed Wind Tunnel Laboratory at Delft University of Technology. All the following information about this tunnel is taken from Merino-Martínez et al. [80]. The A-Tunnel is an anechoic low-turbulence, vertical, open-jet, closed-circuit wind tunnel intended for aeroacoustic measurements, and transition and flow control studies. A schematic of the wind tunnel is shown in Figure 5.3. The measurements were performed in the open-jet test section located in the anechoic plenum. The particle seeding hardware was located on the top floor. For this test setup, a Delft 40x70 contraction was mounted at the exit of the contraction. This has a contraction ratio of 15:1, and allows a maximum outlet velocity of 35 m/s. With this contraction, the outlet has a worst-case flow non-uniformity of -0.8% and a maximum streamwise velocity turbulence intensity of 0.1% for velocities of 10 m/s and above.

The tunnel velocity is measured using a pitot tube upstream of the airfoil. Other properties of the tunnel that can be measured are the freestream density and temperature. Since data recording of these properties were limited, the freestream density was averaged over the entire day for which the measurement took place.

Experimental set-up

The experimental set-up features the DU96 airfoil mounted to a structure mounted directly on top of the contraction, which is the same mounting set-up used in Zhang et al. [78]. The set-up consists of two sidewalls spaced 400mm apart, such that they are flush with the contraction exit. Each of these sidewalls has a circular hole cut out in the middle allowing for two circular, plexiglass panels that are mounted to a rotating metal bracket, between which the airfoil is mounted. On one side, the metal bracket is connected with a servomotor which allows the user to set the airfoil at any desired angle of attack. Its accuracy was verified with an inclinometer. The attached panel was covered with vinyl material to allow for a uniform, dark background for the PIV field of view. The panel on the other side is unobstructed to provide optical access for the PIV camera. A schematic and photo of this setup are shown in Figure 5.4 and Figure 5.5

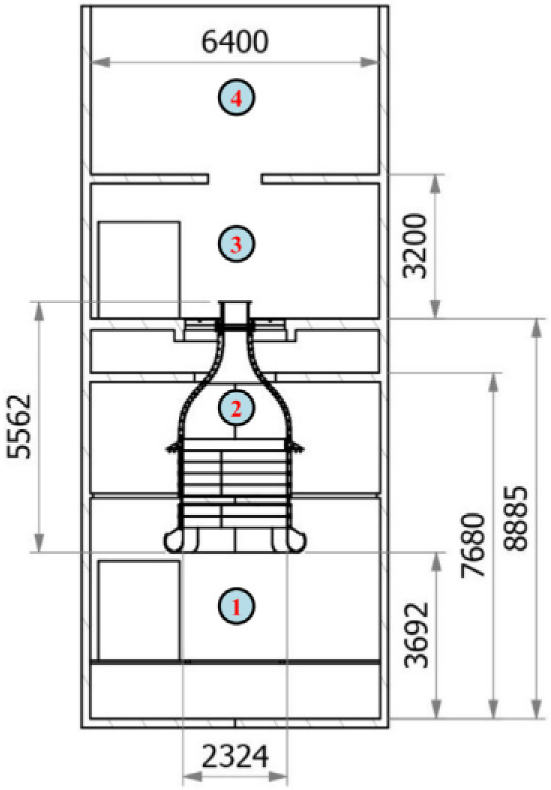

Figure 5.3: Schematic of the A-tunnel, the tunnel used in the present experiment. Numbers indicate 1) The settling chamber, 2) Contraction part, 3) Anechoic plenum, 4) Top floor with fans and collectors [80]

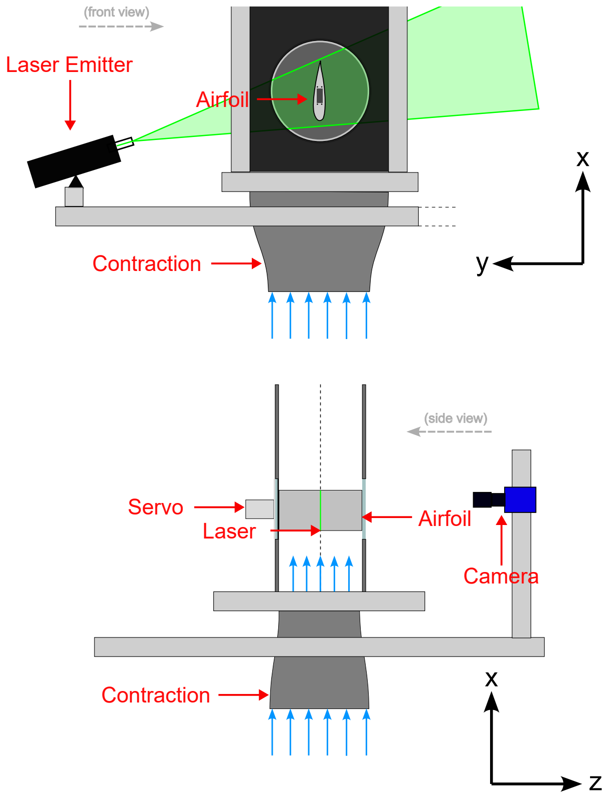

Figure 5.4: Schematic of the side view (top) and front view (bottom) of the experimental set-up. The grey arrows indicate the view direction of the opposing figure

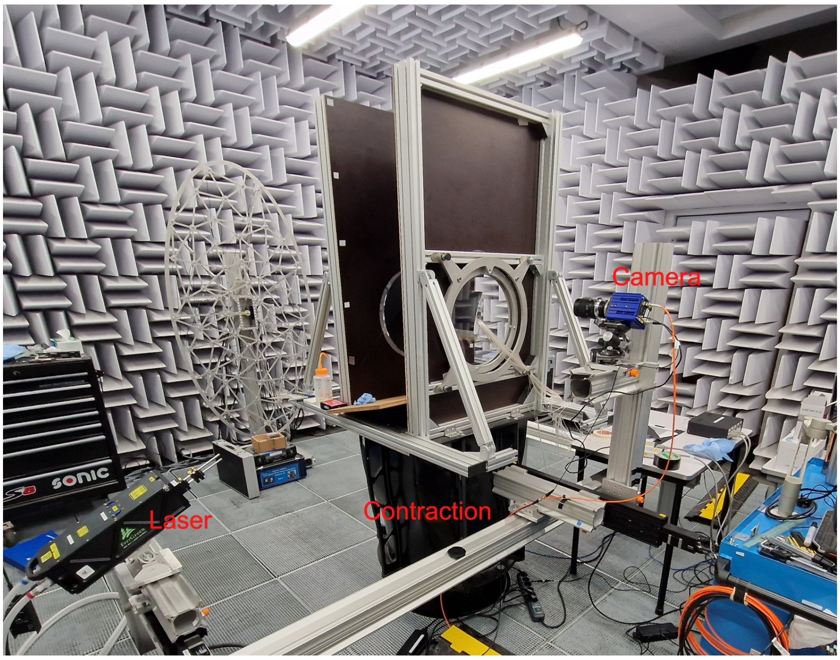

Figure 5.5: Photo of the experimental set-up

Laser set-up

The laser used for the PIV set-up is an EverGreen2 Double-Pulse Nd:YAG laser[1]. This laser is capable of sending double pulses of 70-200 mJ with a wavelength of 532nm. The laser was mounted at a distance from the wing, in line with the centreline of the 2D wing, slightly lower than the airfoil itself (see x-y plane of Figure 5.4). By shining the laser through lenses, the single beam can be turned into a planar laser that illuminates the entire FOV of the PIV camera, encapsulating the centre plane of the 2D wing. The laser beam is shone through two spherical lenses to expand and subsequently focus the laser beam onto a final cylindrical lens, to expand it into a planar beam. Normally, the thickness of the laser sheet needs special attention due to particles moving out of the illuminated region when non-zero out-of-plane velocities are present. However, in this research, 2D flow is assumed, so the thickness of the laser sheet is less significant. This set-up and the planar laser beam is highlighted in the front view of Figure 5.4.

Camera set-up

The camera that was used is a LaVision Imager sCMOS CLHS[2], which is a high-speed camera specifically intended for PIV applications. The CLHS version is connected to the acquisition PC using optic cables. The camera is able to shoot image pairs with an interval of down to 0.2μs at a resolution of 2560x2160 at 50fps. The camera is mounted on a stiff frame outside the optical access panel, pointing as orthogonally as possible onto the centre-plane of the 2D wing. With a 60mm lense, the field of view was adjusted to cover roughly the aft 60% of the chord, as well as roughly 30% of the chord into the aft flow field, capturing at least 50mm above the airfoil surface for all angles of attack. The results is an FOV of roughly 190x90mm,

Particle seeding

For the particle seeding, a SAFEX fog generator was used which creates water-glycol droplets of roughly 1 μm thickness. This generator was deployed in the top floor of the wind tunnel, just before the fans (section 4 in Figure 5.3). The closed-circuit nature of the wind tunnel means that the fog will fill up the entire tunnel when given a continuous seeding input. The seeding was manually adjusted based on perceived seeding density in the PIV images throughout the entire test.

---

[1] `https://www.quantel-laser.com/en/products/item/evergreen-70-200-mj-.html`

[2] `https://www.lavision.de/en/products/cameras/cameras-for-piv/`

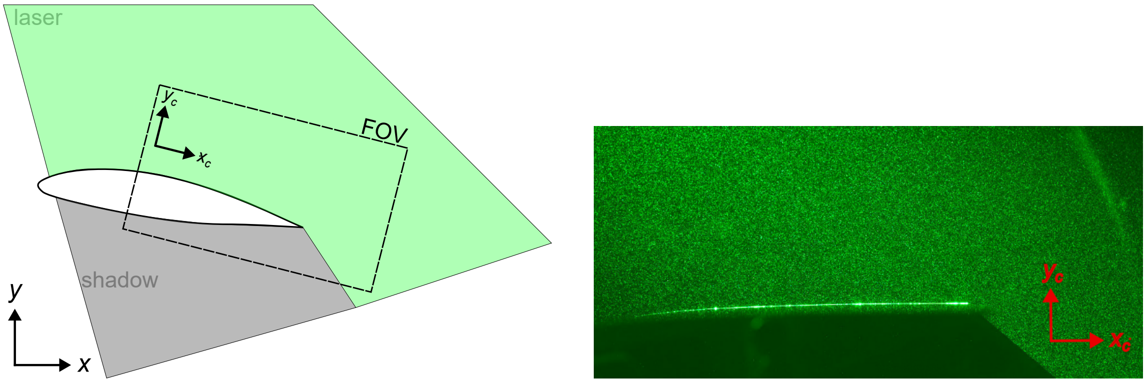

(a) Schematic **(b)** Camera shot

Figure 5.6: Field of view of the PIV camera

PIV & Recording Set-up

Turbulent separation is a drastic flow regime on the upper surface of the airfoil, which requires whole-field measurements in order to fully capture its characteristics. Particle Image Velocimetry (PIV) is a quantitative method that allows for quantitative measurements of the desired flow field. In the present research, as mentioned, PIV will be used to measure the properties of the separation region.

PIV works by capturing an image pair of seed particles that follow the streamlines of the fluid, and capturing images illuminated by a strong light source, such as a high power laser. In this case, a 2D flow is assumed, so as apparent from the previous section, a planar PIV was used, which measures $[u, v] = f(x, y)$.

Since the focus of this research is primarily on statistical results rather than time-resolved analyses, the image rate is not required to be high, and was set at 15Hz, meaning that 15 image pairs are collected per second. On an FOV of roughly 191x89mm spatial resolution of the set-up is 13.15 px/mm, and with a sensor pixel size of 6.5µm, this corresponds to a magnification factor of 11.7. The optimal displacement of a particle for PIV cross-correlation is a quarter of the interrogation window [81]. For a 12x12 minimum interrogation window size, this corresponds to a displacement of 3 pixels, or 0.23mm. Since the velocities inside the separation region, which is of the most interest, varies roughly between $-0.2U_\infty$ to $1.0U_\infty$ (see Figure 2.13a), a higher freestream displacement was chosen. The frame separation was thus chosen per velocity to result in roughly 10 pixel, or 0.75mm freestream displacement. The frame separation values that were used can be found in Table 5.2. To achieve statistical convergence, an ensemble size of 1000 frames was chosen. A summary of the these settings can be found in Table 5.2.

Property	**value**	**unit**
Method	2D planar	
Recording rate	15	Hz
Focal length	60	mm
Aperture - $f_\#$	5.6	-
Field of View	191x89	mm
Spatial resolution	13.15	px/mm
Magnification factor	11.7	-
Interrogation window size	12x12	px
Freestream displacement	10	px
Number of samples	1000	

Table 5.1: PIV settings

Tunnel correction

Several relevant corrections were discussed in section 2.10. Given the fact that this experiment takes place in a wind tunnel set-up rather than a true freestream, some of these corrections need to be

U_∞ $[m/s]$	10	15	20	25	30
Δt $[\mu s]$	70	50	40	30	20

Table 5.2: Frame separation settings for various tunnel velocity settings

considered. However, note that the focus of the results lies on comparison of the flow measurements with and without kirigami, rather than the actual quantity of the measurements. A brief discussion will follow on the relevance of these corrections and whether they are required for an accurate comparison. The blockage-related corrections mainly focus on correcting drag on the model. The reduced drag from the wind tunnel, as shown in the literature review, originates from reduced flow velocity at the model. These are either a function of the area ratio between the model and the tunnel outlet, or the drag on the airfoil directly. Since the kirigami height is extremely small compared to the tunnel, it is not expected to influence the area ratio, and therefore, the velocity at the model will be the same across different kirigami configurations. If kirigami increases or decreases the separation, this could have consequences for the drag due to wake blockage. This in turn causes an error between the measured drag and the actual drag. However, since only the difference between kirigami configurations is of interest, and the drag error moves in the same direction, the only effect this will have on the result is that the measured drag difference between the clean configuration and the kirigami configuration, is an underestimation of actual difference in a freestream. The change in drag across configurations can therefore be assessed without correction. Furthermore, the drag is not measured directly, only the wake deficit. Blockage corrections are therefore omitted in the present research.

The lift interference results in an error between the geometric and the effective angle of attack. Since these map one to one, the comparison between cases remains intact for constant α_{geom}. In past research, using the same experimental set-up, a correction factor was determined. The correction factor ξ, which is calculated as shown in Equation 5.1, which for this airfoil was determined to be 1.294 [78]. Note that this research did not focus on separated flows, so care should be taken when using this correction factor method.

$$\xi = \frac{\alpha_{geom}}{\alpha_{eff}} = \frac{C_{l_\alpha,sim}}{C_{l_\alpha,exp}} \tag{5.1}$$

Since the present experiment does not explicitly focus on the quantitative effect of specific angles of attack, this correction was not applied to any of the present results. Thus, in the rest of this report, α will specifically refer to α_{geom}. However, this correction should be kept in mind for future experiments that aim to reproduce the results in this thesis.

5.3. Post-processing methods

5.3.1. PIV pre-processing

The first step is image calibration, which allows for the definition of a general dimensional coordinate system (in mm) for the acquired raw images (in pixels), and can be used to correct the perspective, correct for image distortion and calibrate the pixel density with dimensional values. This is done using a pinhole calibration model placed parallel to, and as close as possible to the centreline of the airfoil.

Before applying cross-correlation analysis, the raw images require some pre-processing steps to reduce errors. First, a shift and rotation correction is applied to each image set by ensuring a refence point in the images is kept at a constant location (e.g. the airfoil trailing edge). Then, the minimum over time is subtracted from all image sets, with a weighting factor of 1.2, which removes any reflections. A mask is then applied to remove the airfoil from the field of view. Further error sources include particle image size and shape, as well as variation in the illumination intensity of particles [82]. To mitigate this, the intensity is normalised with a local average to obtain more uniform brightness among particles, and these are smoothed using Gaussian smoothing.

A cross-correlation algorithm was then applied to these image pairs. This comprised a standard, multi-pass, 2D PIV method. The initial interrogation window size starts at 48x48 and goes down to 12x12. No window overlap is used since finer resolutions are not strictly necessary, and using no overlap prevents excessive smoothing of the data. Local outlier detection and removal is also applied.

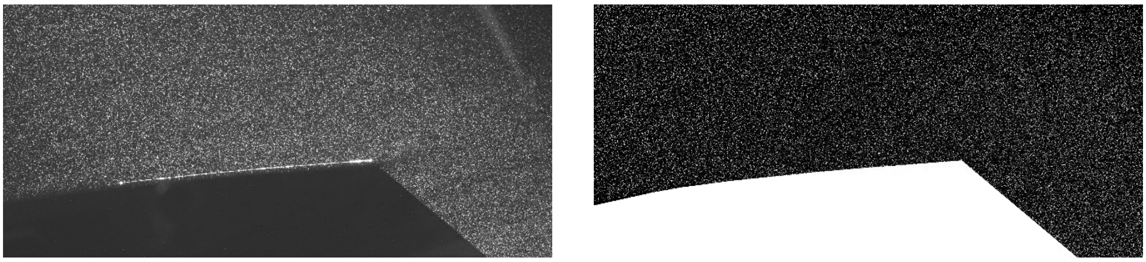

(a) Before **(b)** After

Figure 5.7: Effect of post-processing on the raw image data

5.3.2. Uncertainty quantification method

The aforementioned pre-processing steps help to reduce uncertainty, but uncertainty cannot be fully eliminated. Since PIV reconstructs the velocity field from a displacement field, i.e. $u(x, y) = \Delta x(x, y)/\Delta t$, uncertainty quantification can be applied that aims to find the uncertainty in the displacement field.

This uncertainty can for example, be extracted by analysing the contribution of each particle in an interrogation window, which is known as the particle disparity method. This method works by comparing an interrogation window pair at the optimum window displacement (i.e. by finding the correlation peak). Within this window, pairs of displaced particles are detected, and their disparity is measured. The uncertainty of the correlation window then results from the statistics of the particle disparities in this window[83].

In DaVis, the software used for PIV post-processing, the method used for uncertainty quantification is an extension of the particle disparity method, which is the correlation statistics method. A similar methodology is applied, but instead by matching individual pixels' contribution to the cross correlation, where their individual uncertainty is obtained from the cross correlation peak[84]. This method requires interrogation windows that were obtained using multi-pass PIV with window deformation and predictor-corrector filtering [82]. Both of these methods fall under 'a-posteriori' uncertainty quantification methods [82], as they are applied after cross correlation.

The resulting uncertainty is in the form of a velocity vector for each window that represents a chosen multiple of standard deviations. The uncertainty calculation for this study was set at 1σ. This uncertainty velocity is denoted with the σ subscript e.g. u_σ.

5.3.3. Vector field rotation and dewarping

The perspective correction described in subsection 5.3.1 aligns the coordinate system of the resulting vector fields with the calibration plane, designated at x_c-y_c. Note that, although these vectors have illustrated in line with the FOV for simplicity in this report, this is generally not the case. This reference frame will be rotated to align the x-axis with the tunnel axis. Furthermore, a discrete non-linear transformation will be applied to obtain a surface-bound coordinate system.

The tunnel-aligned rotation is composed of two angles. The first is the angle between the calibration plane and the airfoil chord line (since the camera is not aligned with the tunnel), and the second is the angle between the airfoil chord line and the tunnel. The second angle is simply the geometric angle of attack set by the servo α. The first angle φ can be found by fitting the airfoil curve to the reflection in a raw image that has perspective correction applied to it, and observing what angle the fitted curve was rotated with. These angles are shown in Figure 5.8. The total rotation angle that needs to be applied to the raw vector field is then $\theta = -\alpha - \varphi$. This potentially introduces uncertainties in the form of small deviations between the α setting and the actual angle of the servo.

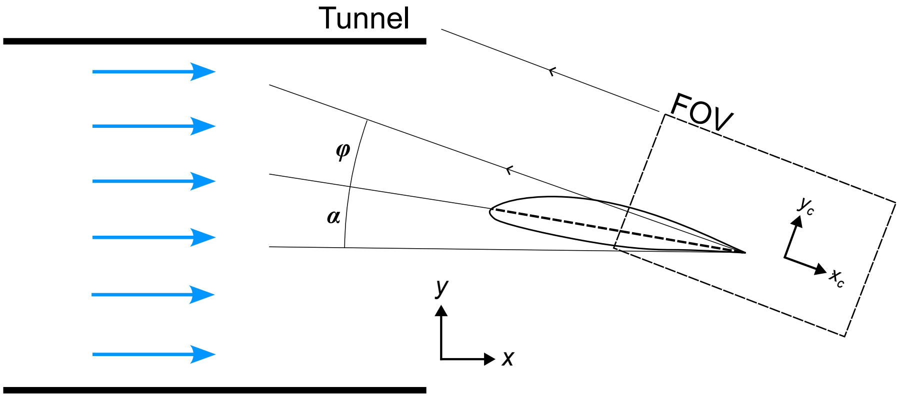

Figure 5.8: Rotation angles from calibration coordinates to tunnel coordinates

Based on this curve fit, a dewarping of the image can be applied to match a wall-attached coordinate system. This allows for easier extraction of the boundary layer profile (i.e. normal to the surface) and a more concrete definition of forward and reverse flow (i.e. parallel to the surface). The first step is to extend the airfoil upper surface curve from the trailing edge, parallel to the airfoil to create a smooth extension, so that the coordinate system spans the entire field. This reference surface is divided into arc length segments with the same resolution as the original grid i.e. $\Delta s = \Delta y$. For each grid-point s_i on the airfoil surface, a wall-normal unit vector **$\bar{\text{n}}$** is generated, along which a new grid is discretised with step sizes Δy. This creates an **s** $-$ **n** coordinate system where **s** is always parallel to the surface below it, and **n** is always normal to the surface below it. **n** is defined such that on the airfoil surface, $n = 0$, and any point above it is the normal distance in mm. **s** is defined such that $s = 0$ at the leading edge, with any non-zero s indicating the arc length of the airfoil from the LE onwards. The old dataset $[u, v]$ is interpolated from the old grid to the new grid points.

Lastly, the velocity field on the new grid $[u, v] = f(s, n)$ needs to be rotated. The angle of rotation is constant for all data points at a constant s. This angle at each constant s_i, called θ_i is equal to the angle between the tangent of the surface at $(s_i, 0)$ and the x-axis of the previous reference frame. The formula for this rotation is as in Equation 5.2. Figure 5.9 shows a diagram of this transformation. Note that this shows the dewarping from an x-y frame that is aligned with the chord, but this need not be the case so long as the reference airfoil surface is correctly aligned in the original x-y frame.

$$\begin{bmatrix} u_s \\ u_n \end{bmatrix} = \begin{bmatrix} cos(\theta_i) & -sin(\theta_i) \\ sin(\theta_i) & cos(\theta_i) \end{bmatrix} \begin{bmatrix} u \\ v \end{bmatrix} \tag{5.2}$$

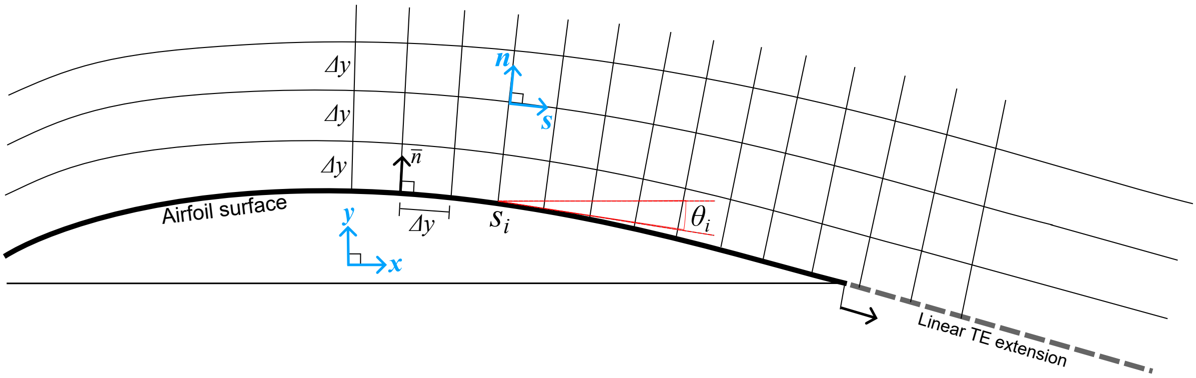

Figure 5.9: Diagram of the discrete surface-bound transformation, showing the dewarped $s - n$ grid over the airfoil surface

The Jacobian of this transformation is not calculated, since the derivatives of the flow field are not used in this report.

5.3.4. Statistics

Based on the 1000 vector fields, time-series statistics can be calculated. Specifically, the mean μ in both directions, the standard deviation σ in both directions, the backflow coefficient γ_{pu} based on the dewarped field and the Reynolds stresses R_{xx}, R_{xy} and R_{yy}. These quantities are calculated for each single data point x_i in vector field i, across all vector fields with $N = 1000$. The resulting output is a single vector field for each component (e.g. the mean generates a mean u field and a mean v field where x_i can take both u_i or v_i as an input). Note that for all of these, i indicates the index along the time series for a single point in the vector field. These operations are applied to all points on the vector field, meaning the result is a new vector field.

The mean is calculated as the arithmetic mean, which, if the size of the dataset N is known, is calculated as in Equation 5.3.

$$\mu = \frac{1}{N}\sum_{i=1}^{N} x_i \tag{5.3}$$

The fluctuations can be characterised by the standard deviation shown in Equation 5.4, which shows a form with and without dependency on the mean.

$$\sigma^2 = \frac{1}{N}\sum_{i=1}^{N}(x_i-\mu)^2 = \sum_{i=1}^{N}\frac{x_i^2}{N} + \left(\sum_{i=1}^{N}\frac{x_i}{N}\right)^2 \tag{5.4}$$

Assuming the thousand images are a representative sample of the time series, the backflow coefficient can be calculated as the number of datapoints that show reverse flow over the total number of datapoints N. The former is calculated by a function that is 1 when $u_{s,i}$ is negative and 0 when positive. Using the sign function, this is mathematically represented by Equation 5.5

$$\gamma_{pu} = \frac{1}{N}\sum_{i=1}^{N}\frac{1-\mathrm{sgn}(u_{s,i})}{2} = \frac{1}{2} - \frac{1}{2N}\sum_{i=1}^{N}\mathrm{sgn}(u_{s,i}) \tag{5.5}$$

Lastly, the Reynolds stresses are derived from the fluctuating term u' of Reynolds averaging process. Using the notation convention mentioned in subsection 2.3.2, the formula for these are show in Equation 5.6. Note that, due to the flow field being assumed as incompressible, in this report, these quantities represents the Reynolds stress over the density i.e. $R'_{ij} = \frac{R_{ij}}{\rho}$.

$$R'_{xx,i} = \overline{u_i'^2} \quad R'_{xy,i} = \overline{u_i'v_i'} \quad R'_{yy,i} = \overline{v_i'^2} \tag{5.6}$$

5.3.5. Boundary layer extraction

From the dewarped mean fields, the boundary layer can be extracted as vertical profiles of u_s velocity. Typically, the boundary layer thickess can be measured by δ_{99} which is the point where the velocity profiles reaches 99% of the boundary layer edge velocity. However, due to the vertical pressure gradient around an airfoil, the value of this edge velocity becomes ambiguous as the flow outside the shear layer is not constant across y. A quantity similar to δ_{99} can be found by finding the value where the shear $\omega_n = \frac{\partial u_s}{\partial n}$ vanishes. The Jacobian is not necessary here, because the contribution of $\frac{\partial u_n}{\partial s}$ to the vorticity is neglected, and the Jacobian for the terms with respect to n are equal to 1 (since $dy = dn$). This point was determined by normalising the profile of ω_n along y by its maximum absolute value for each x-coordinate in a dewarped velocity field, which results in a vorticity field with locally normalised vorticities. A function for finding isolines is then used to find a continuous line in this normalised vorticity field where the vorticy is at a certain threshold. Since finding 0 did not give reliable results, this threshold was set at 4% of the maximum shear. This generates a continuous line indicating the height of the shear layer δ_ω (not to be confused with the vorticity thickness). Although this δ_ω will not necessarily be equal to δ_{99}, these values are still strongly related. Furthermore, the purpose of quantification in this thesis primarily for purposes of comparison, so the actual quantities are less significant.

5.3.6. Drag estimation

The drag can be directly derived from a velocity field based on a control volume analysis on the momentum. Assuming uniform inflow, and a control volume boundary far away enough from the trailing edge of the airfoil (measured as x_{probe}), the drag calculation becomes only a function of the velocity profile at the control volume boundary. The time-averaged drag per unit span is normally given by Equation 5.7 [85] [86], where $u_e(y)$ is the x-component of the velocity profile at the aft control volume boundary (i.e. the wake profile), and a, b are the upper and lower y-bounds of the control volume.

$$\overline{D}' = \rho \int_a^b U_\infty (U_\infty - \overline{u}_e(y))dy \tag{5.7}$$

However, the limited field of view was unable to capture the far-field of the airfoil, or the external streamlines towards the free stream, violating the assumptions of the equation above. As a result, this calculation would not converge to a constant drag value with increasing x_{probe}. More consistent behaviour was found when simply calculating the total amount of momentum per unit span exiting the control volume behind the trailing edge, called Π_{wake}, calculated with Equation 5.8. Since the drag is equal to the difference between momentum inflow and outflow, this serves as an indicator for drag, i.e. higher momentum outflow means lower drag. As mentioned, the purpose of these parameters is comparison, which this method will fulfil. The comparison is valid if a and b are kept constant, across comparisons which is the case for a constant $(x/c)_{probe}$ and constant FoV.

$$\Pi_{wake} = \rho \int_a^b \overline{u}_e(y)^2 dy \tag{5.8}$$

5.4. Baseline measurements

This section will give an concise overview of the airfoil separation characteristics based on PIV and pressure measurements.

5.4.1. Characteristics of the flow field

Flow separation can be observed in various levels in the flowfield. Below are 3 examples at different angles of attack for a single flow velocity to highlight this, at 8, 12 and 18 degrees. Figure 5.10 shows various scalar fields of the region of flow on the aft part of the airfoil, and behind it.

From Figure 5.10b, it can be observed the boundary layer is indeed a turbulent one, due to the strong fluctuations in velocity near the airfoil. At the trailing edge, the boundary layer shows rapid growth into a primitive of separation, although neither Figure 5.10c nor Figure 5.10d show any signs of separation. This absence of separation is consistent with the pressure measurements.

Figure 5.11, on the other hand, shows more signficiant evidence of separation. All figures show the rapid boundary layer growth when separation sets in. Figure 5.11c and d show the clear presence of separation, in both the flow reversal near the surface starting from roughly $x/c = 0.6$, as well as the significant respective downward flow at the aft side of the separation region. Figure 5.11b shows, in line with the findings of Simpson [41] (see Figure 2.14), that the separation region both aggravates the velocity fluctuations as well as raises them away from the surface, leaving a weakly fluctuating recirculation region underneath.

Lastly, Figure 5.12 shows similar results to 12 degrees, but the airfoil is now in full separation. The reverse flow region extends almost beyond the FoV, spanning almost the entire aft part of the airfoil. Figure 5.12b shows how the fluctuations are carried far from the surface, over the separation region, as well as the subsequent breakdown of the wake into turbulence in the far-field.

The kirigami height was measured to be 1.4mm, meaning that any flow phenomena around the kirigami are most likely not observable. As such, the question whether these function as a vortex generator are hard to answer based on the flow near the kirigami alone.

5.4.2. Pressure

The pressure distributions for the airfoil is shown below, in Figure 5.13. The pressure distribution consists of a sharp suction peak at the leading edge, with a subsequent sharp drop and a secondary

minimum shortly after, which then recovers through another adverse pressure gradient toward the trailing edge. This is also consistent with both the simulated and measured the pressure distribution shown in Suryadi & Herr [79] (see Figure 5.2), which also uses a DU96 with boundary layer tripping.
At the trailing edge of the airfoil, the onset of separation can be clearly observed, through the stagnation of the pressure gradient without achieving full recovery, which is highly characteristic of trailing edge separation. From 6 to 10 degrees, the pressure appears to fully recover to freestream with no indication of trailing edge separation. For the lowest Reynolds number at 6^o however, a slight drop in pressure is seen in the middle of the pressure gradient. This could be indicative of a laminar separation bubble, meaning that the flow has not fully transitioned at the leading edge at this Reynolds number. This pressure change disappears for the higher Reynolds numbers. At 12 degrees, the onset of trailing edge separation suddenly appears, with a ZPG starting at around $x/c = 0.6$. This gradually progresses to $x/c = 0.4$ at 20 degrees.
For lower angles of attack, the pressure has a strong overlap between all Reynolds numbers. For the higher angles of attack, some difference is observed between different Reynolds numbers. At 18 and 20 degrees, steeper pressure gradients are found for higher Reynolds numbers resulting in a slightly earlier onset of the ZPG region.
Furthermore, the steeper part of the gradient resides on top of the kirigami for the low angles of attack. At 12 and 14 degrees, the kirigami aligns with the onset of the ZPG region. The kirigami is fully in the separated ZPG region for 16 degrees and onward.

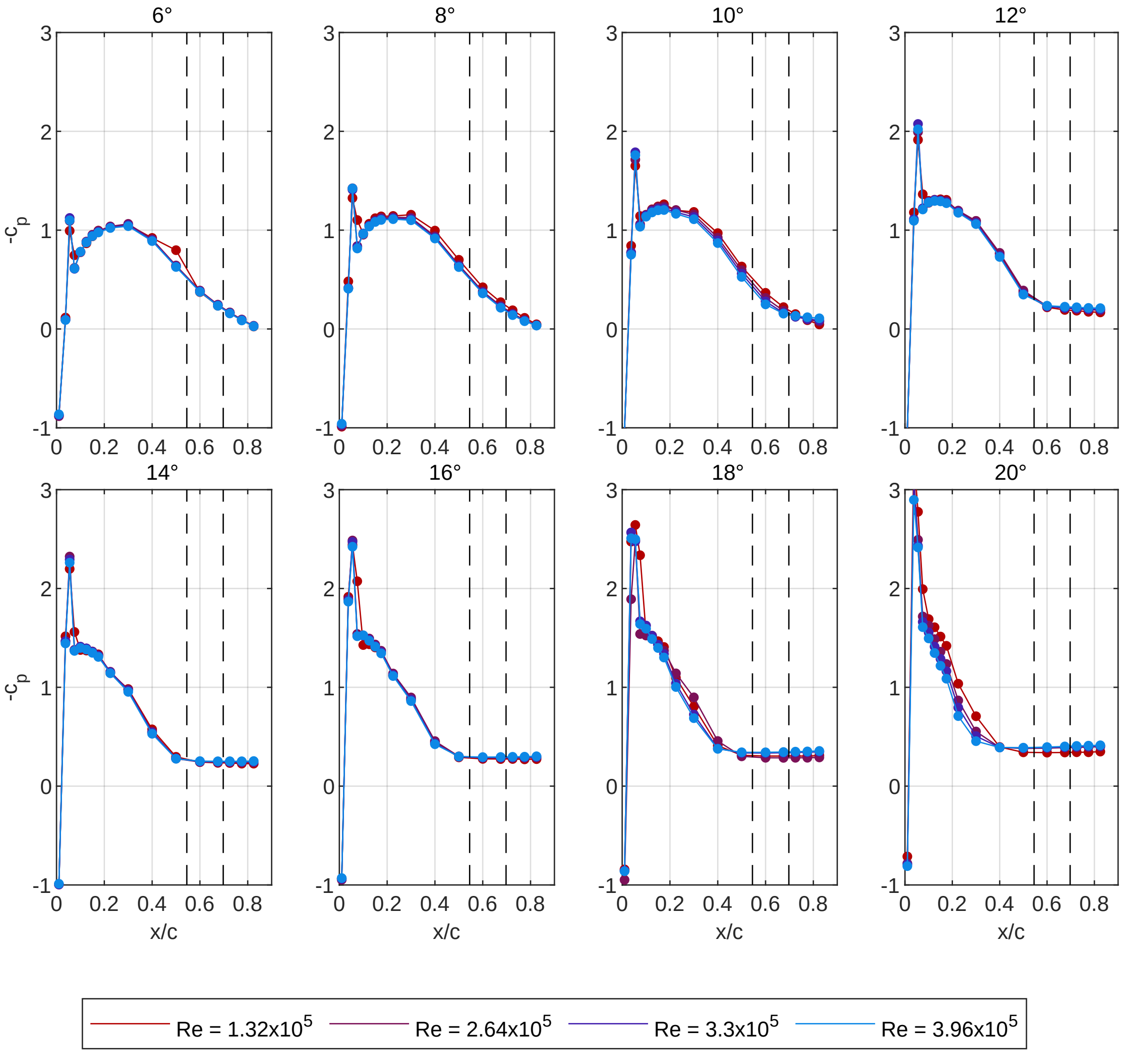

Figure 5.13: Airfoil suction side pressure distribution for angles of attack from 6^o to 20^o without kirigami. Dashed lines indicate the start and endpoint of where the kirigami device would be placed on the surface

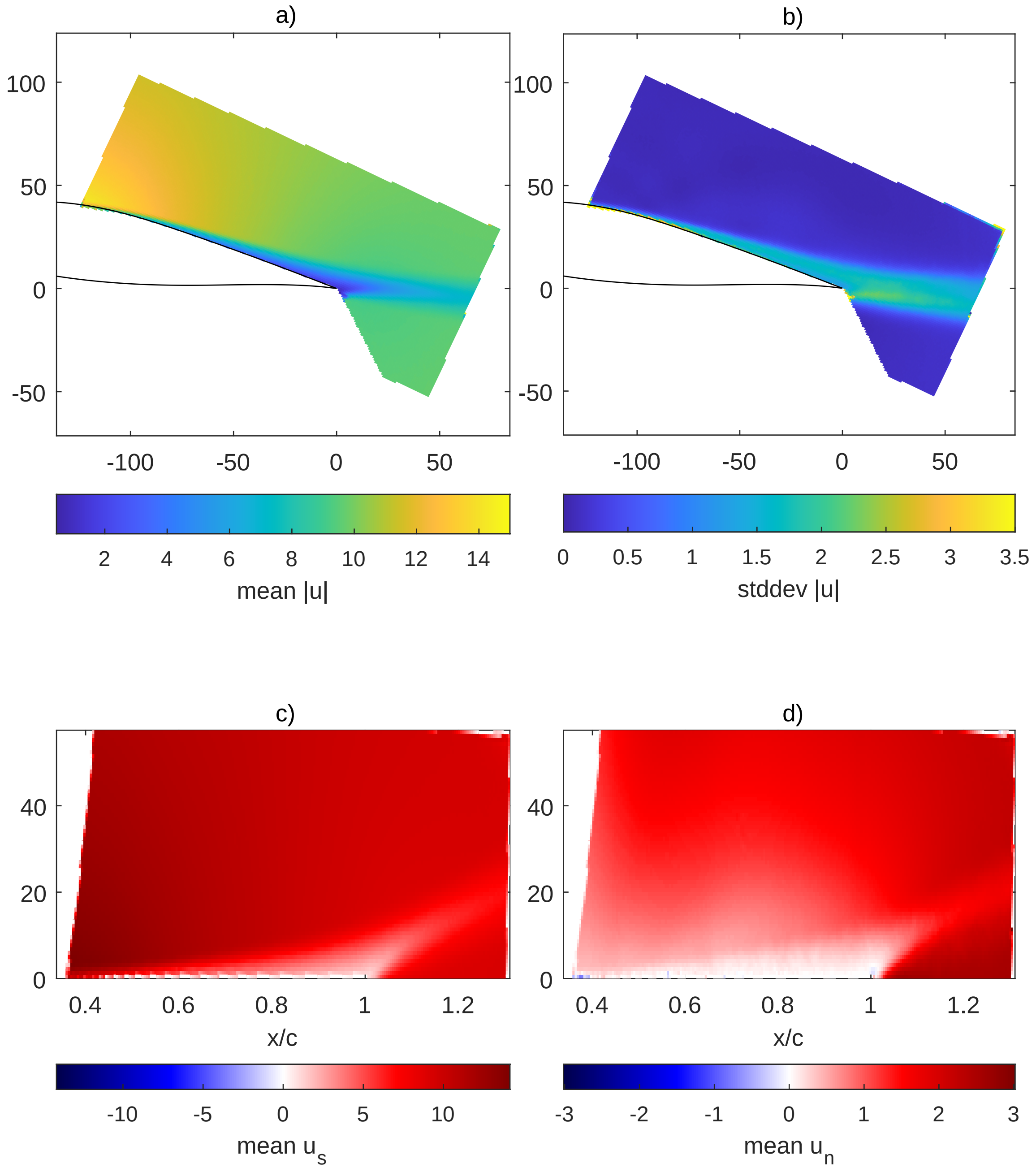

Figure 5.10: Contour fields of the DU96 airfoil at $\alpha = 8^o$, $Re = 1.32 \times 10^5$, showing a) $|\overline{u}|$ mean, b) $|\overline{u}|$ standard deviation c) u_s (x in dewarped space) and d) u_n (y in dewarped space)

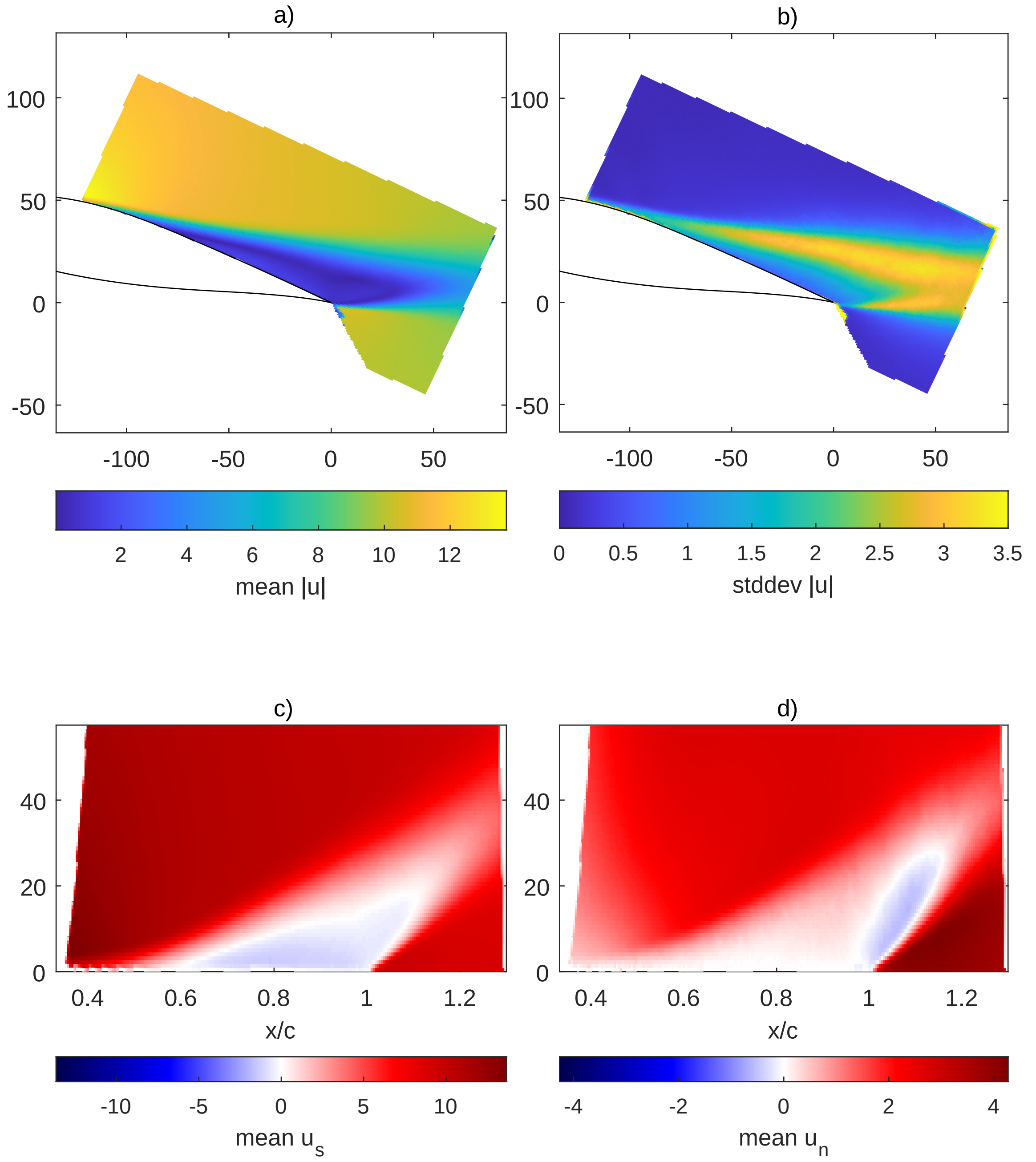

Figure 5.11: Contour fields of the DU96 airfoil at $\alpha = 12^o$, $Re = 1.32 \times 10^5$, showing a) $|\overline{u}|$ mean, b) $|\overline{u}|$ standard deviation c) u_s mean and d) u_n mean

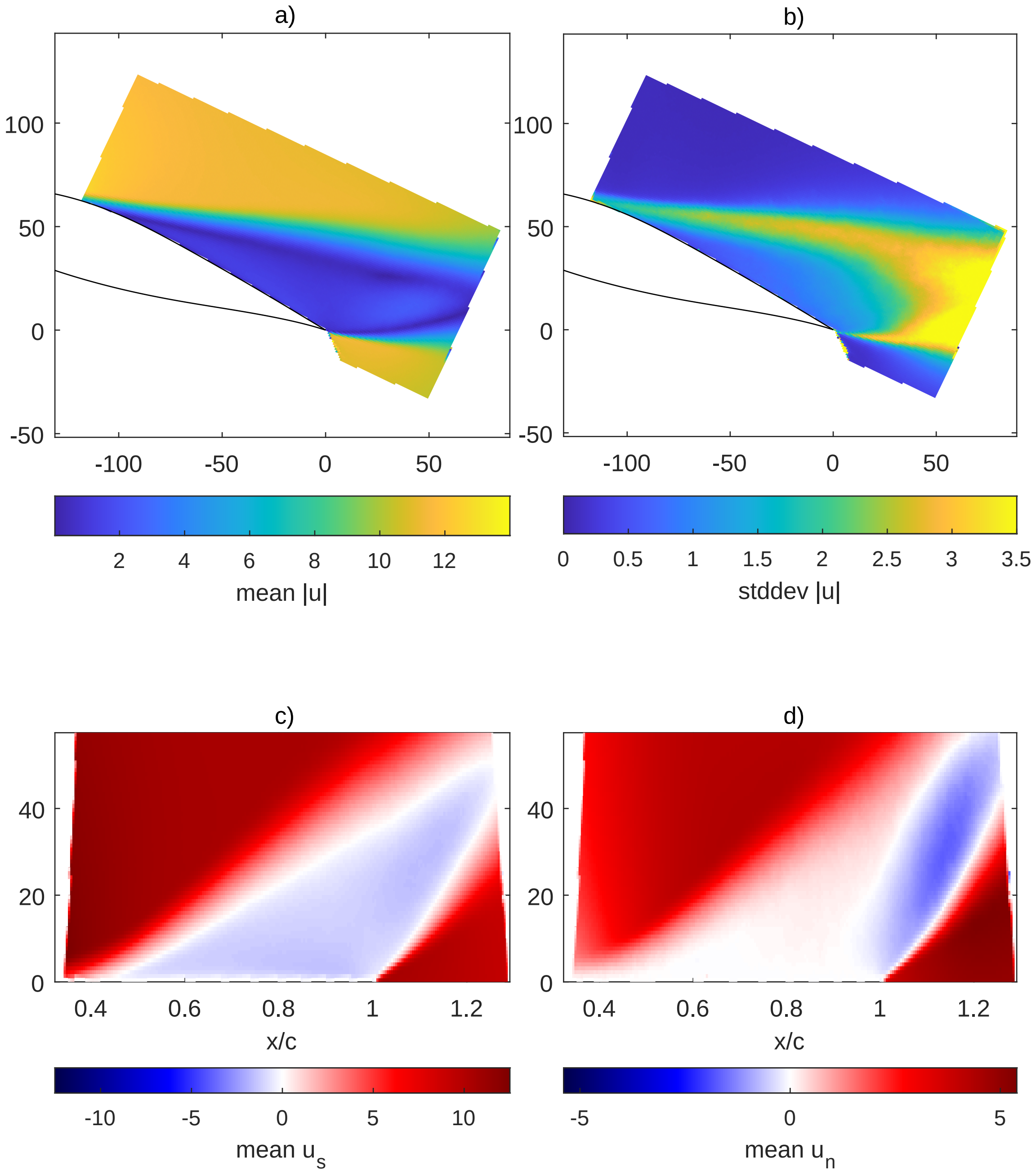

Figure 5.12: Contour fields of the DU96 airfoil at $\alpha = 18^o$, $Re = 1.32 \times 10^5$, showing a) $|\overline{u}|$ mean, b) $|\overline{u}|$ standard deviation c) u_s mean and d) u_n mean

5.4.3. Scaling parameters

To encapsulate a reasonable parameter space, the angle of attack and tunnel velocity were varied. In turn, this both changes the pressure gradient (see previous section), the Reynolds number (and therefore the boundary layer thickness), and the separation point. Clarifying what conditions the kirigami is operating in will aid in determining the effect of the kirigami on the flow. Since flow control devices are typically characterised with respect to baseline parameters, here too, the characterisation will be done with respect to the clean airfoil flow measurements.

Through laser scans, it was known that the centreline height of the kirigami on the airfoil surface is, on average, 1.4mm. With this, the h/δ of the device can be determined. The δ used here is the clean shear layer thickness (see subsection 5.3.5) measured at the end of the kirigami device. This is plotted for each angle of attack in Figure 5.14.

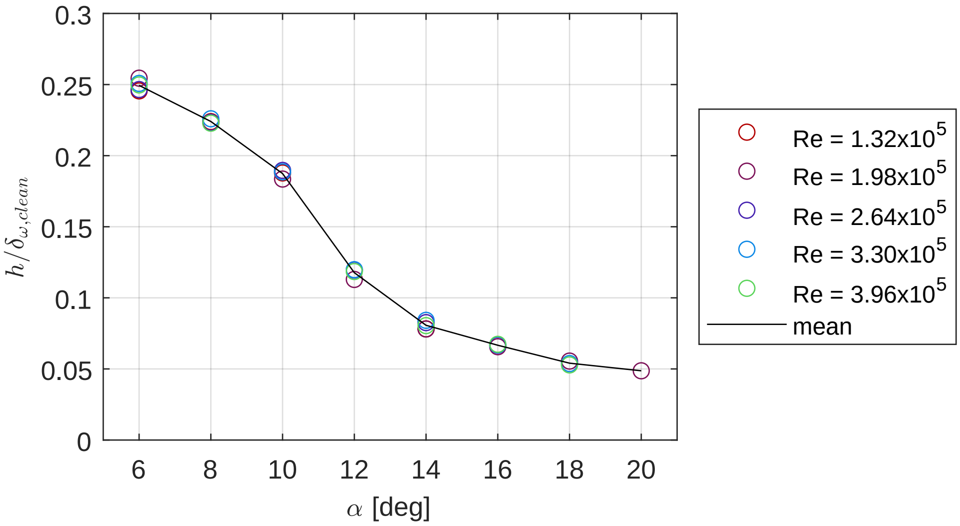

Figure 5.14: Relative kirigami device height measured at $x/c = 0.6$ with $h \approx 1.4mm$

The range of h/δ evidently varies between 0.05 to 0.25. The size of the shear layer naturally increases for higher angles of attack, as the onset of separation, and separation itself results in rapid boundary layer growth [40]. It appears that the kirigami device operates in the height scale range of sub-scale vortex generators for 6 to 12 degrees, which is between $h/\delta = 0.1 - 0.3$ [8].

However, the variation with Reynolds number is practically non-existent, which means the experimental conditions only significantly varied with angle of attack, which effectively captures a smaller parameter space. The thickness of a turbulent boundary layer typically grows with $\delta \sim Re^{-\frac{1}{5}}$ [33]. With the limitations of the tunnel used ($U_\infty = 10 - 30\ m/s$), the Reynolds number could not be varied enough to obtain a sufficient range of boundary layer thicknesses, as this scaling relation would result in a thickness variation of approximately 25%.

It is noteworthy that the boundary layer thickness could not be accurately determined for all cases, resulting in some outliers. As a result, only a few results are available for 16 to 20 degrees. At these angles of attack, the separation region is so large that the edge of the shear layer moves outside the top edge of the FOV, meaning the actual location of the edge cannot be determined.

The separaration point is determined at the point of transitory detachment 2mm above the surface (similar methodology as Simpson [41]). This plot against angle of attack can be found for various Reynolds numbers in Figure 5.15.

It appears that for 6 and 8 degrees, no separation occurs. At 10 degrees, separation rapidly grows, and slowly stagnates after 12 degrees. The separation point is in closest proximity to the kirigami device at 12 degrees, followed by 14 and 16 degrees. This also matches the locations at which the pressure gradient flattens off.

Due to the size of the separation region, being too small at 10 degrees, the lack of PIV resolution results in large variation in the separation point across Reynolds numbers. Furthermore, at 18 degrees and 20 degrees, the separation point moves too far upstream across the edge of the FoV, which also results in

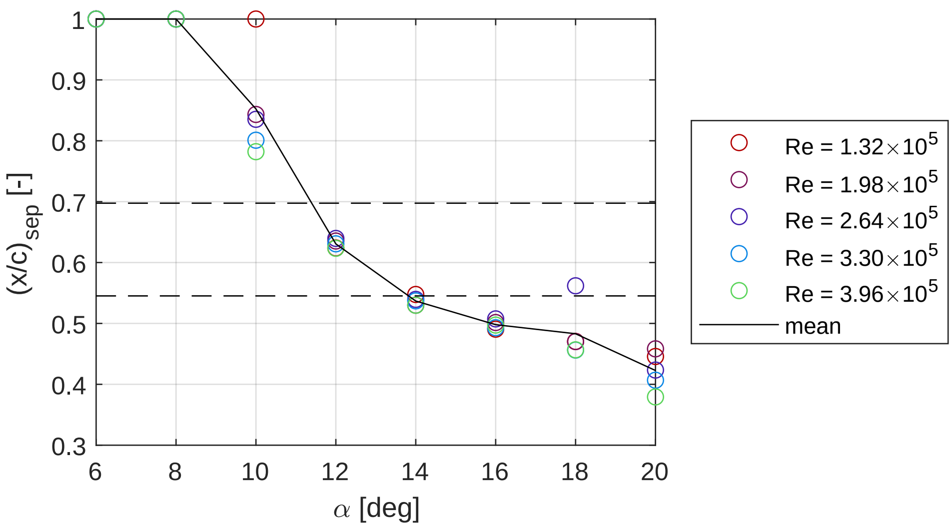

Figure 5.15: Transitory detachment point on the clean airfoil surface with angle of attack. Dashed lines indicate kirigami bounds

outliers in that region. Some of the most extreme, unphysical outliers were removed from the plot. With that said, in line with the invariance over Reynolds number of the boundary layer thickness, the clean surface separation point also shows a limited degree of the same variation across 12 to 16 degrees. The behaviour of the separation on the DU96 is characteristic of that of trailing edge separation, proving its worth as a testing platform for trailing-edge separation control. The next section will show how the kirigami has affected the separation characteristics.

5.5. Separation control effectiveness

In this section, the effect of the presence of kirigami on the airfoil surface is characterised, both through measurement of some characteristic parameters, as well as a closer analysis of the separation region for cases of interest. The kirigami on the airfoil was tested under a wide range of conditions, varying in angle of attack and flow velocity. An overview will follow that quantifies various properties of the separation region, with the goal to investigate how these conditions affect the separation of the airfoil with and without kirigami.

To characterise the separation region, several parameters are used to identify the size of the shear layer, of the reverse flow region and of the reverse flow intensity. All are expected to grow with more intense separation. The first two parameters are the height of the shear layer edge δ_w above the surface (i.e. in the direction of n in the wall-attached coordinate system), and the height of the detachment line (i.e. the isoline where the backflow coefficient $\gamma_{pu} = 0.5$). These are measured at the centre of the separation region, which is defined as half-way in between the separation point ($\gamma_{pu} = 0.5$) and the trailing edge. Furthermore, the reverse flow intensity here is measured as the maximum reverse flow magnitude, and is zero otherwise to indicate the absence of separation. A comparison of the separation points have also been included. The cases at 20 degrees angle of attack have been excluded, as the size of the separation region extended far beyond the field, making it difficult to determine various properties. Moreover, its relative results with and without kirigami are expected to be similar to that of 18 degrees, considering the kirigami is fully immersed into the separated flow.

5.5.1. Separation region size

Figure 5.16 shows both the shear layer height and separation line height at the chordwise mid-point of the separation region for a single Reynolds number to study as an example.

Three regimes of angle of attack can be distinguished from these findings: low, medium and high.

The separation region and shear layer are aggravated by the kirigami for low angles of attack. (6 to 10). Since 6 and 8 do not show any form of separation before this, the kirgami has directly instigated separation. This is in line with the literature findings of kirigami flow control, where kirigami increases

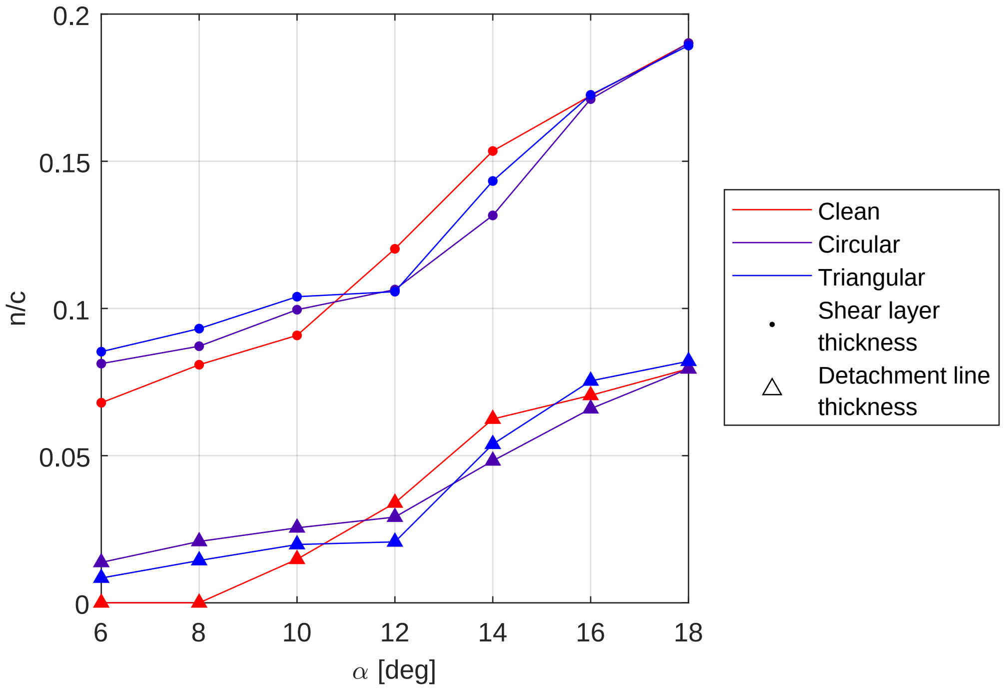

Figure 5.16: Height of the shear layer and separation region measured half-way inside the separation region at $Re = 1.98 \times 10^5$

separation and the size of the wake [22].

For 12 degrees and 14 degrees, however, a noticeable reduction is observed in the size of the separation region and the shear layer for both forms of kirigami. Triangular kirigami appears more effective in inhibiting the separation region at 12 degrees, whereas circular shows the biggest reduction at 14 degrees, for both the separation region as well as the shear layer. It appears that the height scale of the kirigami at $\frac{h}{\delta} \approx 0.08$ to 0.12 is enough to affect the separation region in a favourable way.

At 16 degrees ($\frac{h}{\delta} \approx 0.07$), these differences reduce as it approaches the high angle of attack regime. However, it still has an effect, with a slight reduction in the height of the separation region for circular kirigami. This is the height scale that matches the scale in roughness literature where adverse effects on separation were measured [69]. In the present research, the effects at this height are either favourable or unchanging, indicating that the kirigami is not functioning as a conventional roughness at these height scales.

For high angles of attack (beyond 18), the differences observed in the shear layer is completely diminished, which indicates that the scale of the kirigami is simply too small to influence the separation region at $\frac{h}{\delta} \approx 0.05$.

5.5.2. Flow reversal

The reduction in separation is also exemplified in the intensity of the reverse flow for the same reynolds number, shown in Figure 5.17.

The reverse flow is significantly reduced at 12 and 14 degrees for both triangular and circular kirigami. At this Reynolds number, they appear to be of similar effectivity. The maximum reduction is observed for circular kirigami at 14 degrees, which amounts to a 25% reduction in reverse flow velocity. This general separation control efficacy of the kirigami at these angles of attack could be attributed to enhanced mixing in the form of momentum being transported towards the wall due to the kirigami working as vortex generators. Further analysis will point out whether this is the the exact working principle of the kirigami.

Consistent with the previous findings, the separation is also strongly aggravated at low angles of attack (8 to 10), with an extremely large relative reverse flow measured at these angles of attack. This might indicate that the kirigami causes a momentum deficit leading to flow reversal, which matches the

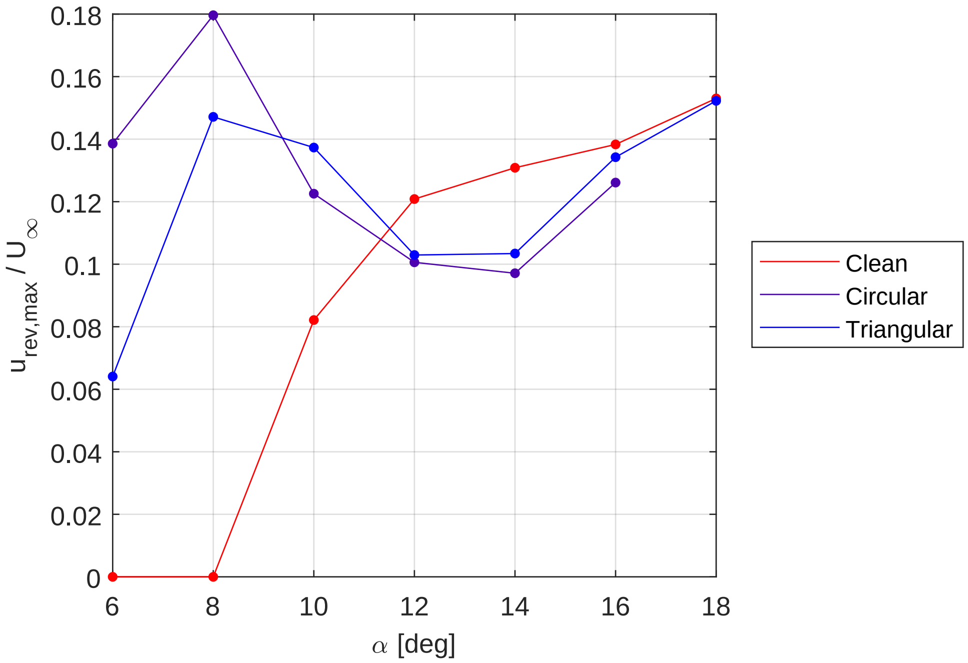

Figure 5.17: Maximum reverse flow magnitude in the separation region at $Re = 1.98 \times 10^5$

behaviour of roughness in turbulent separation [69] (see section 2.7).

5.5.3. Effect on drag

The reduction in flow reversal is indicative of reduced drag, but in order to properly quantify whether this is the case, one needs to look at the momentum change in the wake, which is determined as described in subsection 5.3.6.

Owing to the reduction in flow reversal, the drag has been substantially reduced for 12 and 14 degrees. For 14 degrees, the circular kirigami has resulted in roughly 7% more momentum outflow in the wake. This result is expected considering the significant reduction in reverse flow that was found for these angles of attack in Figure 5.17. These findings are consistent with those in the previous sections, which established separation was reduced for these cases. The reduction in both the size of the separation region and the intensity of the reverse flow are indicators of a reduced momentum deficit downstream, which in turn indicates a reduction in drag.

5.5.4. Detachment point

This section shows the change in separation point when kirigami is applied for a specific Reynolds number, building upon the clean measurements in Figure 5.15.

Consistent with the findings in separation region size, at low angles of attack, the detachment point moves forward significantly under the influence of kirigami. From this low angle of attack onward, the detachment point moves much more gradually upstream than the clean case as angle of attack is increased. The circular kirigami has a much more prounced effect at these low angles than the triangular kirigami. At 12 and 14 degrees, where separation reduction was observed in other metrics, the separation point expectedly moves aft of the clean case. At 12 degrees, the triangular case is more effective in doing so, despite the circular also showing reduced separation in previous data. This effect reverses for 14 degrees.

It appears there is some tendency towards separation reduction if the clean separation point is located either within the kirigami or just upstream of it. The kirigami also seems unaffected when the separation point is further upstream. Only at a point just near the starting edge does the kirigami delay separation. This shows that it is less likely that the kirigami functions as vortex generators, since mixing happens aft of a VG, and therefore the separation could only be controlled if the separation point was located behind the kirigami. The fact that kirigami aggravates separation only if the separation point is behind

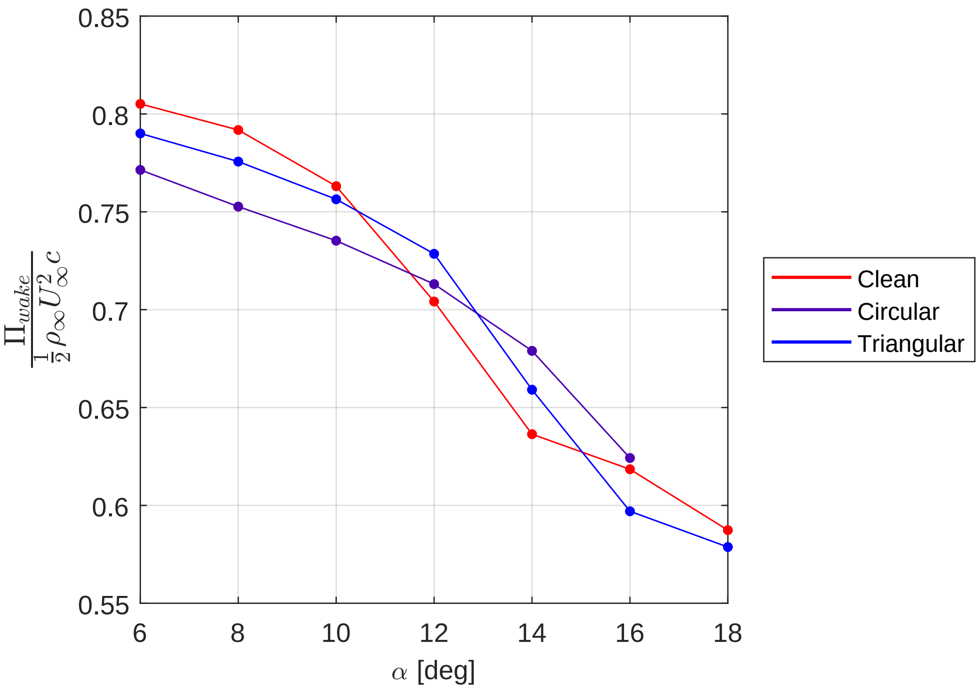

Figure 5.18: Momentum outflow at the wake boundary at $Re = 1.98 \times 10^5$

it reinforces the hypothesis that kirigami causes a momentum deficit at this large of an h/δ.

Instead, considering that separation seems to only be reduced when the separation point is just ahead of the kirigami could signify that the kirigami functions as a 'hump' in the flow. If the kirigami causes enough blockage for the flow, the streamlines would need to curve over the top, similar to a solid hump. Consider the example of a Gaussian bump. Experimental and numerical pressure data of such a surface geometry from literature is shown in Figure 5.20 [87]. After a gentle pressure rise upstream of the bump due to the upward curvature of the streamlines, a strongly favourable pressure gradient exists on the front part of the bump in anticipation of the suction peak. Since separation is driven by a combination of wall shear stress and an adverse pressure gradient, this suction peak may briefly override the adverse pressure gradient and delay an early onset of separation. With sufficient blockage of the kirigami, a similar effect could happen just upstream, as shown in Figure 5.21. The proposed mechanism is that the kirigami creates an equivalent displacement body that functions as a hump, leading to convex streamline curvature and a favourable pressure gradient at the leading edge of the kirigami device. The subsequent strong adverse pressure gradient downstream of that that would also then contribute to earlier separation if the separation point were further downstream of the kirigami.

This effect would also explain the difference between the circular and triangular kirigami. Figure 4.1 shows that the circular shape has a larger area than the undeployed triangular shape, resulting in more frontal area when deployed and thus more blockage for the circular device than the triangular one, and as a result, a larger pressure gradient. This would also explain the increased effect that circular kirigami has on the separation at low angles of attack (if the kirigami were functioning as a roughness), with a larger area indicating a larger momentum deficit. The shape of the kirigami will also influence the wake that is shed off each element, but more detailed studies are required to determine the properties of these, as well as their exact effects.

A local favourable pressure gradient might explain why separation control occurs for a detachment point upstream of the kirigami, but this same theory would imply an amplified adverse pressure gradient over the rest of the kirigami geometry. This, in turn, fails to explain the reduction of separation for a more aft detachment point. An explanation for the latter effect could emerge from studying the flow directly around the kirigami. This is where the 'roller-bearing' effect mentioned by Howard & Goodman [72] could come in, reducing shear stress and delaying separation. This effect is also illustrated in Figure 5.21. The kirigami elements are thin, hollow surfaces, meaning they are likely to generate a wake

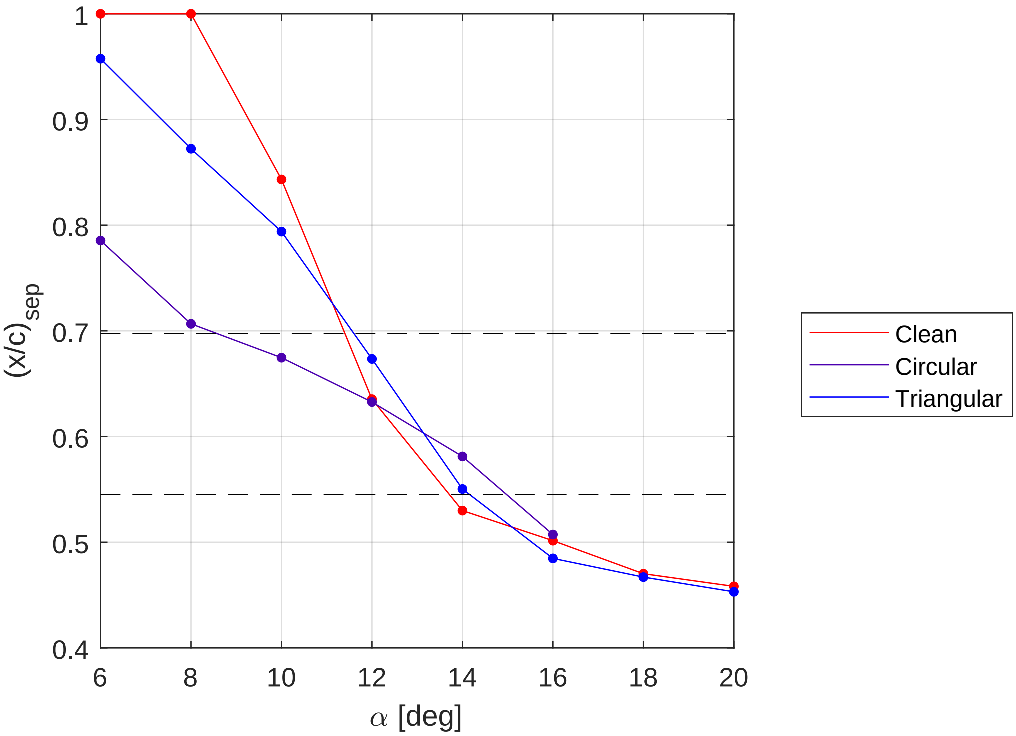

Figure 5.19: Transitory detachment point measured 2mm above the surface at $Re = 1.98 \times 10^5$

with recirculation as demonstrated in the image, which is similar to the effect of spanwise grooves. The proposed mechanism, as Howard & Goodman discusses, is that the grooves ”obviate the usual no-slip, boundary condition” [72], through the exchange of larger separation regions with smaller ones. This means the flow velocity of the displacement body in Figure 5.21 has a non-zero velocity due to the recirculation, rather than a zero-slip boundary condition, which alleviates shear stresses at this boundary. Since these are one of the driving forces for separation, this should lead to a delay in separation. Further analysis should point out whether this is the actual working mechanism of kirigami. However, with the current size of interrogation window being around 0.91mm/window, and a kirigami height of 1.4mm, the PIV resolution in the present research is insufficient to make any judgments on this.

5.5.5. Variation with Reynolds numbers

The kirigami was measured at four other Reynolds numbers. For brevity, these plots have been moved to Appendix A. The behaviour of the separation under the influence of kirigami for these Reynolds number varies somewhat, but not in any way that significantly affects the conclusions. For the separation region size, The trend of enhanced size at low angles of attack, and reduced size at medium angles of attack is continued. The reverse flow enhancement for low angles of attack is reduced for lower Reynolds numbers, but significantly increased for higher Reynolds numbers. The reverse flow reduction is more significant at lower Reynolds numbers, and gives mixed results for higher Reynolds numbers. However, an increase in momentum in the wake is still observed across the board for medium angles of attack. The most significant separation reduction in these cases is observed for 12 degrees angle of attack at a Reynolds number of 1.32×10^5.

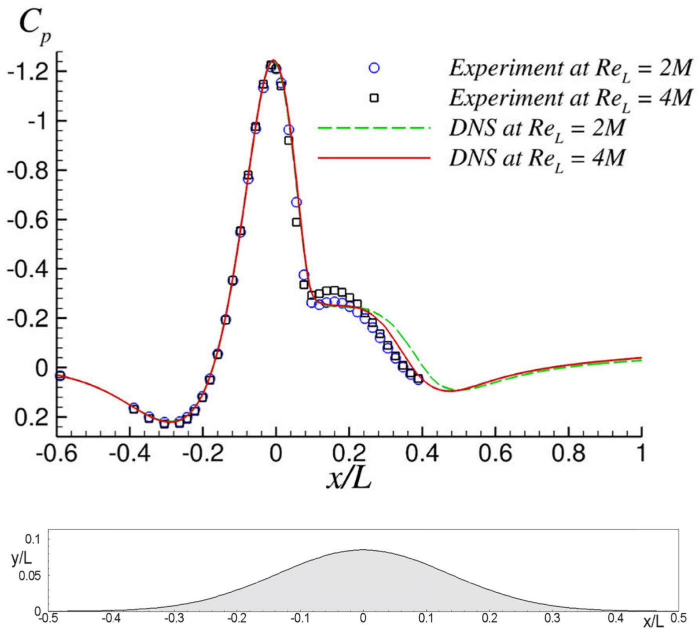

Figure 5.20: Example of an experimental and numerical pressure distribution of a flow over a bump. The Gaussian bump geometry is shown below the pressure figure (NB that the x axis locations do not align with the figure above). Data taken from Uzun & Malik [87]

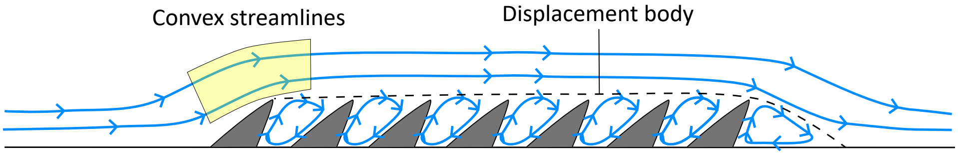

Figure 5.21: Diagram of the hypothesised mean flow around the kirigami, showing both the proposed hump effect and the roller-bearing effect

5.6. Controlled separation properties

Based on the last section, two example cases of interest are identified to investigate further. One at $\alpha = 12^o$, $Re = 1.32 \times 10^5$, and one at $\alpha = 14^o$, $Re = 1.98 \times 10^5$. These two cases exhibited the most significant change in separation under the influence of Kirigami.

5.6.1. Separation control effect on pressure

To investigate how the kirigami and the resulting change in the separation region has affected pressure, the pressure distributions are plotted for a select pair of cases in Figure 5.22. The pressure measurements for $Re = 1.98 \times 10^5$ were unavailable. Instead, the 14 degree angle of attack case is plotted at the same reynolds number as the 12 degree case, since these showed relatively similar results. Some filtering of extreme outliers was also applied to the circular and triangular case, leading to some missing points.

The first observation is that the pressure curve for triangular kirigami shows some significant anomalies near the suction peak. The suction peak, as well as part of the region behind it, seems to have been shifted down, and recovers sharply at about $0.3c$. This behaviour is untypical and most likely cannot be attributed to physical effects. It is more likely that this is due to improper zeroing of the pressure probes, so these points should be disregarded.

There is little difference between the clean case and the case with kirigami. For the case at 14 degrees, a minor delay can be seen in the point where the pressure gradient reaches zero, although this effect is quite subtle. This is complemented by a modest increase in the suction peak, which confirms a delay in separation, although more measurements should be done to confirm this effect. More detailed measurements are needed to obtain information about the pressure effects near the kirigami device

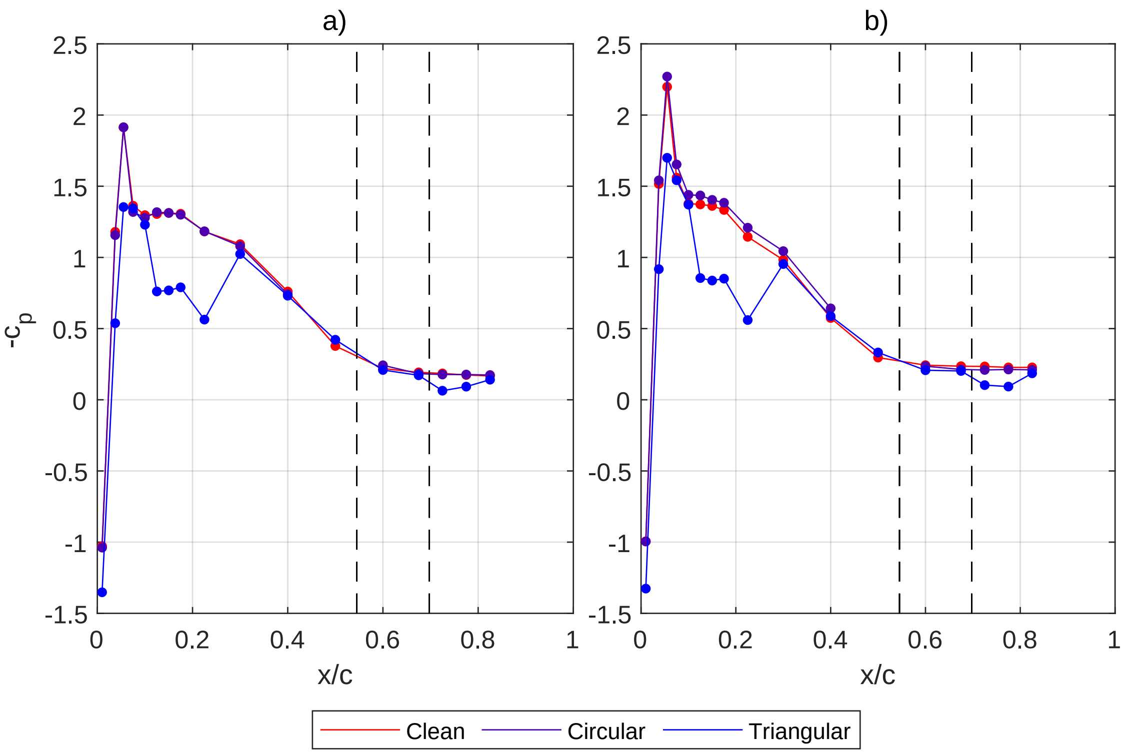

Figure 5.22: Comparison of suction side pressure distributions for a) $\alpha = 12^o$ and b) $\alpha = 14^o$, both at $Re = 1.32 \times 10^5$

that might affect separation. This could take the form of probe measurements right above the kirigami on a larger scale, zero pressure gradient experiment.

There is also a region of pressure recovery just behind the triangular kirigami. If this could be attributed to the kirigami, it would have also appeared for the circular kirigami. This means this is more likely to be an error with the zeroing of the pressure probes, considering that various probes were already excluded for triangular kirigami as significant outliers.

The pressure measurements near the kirigami show no change compared to the baseline, meaning there is no evidence that the kirigami functions as a blockage that modifies the pressure gradient. Although the resolution of the measurements is not large enough to draw any final conclusions, as well as the kirigami being on top of some of the probes, it cannot be concluded that the kirigami has an effect on the pressure gradient.

5.6.2. Separation region profiles

Figure 5.23 and Figure 5.24 show the mean velocity profile in s-direction (along the surface) for the cases mentioned above.

Both cases clearly show a reduction in separation. This is characterised by the simultaneous effect of the thinning of the shear layer and the reduction in reverse flow velocity. The effect of reduced flow reversal is more pronounced for the 12 degree case, whereas the effect of boundary layer thinning is more pronounced for the 14 degree case. Both of these effects persist over the entire surface.

Both Figure 2.19[51] and Figure 2.15[47] show that the primary mechanism of vortex generators involves moving momentum closer to the wall and will therefore result in less momentum away from the wall and thus a change in the shape of the velocity profile. In the abovementioned figures, no vertical displacement of horizontal momentum is observed, only a downscaling of the profile in both the momentum profiles. This shows that the separation control mechanism most likely cannot be attributed to the kirigami functioning as vortex generators and enhancing mixing through macro-scale vortices.

Furthermore, these figures show the difference between circular and triangular kirigami much more clearly. Of particular interest is the fact that at 12 degrees, the separation region is reduced more by the triangular kirigami, whereas for 14 degrees, the circular kirigami is more effective. With this in mind,

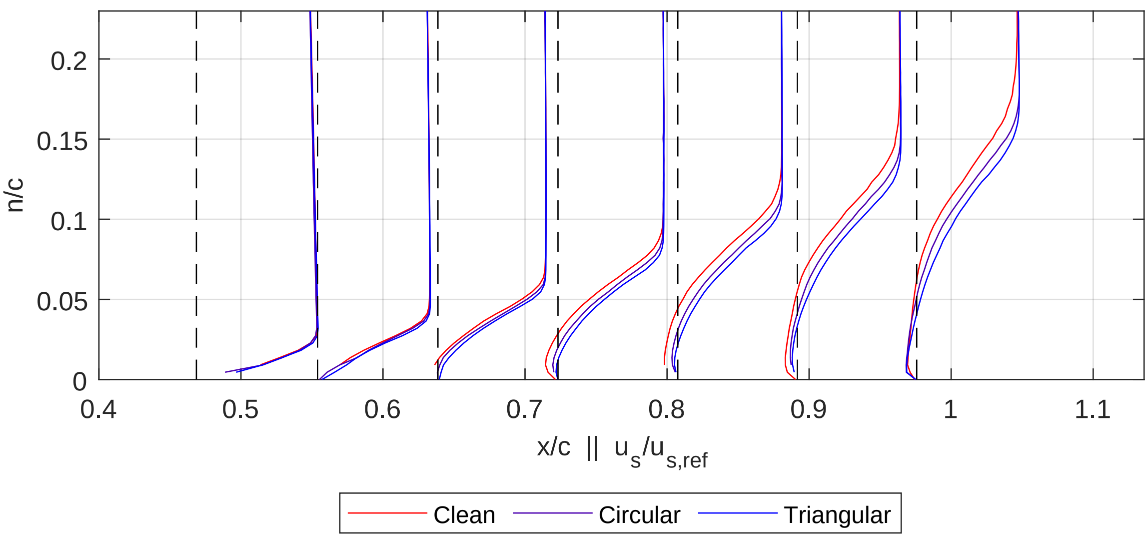

Figure 5.23: Mean velocity profiles of the separation region for $\alpha = 12^o$ at $Re = 1.32 \times 10^5$. Dashed lines indicate $u_s/u_{s,ref} = 0$ for each profile. $u_{s,ref}$ is a constant

it could be that multiple effects are happening simultaneously, as the same relative effectivity would be expected from the devices. From the present data, it is unclear which effects are responsible for this, and how they interact.

To investigate the possibility of the enhancement of turbulent mixing, one can investigate the Reynolds stresses. To get an indication of how the turbulent shear layer in the separation region develops over the airfoil, a similar profile plot as above is created, but for the R'_{xx}. Note that this R'_{xx} is calculated in the dewarped reference frame. However, this still allows for a valid comparison on vertical profiles, as the angle of rotation applied by the non-linear transformation is constant along the n-vector. Both cases are plotted in Figure 5.25 and Figure 5.26

For both profiles, the kirigami has significantly decreased the R'_{xx}, and also narrowed the turbulent layer. Despite R'_{yy} figures being omitted, similar results were found. This is indicative of decreased mixing, which conflicts with the hypothesis that turbulent mixing is enhanced. On the other hand, this is also consistent with the general properties of a turbulent separation region: a larger separation region is directly associated with increased Reynolds stresses. This multifaceted influence of controlled separation on Reynolds stresses and the resulting ambiguous causality makes it hard to distinguish the influence of Reynolds stresses on separation control.

Lastly, the R'_{xy} is of interest due to its contribution to the momentum balance (see Equation 2.9). This is shown in Figure 5.27.

As apparent, the data in R'_{xy} is of insufficent quality to make proper judgments on. This is potentially due to the statistics around this quantity not having fully resolved. This also makes it difficult to analyse the momentum and turbulence production and transport terms. In the future, the Reynolds stresses should be measured using more datapoints in the velocity signal.

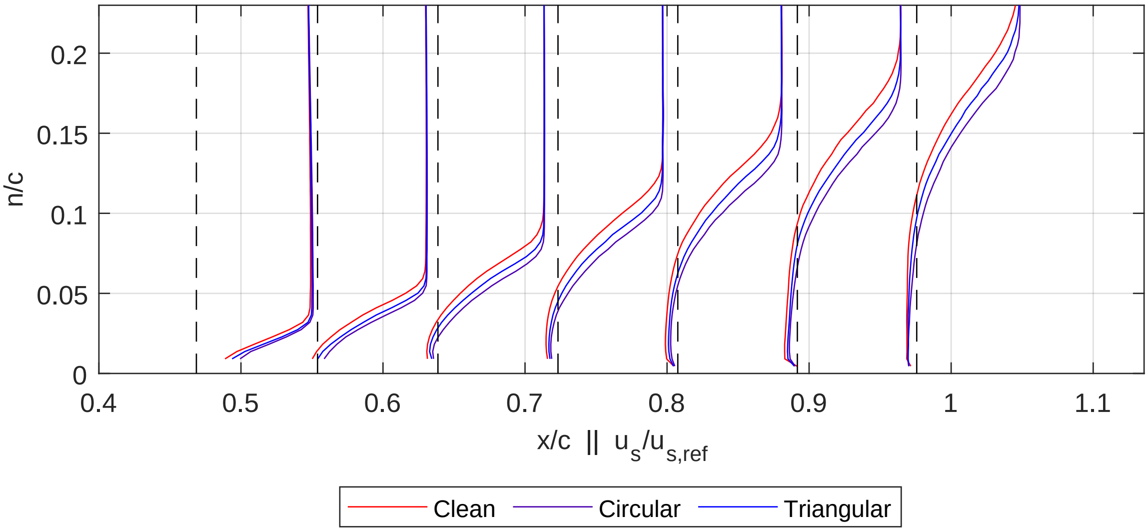

Figure 5.24: Mean velocity profiles of the separation region for $\alpha = 14^o$ at $Re = 1.98 \times 10^5$. Dashed lines indicate $u_s/u_{s,ref} = 0$ for each profile. $u_{s,ref}$ is a constant

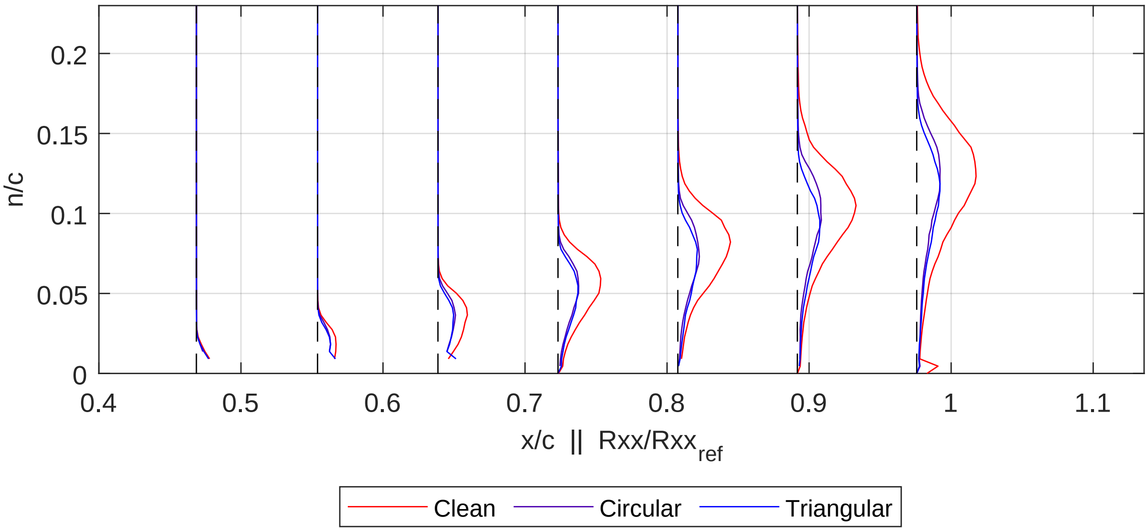

Figure 5.25: Mean xx Reynolds stress in profiles of the separation region for $\alpha = 12^o$ at $Re = 1.32 \times 10^5$. Dashed lines indicate $R_{xx}/R_{xx,ref} = 0$ for each profile. $R_{xx,ref}$ is a constant

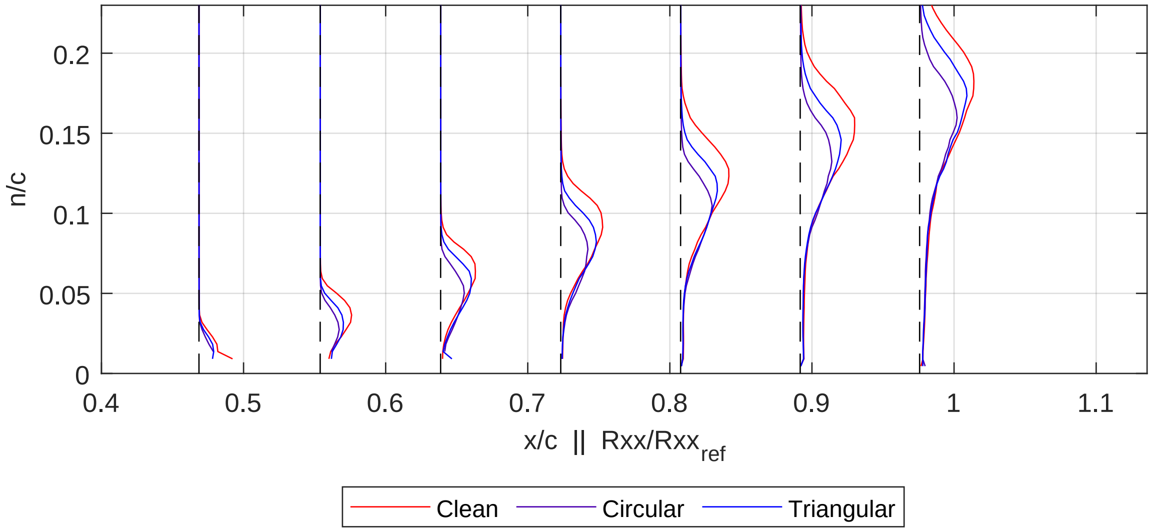

Figure 5.26: Mean xx Reynolds stress in profiles of the separation region for $\alpha = 14^o$ at $Re = 1.98 \times 10^5$. Dashed lines indicate $R_{xx}/R_{xx,ref} = 0$ for each profile. $R_{xx,ref}$ is a constant

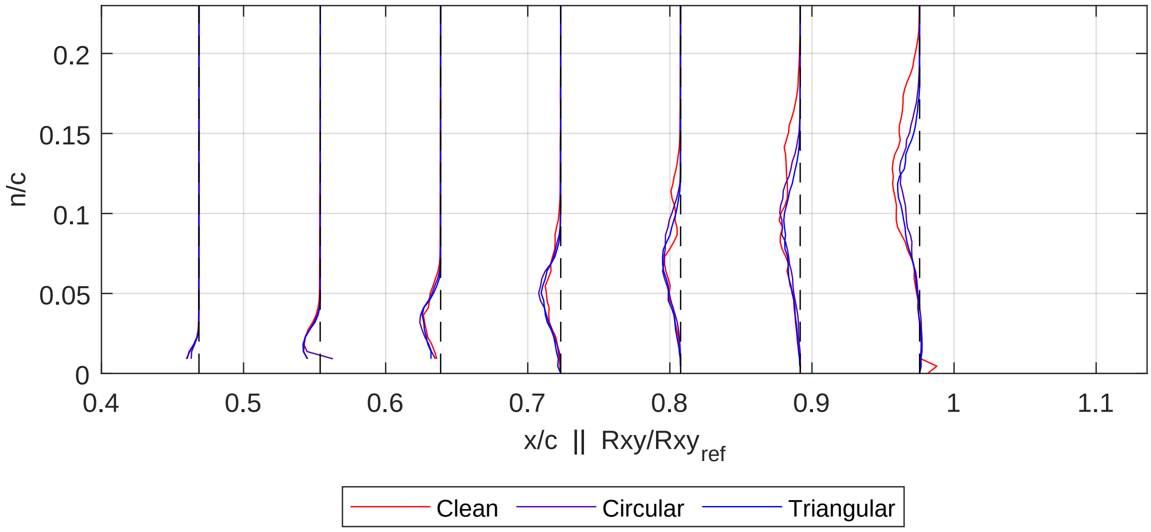

Figure 5.27: Mean xy Reynolds stress in profiles of the separation region for $\alpha = 12^o$ at $Re = 1.32 \times 10^5$. Dashed lines indicate $R_{xy}/R_{xy,ref} = 0$ for each profile. $R_{xy,ref}$ is a constant

5.6.3. Effect on separation region shape and intermittency

The literature has established a relation between the backflow and upstream momentum transport. In the absence of detailed frequency measurements, these can be characterised by the backflow coefficient. Figure 5.28 and Figure 5.29 show the isolines for $\gamma_{pu} = 0.99,\ 0.8,\ 0.5$, indicating ID, ITD and TD, as well as the mean flow reversal (detachment) boundary (isoline for $\overline{u}_s = 0$).

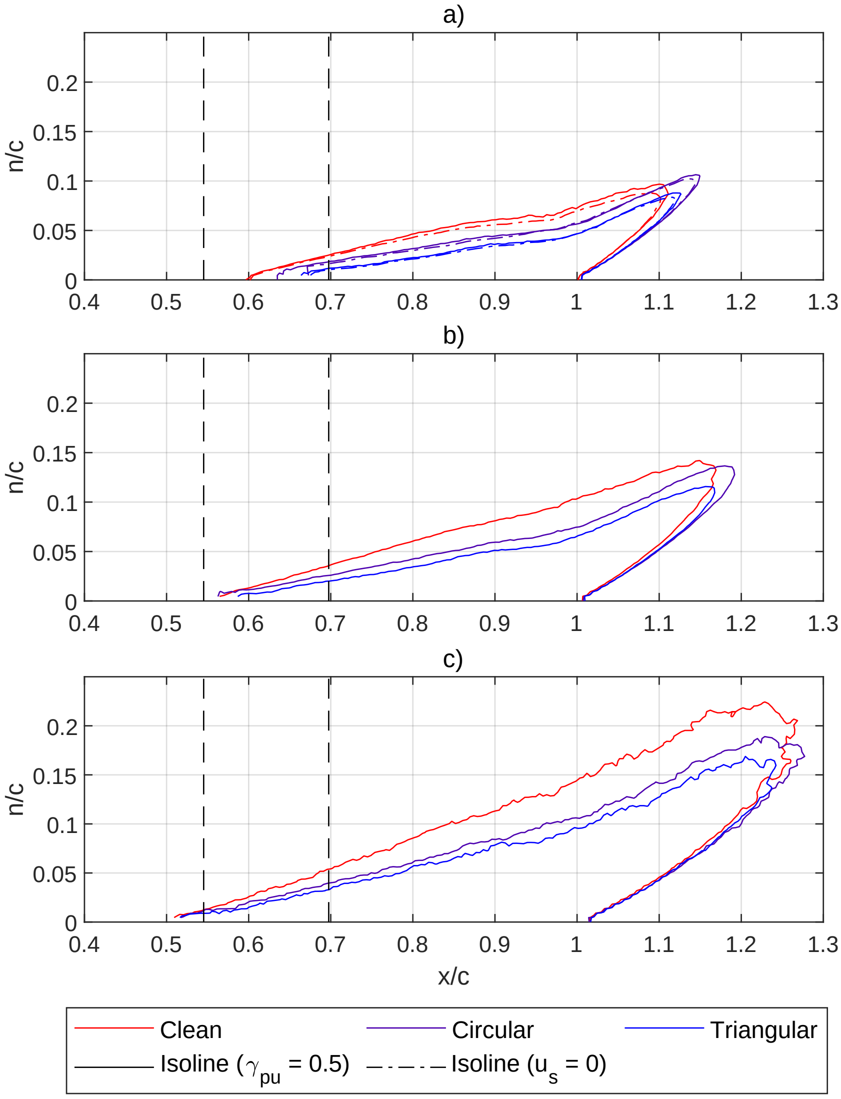

Figure 5.28: Backflow coefficient isolines for $\alpha = 12^o$ at $Re = 1.32 \times 10^5$ showing a) $\gamma_{pu} = 0.5$ (TD) with $\overline{u}_s = 0$, b) $\gamma_{pu} = 0.8$ (ITD), c) $\gamma_{pu} = 0.99$ (ID)

Both cases show a reduction in the size of the separation region due to the reduction in backflow. The transitory detachment regions also clearly show the change in the point of detachment. Furthermore, a strong overlap between the detachment region and the transitory detachment point emerges. The kirigami has different effects on the separation region shape for 12 degrees versus 14 degrees: at 12 degrees, the difference between the ITD and ID region of the clean case and the case with kirigami increases towards the trailing edge, whereas the difference stays more constant for the 14 degree case. This effect is observed in spite of the fact that the point of ID and ITD do not appear to move significantly under the presence of kirigami. Since the rapid growth of the boundary layer thickness is associated with the region between ID and ITD [40], it could be that the kirigami is interacting with the backflow near the surface. A reduction in backflow was also found in separation control research in shark skins (see section 2.6). In their study on actuating shark skin denticles, Lang et al. similarly attributed the reduction in separation and backflow to increased resistance to backflow in the separation onset due

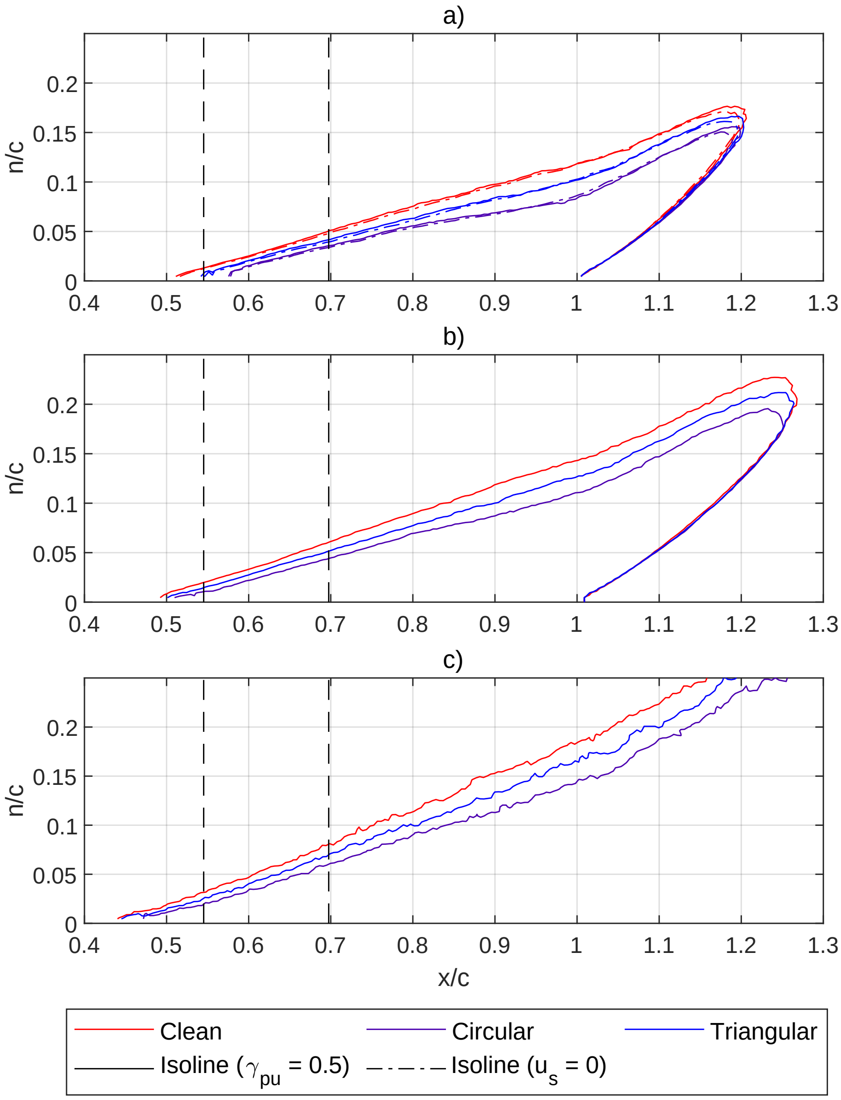

Figure 5.29: Backflow coefficient isolines for $\alpha = 14^o$ at $Re = 1.98 \times 10^5$ showing a) $\gamma_{pu} = 0.5$ with $\overline{u}_s = 0$, b) $\gamma_{pu} = 0.8$, c) $\gamma_{pu} = 0.99$.

to the shark scales[61].

Further evidence for this is the fact that the height scale of the kirigami at this angle of attack and Reynolds number ($h/\delta \approx 0.12$) is within the height of peak backflow at the onset of separation (see Figure 2.13b)[41]. It could be hypothesised that kirigami disrupts the turbulent structures responsible for the backflow in the separated region [40]. This would also provide further insight on the inhibited growth rate of the separation region at 12 degrees angle of attack. However, the present PIV results are incapable of measuring boundary layer details of this size, and also cannot capture the flow near the kirigami due to visual obstruction, so this cannot be further verified with the available data.

The same difference in separation reduction effectiveness between device shapes is also observed in these figures: triangular is more effective at 12 degrees angle of attack, circular is more effective at 14 degrees. This makes it unclear how these shapes affect the disruption of backflow. It is plausible that this swap in effectivity is due to an interaction between different separation reduction mechanisms, which can serve serve as a hypothesis for future research.

5.6.4. Uncertainty quantification

The uncertainty quantification methodology described in subsection 5.3.2 can be used to assess the validity of the aforementioned results.

Figure 5.30 shows an example of the uncertainty velocity field in x and y, using one of the example cases above. The uncertainty velocities are small compared to the flow, being of a magnitude less than 1% of the freestream velocity. It appears the largest source of uncertainty in x-direction is the turbulence in the upper shear layer of the separation region (compare with Figure 5.11b). This effect is much lower in the y component, where the largest source of uncertainty exists in the pressure-side wake behind the trailing edge. This wake, however, is not a factor in the quantities presented in this chapter. Furthermore, directly at the surface, the uncertainty is higher. This is presumably due to the reflections at the surface.

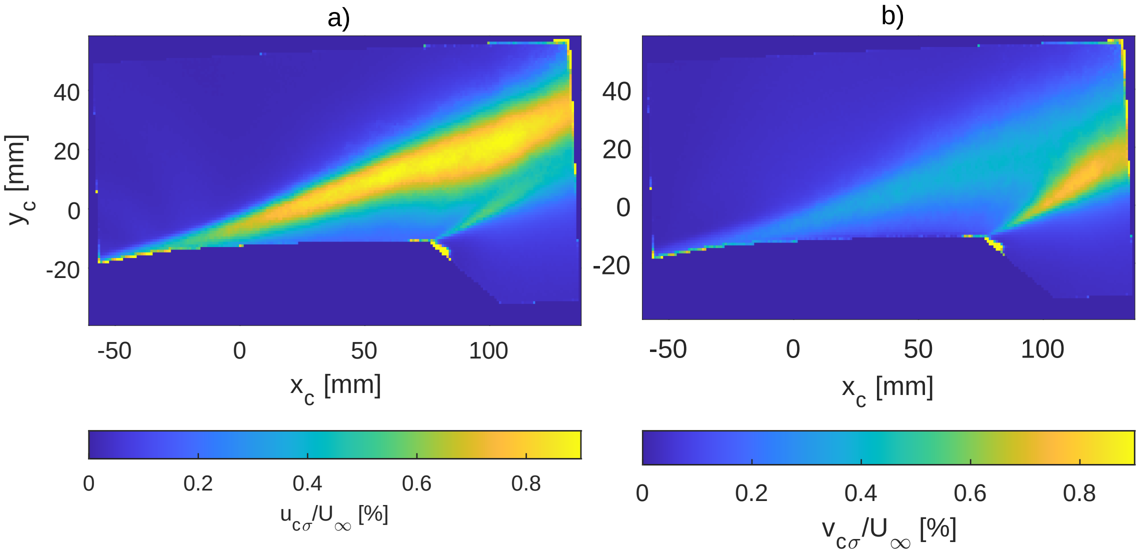

Figure 5.30: Color plots of the velocity uncertainty for $\alpha = 12^o$ at $Re = 1.32 \times 10^5$ in FOV coordinates. Both uncertainty components are plotted as a) u_c and b) v_c

To assess what effect these uncertainties have on the results, the contour lines of the mean flow field are shown for the clean case and a case with kirigami in Figure 5.31 and Figure 5.32. Additionally the contour plots for $\overline{u}+u_\sigma$ and $\overline{u}-u_\sigma$ are plotted to show how the velocity magnitudes change and displace with added uncertainty.

In Figure 5.31, the uncertainty bands for the x-component of the velocity are extremely small, and do not influence the resulting flow field much. For the y-component, the bands are larger and more chaotic, but the total offset is still small, and do not influence the results much since the y-component was not used for any of the parameters calculated in section 5.5.

It was established that the controlled separation case significantly reduced fluctuations in the shear layer. Figure 5.30 showed that these fluctuations are the primary cause of uncertainty in the flow field. It therefore makes sense that when kirigami is applied, the uncertainty decreases, as apparent from Figure 5.32. This establishes that the change in measured separation by kirigami devices is not influenced by uncertainty. This trend is also observed for other kirigami configurations for the cases described in this chapter. A collection for all relevant plots for these cases can be found in Appendix B.

This insignificant effect of the uncertainty on the flow field concludes that the PIV results obtained in this study are of sufficient quality to consider the conclusion that kirigami is able to reduce separation to be valid.

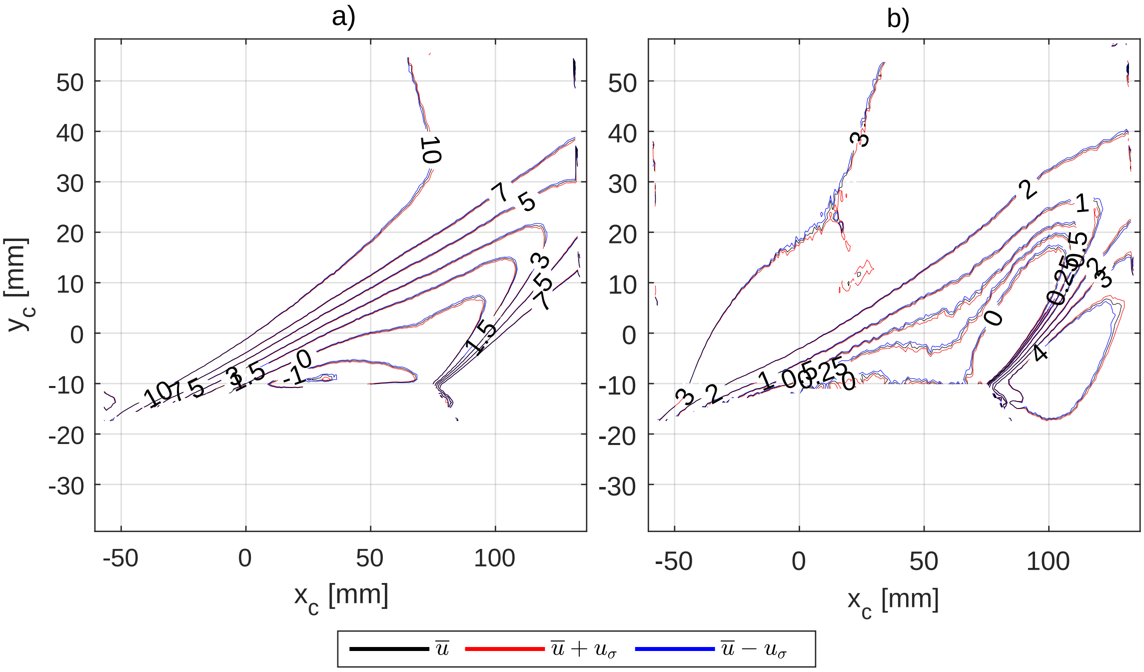

Figure 5.31: Contour plot of the mean flow components with uncertainty bounds $\alpha = 12^o$ at $Re = 1.32 \times 10^5$, clean configuration. The uncertainty components are plotted in a) u_c b) v_c

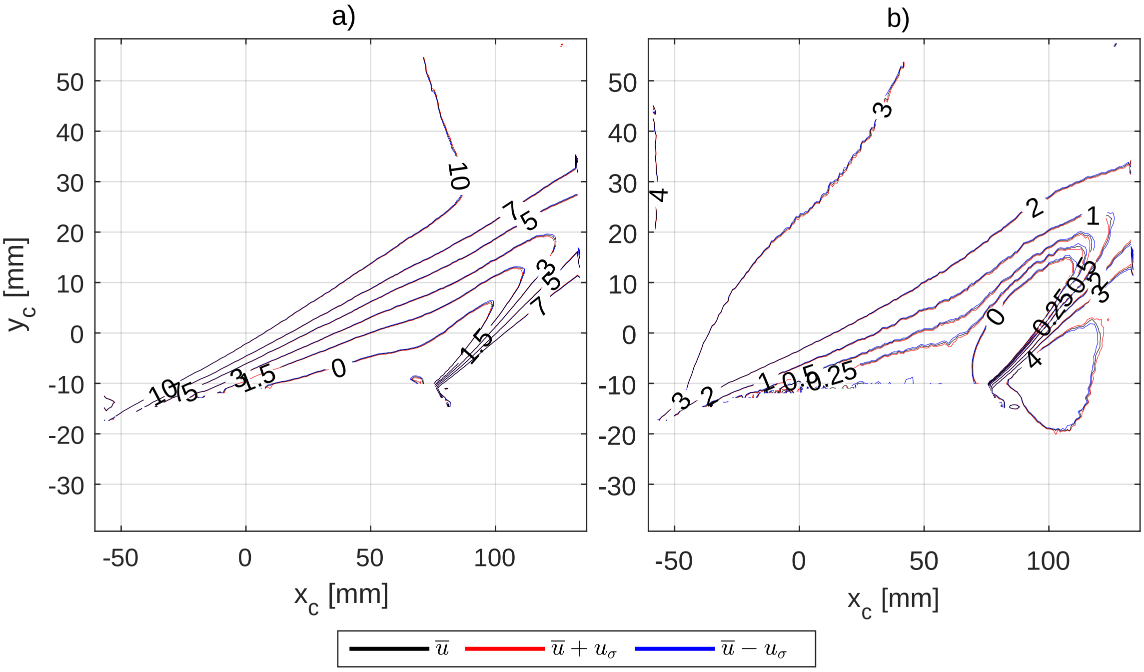

Figure 5.32: Contour plot of the mean flow components with uncertainty bounds $\alpha = 14^o$ at $Re = 1.98 \times 10^5$, triangular kirigami configuration. The uncertainty components are plotted in a) u_c b) v_c

6

Conclusion

The research conducted aimed to explore whether kirigami can be used for flow control. A literature survey gives the necessary background, based on which several research questions were posed. An investigation was conducted into the capabilities of FEM to predict extension length of a kirigami design, and how uniformity can be achieved. In a wind tunnel, these kirigami devices were tested on the suction side of a DU96 airfoil. Using PIV, the separation region was measured to see how kirigami would affect the separation.

The research performed in this thesis successfully resulted in a suitable design of a kirigami metasurface for the purpose of airfoil flow control. Furthermore, under some operating conditions, separation was reduced, leading to a significant drag reduction. This lays the basis for further research into kirigami as a flow control method. The conclusions to the research questions based on these results are given in this chapter. Lastly, these conclusions are supported with recommendations for further steps into kirigami research.

6.1. Kirigami design

The main research question concerning the design of kirigami was posed as follows:

What steps need to be taken to structurally design a kirigami metasurface suitable for separation control?

This question was investigated in chapter 4. The first part of this question concerned the ability of a finite-element method shell model to simulate the deployment height of the kirigami, which can be used to modify the scaling of the kirigami with respect to the boundary layer. A strong agreement was found between numerical and experimental results. The FEM model was able to both predict the quantitative height for a range of extensions, as well as predict the deployment behaviour practically one-on one.

This validation of the FEM allowed for the numerical investigation of non-uniform deployment in the form of a triangular front in the start and end rows of the kirigami. The root cause was reasoned to be the strong resistance to transverse buckling due to the strip, as buckling is the primary mechanism for the deployment of the kirigami elements. A solution was implemented that involved cutting slots in the front and aft strip of the kirigami. This alleviated the buckling stiffness in the strip, and allowed for much more uniform deployment. Therefore, for uniform deployment, the kirigami geometry should be such that the strip area does not restrict buckling, and rectangular strip cuts are an effective method in achieving this.

Leveraging some practical observations, a final design was made. The deployed kirigami device had to match an approximate height, so that it matches the scale of the boundary layer. The extension curve obtained from FEM, as well as the fact that a similar element aspect ratio was used directly translated this required height to the required dimensions of a single kirigami element. Further considerations, such as spanwise flow uniformity and minimising chordwise surface coverage finalised the rest of the design.

6.2. Separation control

The main research question concerning the design of kirigami was posed as follows:

How do tension-activated kirigami metasurfaces affect the flow separation on a DU96 airfoil in a wind-tunnel?

This question was investigated in chapter 5. Using PIV, the turbulent, trailing-edge separation on the airfoil was characterised. For the mean flow, the separation region was characterised using the height of the shear layer and the reverse flow boundary at the centre of the separation region, as well as the peak reverse mean flow velocity in the recirculation and the momentum in the wake behind the airfoil. Three regions of angle of attack can be categorised: low, medium and high. At low angles attack, from 6 to 10 degrees, separation is significantly aggravated by the kirigami. At medium angles of attack, from 12 to 16 degrees, signs of a reduction in separation are observed. For some cases, the presence of kirigami has resulted in a reduction in the overall size of the separation region, as well as a reduction in backflow, which has also resulted in a reduction in drag. At large angles of attack, beyond 18 degrees, the separation region is so large that the entire kirigami is encapsulated by the deeply separated region, which did not lead to significant changes to the separation behaviour.

The dynamics of the kirigami were captured in the form of the backflow coefficient and the Reynolds stresses. Reynolds stresses above the surface generally grow with increased separation and shrink with decreased separation, and the same pattern was found on controlled separation in this experiment. Although this implies that kirigami reduces turbulence, the effect of kirigami on the Reynolds stresses could not be disconnected from their effect on the entire separation region. The backflow was also found to be significantly reduced, but in different ways for different cases. For a detachment point just ahead of the kirigami device, the presence of the kirigami moves the detachment point further aft, without affecting the growth rate of the backflow region. For a detachment point located in the bounds of the kirigami device, the growth rate of the backflow region is reduced.

As for the working principle behind kirigami, it appears that the kirigami functions as a large-scale roughness at low angles of attack. The lack of separation makes for a incoming boundary layer, resulting in a larger h/δ and therefore a larger roughness. This, in turn causes an amplified momentum deficit in the boundary layer, which results in much earlier separation. For medium angles of attack, the flow near the kirigami causes the separation point to move forward. This could be attributed to an effect of pressure modification due to the kirigami serving as hump on the surface, or through internal flow phenomena on the kirigami reducing shear stresses, such as a 'roller-blade' effect caused by repeated separation regions. However, due to limitations in the measurement capabilities in the experiment and the challenges of measuring flow near the kirigami, this could not be fully verified. The existing evidence, furthermore, provides very limited support these theories. Instead, another theory is that the kirigami interferes with the backflow structures present between the ID and ITD point, which inhibit the rapid growth resulting from kirigami. This corresponds with the hypothesised separation control mechanism from other studies researching flow control through shark skin. Even though the exact separation reduction mechanism behind kirigami metasurfaces is hypothetical, this last hypothesis appears to be the most promising one for the present separation control mechanism. To the extent of the author's knowledge, this proposed mechanism of blocking backflow near the surface is not studied or understood in literature.

The difference between triangular and circular-shaped kirigami is mixed. Generally, at lower angles of attack separation is much more aggravated by the circular kirigami than the triangular one, which is likely to be driven by the increased frontal area of the circular kirigami devices at the same deployment height. The triangular-shaped kirigami also reduces at 12 degrees angle of attack compared to the circular one. This effect inverts at 14 degrees, where circular kirigami reduces separation the most. This dichotomy in effectiveness is cause to believe multiple effects are driving the reduction in separation, whose interaction should be kept in mind for future studies.

The relative scale of the of the kirigami devices varied between $h/\delta = 0.05$ and 0.25, being primarily a function of angle of attack. For the lower to medium angles of attack, this is similar to the scale of micro-vortex generators. However, due to their mode of operation, it is more akin to a large roughness. The low angles of attack appear to operate as a ’fully rough’ profile, where the large angles of attack operate as ’hydraulically smooth’. Typically, these roughness flows scale with the roughness Reynolds number $k_s^+ = \frac{k_s u_\tau}{\nu}$, which could not be determined in the present research. Although k_s^+ is typically a more appropriate scaling factor in these regimes than h/δ, the h/δ still served as an informative metric of how much influence the kirigami has on the separation region. For high h/δ, the kirigami significantly enhanced separation. For the medium angles of attack, some separation reduction was found, down to a h/δ of 0.07, where its effects diminish more. Similar scales in literature have also been found to influence separation. Below 0.07, the kirigami no longer has an influence on the separation region and is fully immersed.

The resulting separation reduction also influences the lift & drag on the airfoil. For the reduced separation cases, reverse flow was reduced, and as a result, the momentum deficit in the wake was reduced. The largest reduction occurred for 14 degrees angle of attack at $Re = 1.98 \times 10^5$ for circular-shaped kirigami, with up to 7% more momentum in the week, which means a significant drag reduction. Additionally, a minimal recovery of lift was found in the pressure distribution for the 14 degree case, where separation delay occurred. For other cases with controlled separation, no significant changes in lift were observed.

6.3. Recommendations

Although it was successfully shown that kirigami is capable of reducing the turbulent separation on an airfoil, some of the research questions did not result in a conclusive answer as to what the exact mechanism is, and what a potential optimisation of this flow control method would look like. It is prudent for the progress of this field to identify these characteristics, to enable more targeted approaches.

Future experimental research should attempt to investigate the flow nearby the kirigami using more detailed pressure measurements, and more detailed velocity field measurements nearby the kirigami. These will be able to further explain what the flow control mechanism of kirigami is. Toward the separation control mechanism of kirigami, several hypotheses were posed. However, one that was mentioned in other literature into separation control was that of the inhibition of the backflow near the surface. This has been proposed as a hypothesis but is not studied as a passive control mechanism in literature. Further testing should be done as to the validity of this hypothesis, as this could reveal a valuable knowledge gap in the field of passive turbulent separation control. It is furthermore useful to measure the reference boundary layer profile in more detail, particularly the viscous sublayer and a potential roughness defect layer, (and with that, the u_τ) as these give more information on the momentum deficit caused by the kirigami, as well as allow for roughness scaling methods of the kirigami height. This investigation into the kirigami operating as a roughness that aggravates separation is of equal significance, because a successful control strategy involves mitigating this adverse effect on top of enhancing the separation-reducing effects.

Another aspect that could contribute to kirigami separation control that was not highlighted in this thesis is that of 3D effects, as the nature of the experiment was inherently 2D. Turbulent separation has been said to exhibit 3D flow structures, and there is the potential for these effects to play a role in what is happening.

Considering an airfoil restricts the experiment to a specific set of pressure distributions, which are closely coupled to the boundary layer thickness, it is beneficial to also perform similar experiments in more controlled environments, where the user has more freedom in selecting the pressure gradient, as well as control the boundary layer thickness.

Alternatively, to circumvent some of the challenges involved in a wind tunnel experiment, such as optical access to the flow near a kirigami device, numerical methods can be used. Although the ability of CFD to predict turbulent separation is somewhat limited, recent advancements in the field of LES provide the opportunity for more accurate simulations. These numerical methods can be used to study the flow effects of kirigami in superior detail and smaller scales.

Based on this experiment, it appears the applications for kirigami on airfoils are as of yet limited, since the typical design goal for an airfoil is not only to delay stall and improve lift, but also to have the ability to operate in a large range of different conditions, based on inflow. Although there is potential for this, further, more practically-oriented research is needed to enable research into how kirigami can be used to enhance lift over airfoils. Instead, a more interesting application could be that of bluff bodies. Various sources in the literature survey in this thesis have investigated methods of drag reduction over bluff bodies, and kirigami has the potential to make significant contributions to this field.

References

[1] J. Anderson John D., “Ludwig Prandtl’s Boundary Layer,” *Physics Today*, vol. 58, no. 12, pp. 42–48, Dec. 2005, ISSN: 0031-9228. DOI: `10.1063/1.2169443`. eprint: `https://pubs.aip.org/physicstoday/article-pdf/58/12/42/9877446/42\_1\_online.pdf`. [Online]. Available: `https://doi.org/10.1063/1.2169443`.

[2] M. H. Hansen, “Aeroelastic instability problems for wind turbines,” *Wind Energy*, vol. 10, no. 6, pp. 551–577, 2007. DOI: `https://doi.org/10.1002/we.242`. eprint: `https://onlinelibrary.wiley.com/doi/pdf/10.1002/we.242`. [Online]. Available: `https://onlinelibrary.wiley.com/doi/abs/10.1002/we.242`.

[3] EASA. “Loss of control (loc-i) in general aviation.” (2016), [Online]. Available: `https://www.easa.europa.eu/en/downloads/18980/en` (visited on 11/27/2023).

[4] B. Scheichl, R. Bowles, and G. Pasias, “Developed liquid film passing a smoothed and wedge-shaped trailing edge: Small-scale analysis and the ‘teapot effect’ at large reynolds numbers,” *Journal of Fluid Mechanics*, vol. 926, A25, 2021. DOI: `10.1017/jfm.2021.612`.

[5] J. Katz, *Race Car Aerodynamics: Designing for Speed*. Cambridge, MA: Bentley Publishers, 2006, ISBN: 978-0-8376-0142-7.

[6] G. Sovran and D. Blaser, “A contribution to understanding automotive fuel economy and its limits,” *SAE Technical Papers*, 2003, Cited by: 41. DOI: `10.4271/2003-01-2070`. [Online]. Available: `https://www.scopus.com/inward/record.uri?eid=2-s2.0-85088339345&doi=10.4271%2f2003-01-2070&partnerID=40&md5=5cebc246a74e0521ac3d770a7b9897ac`.

[7] H. D. Taylor, “The elimination of diffuser separation by vortex generators,” United Aircraft Corporation, Report R-4012-3, Jun. 1947.

[8] J. C. Lin, “Review of research on low-profile vortex generators to control boundary-layer separation,” *Progress in Aerospace Sciences*, vol. 38, no. 4, pp. 389–420, 2002, ISSN: 0376-0421. DOI: `https://doi.org/10.1016/S0376-0421(02)00010-6`. [Online]. Available: `https://www.sciencedirect.com/science/article/pii/S0376042102000106`.

[9] S. Leibovich, “The structure of vortex breakdown,” *Annual Review of Fluid Mechanics*, vol. 10, no. Volume 10, 1978, pp. 221–246, 1978, ISSN: 1545-4479. DOI: `https://doi.org/10.1146/annurev.fl.10.010178.001253`. [Online]. Available: `https://www.annualreviews.org/content/journals/10.1146/annurev.fl.10.010178.001253`.

[10] R. Barrett and S. Farokhi, “Subsonic aerodynamics and performance of a smart vortex generator system,” *Journal of Aircraft*, vol. 33, no. 2, pp. 393–398, 1996. DOI: `10.2514/3.46950`. eprint: `https://doi.org/10.2514/3.46950`. [Online]. Available: `https://doi.org/10.2514/3.46950`.

[11] A. Lamoureux, K. Lee, M. Shlian, S. R. Forrest, and M. Shtein, “Dynamic kirigami structures for integrated solar tracking,” *Nature Communications*, vol. 6, no. 1, p. 8092, Sep. 2015, ISSN: 2041-1723. DOI: `10.1038/ncomms9092`. [Online]. Available: `https://doi.org/10.1038/ncomms9092`.

[12] Z. Liu, H. Du, J. Li, L. Lu, Z.-Y. Li, and N. X. Fang, “Nano-kirigami with giant optical chirality,” *Science Advances*, vol. 4, no. 7, eaat4436, 2018. DOI: `10.1126/sciadv.aat4436`. eprint: `https://www.science.org/doi/pdf/10.1126/sciadv.aat4436`. [Online]. Available: `https://www.science.org/doi/abs/10.1126/sciadv.aat4436`.

[13] L. Stein-Montalvo, L. Ding, M. Hultmark, S. Adriaenssens, and E. Bou-Zeid, “Kirigami-inspired wind steering for natural ventilation,” *Journal of Wind Engineering and Industrial Aerodynamics*, vol. 246, p. 105 667, 2024, ISSN: 0167-6105. DOI: `https://doi.org/10.1016/j.jweia.2024.105667`. [Online]. Available: `https://www.sciencedirect.com/science/article/pii/S0167610524000308`.

[14] H. Qiu, Y. Feng, Y. Gao, Z. Hong, and J. Tan, “Gradient design and fabrication methodology for interleaved self-locking kirigami panels,” *CAD Computer Aided Design*, vol. 166, 2024, Cited by: 1; All Open Access, Bronze Open Access. DOI: 10.1016/j.cad.2023.103632. [Online]. Available: https://www.scopus.com/inward/record.uri?eid=2-s2.0-85174744601&doi=10.1016%2fj.cad.2023.103632&partnerID=40&md5=bb747e3c9868780a6570f9149c6f7568.

[15] Y. Li, X. Song, H. Liu, and J. Yin, “Geometric mechanics of folded kirigami structures with tunable bandgap,” *Extreme Mechanics Letters*, vol. 49, p. 101 483, 2021, ISSN: 2352-4316. DOI: https://doi.org/10.1016/j.eml.2021.101483. [Online]. Available: https://www.sciencedirect.com/science/article/pii/S2352431621001851.

[16] R. M. Neville, F. Scarpa, and A. Pirrera, “Shape morphing kirigami mechanical metamaterials,” *Scientific Reports*, vol. 6, 2016, Cited by: 125; All Open Access, Gold Open Access, Green Open Access. DOI: 10.1038/srep31067. [Online]. Available: https://www.scopus.com/inward/record.uri?eid=2-s2.0-84981268304&doi=10.1038%2fsrep31067&partnerID=40&md5=90d25d0660dc1622bf1316e466a9f096.

[17] N. An, A. G. Domel, J. Zhou, A. Rafsanjani, and K. Bertoldi, “Programmable hierarchical kirigami,” *Advanced Functional Materials*, vol. 30, no. 6, p. 1 906 711, 2020. DOI: https://doi.org/10.1002/adfm.201906711. eprint: https://onlinelibrary.wiley.com/doi/pdf/10.1002/adfm.201906711. [Online]. Available: https://onlinelibrary.wiley.com/doi/abs/10.1002/adfm.201906711.

[18] T. Corrigan, P. Fleming, C. Eldredge, and D. Langer-Anderson, “Strong conformable structure via tension activated kirigami,” *Communications Materials*, vol. 4, no. 1, p. 31, 2023, ISSN: 2662-4443. DOI: 10.1038/s43246-023-00357-4. [Online]. Available: https://doi.org/10.1038/s43246-023-00357-4.

[19] L. Gamble, A. Lamoureux, and M. Shtein, “Multifunctional composite kirigami skins for aerodynamic control,” *Applied Physics Letters*, vol. 117, no. 25, p. 254 105, Dec. 2020, ISSN: 0003-6951. DOI: 10.1063/5.0024501. eprint: https://pubs.aip.org/aip/apl/article-pdf/doi/10.1063/5.0024501/14544110/254105_1_online.pdf. [Online]. Available: https://doi.org/10.1063/5.0024501.

[20] A. Rafsanjani, Y. Zhang, B. Liu, S. M. Rubinstein, and K. Bertoldi, “Kirigami skins make a simple soft actuator crawl,” *Science Robotics*, vol. 3, no. 15, eaar7555, 2018. DOI: 10.1126/scirobotics.aar7555. eprint: https://www.science.org/doi/pdf/10.1126/scirobotics.aar7555. [Online]. Available: https://www.science.org/doi/abs/10.1126/scirobotics.aar7555.

[21] S. Babaee, S. Pajovic, A. Rafsanjani, Y. Shi, K. Bertoldi, and G. Traverso, “Bioinspired kirigami metasurfaces as assistive shoe grips,” *Nature Biomedical Engineering*, vol. 4, no. 8, pp. 778–786, 2020, ISSN: 2157-846X. DOI: 10.1038/s41551-020-0564-3. [Online]. Available: https://doi.org/10.1038/s41551-020-0564-3.

[22] X. Wen, D. Wang, Z. Chen, F. Yang, C. Jiang, and Y. Liu, “Dynamic kirigami structures for wake flow control behind a circular cylinder,” *Physics of Fluids*, vol. 35, no. 1, p. 011 707, Jan. 2023, ISSN: 1070-6631. DOI: 10.1063/5.0130369. eprint: https://pubs.aip.org/aip/pof/article-pdf/doi/10.1063/5.0130369/19821498/011707_1_online.pdf. [Online]. Available: https://doi.org/10.1063/5.0130369.

[23] S. Sadanand Amin, “Additive manufacturing of kirigami metasurfaces,” thesis, 2022.

[24] M. A. Dias, M. P. McCarron, D. Rayneau-Kirkhope, *et al.*, “Kirigami actuators,” *Soft Matter*, vol. 13, no. 48, pp. 9087–9092, 2017. DOI: 10.1039/c7sm01693j.

[25] Y. Yang, M. A. Dias, and D. P. Holmes, “Multistable kirigami for tunable architected materials,” *Phys. Rev. Mater.*, vol. 2, p. 110 601, 11 Nov. 2018. DOI: 10.1103/PhysRevMaterials.2.110601. [Online]. Available: https://link.aps.org/doi/10.1103/PhysRevMaterials.2.110601.

[26] T. C. Shyu, P. F. Damasceno, P. M. Dodd, *et al.*, “A kirigami approach to engineering elasticity in nanocomposites through patterned defects,” *Nature Materials*, vol. 14, no. 8, pp. 785–789, 2015, ISSN: 1476-4660. DOI: 10.1038/nmat4327. [Online]. Available: https://doi.org/10.1038/nmat4327.

[27] S. Wildenborg, “Programming kirigami through fibre steering,” thesis, 2023.

[28] E. C. Maskell and R. A. E. (Britain), “Flow separation in three dimensions,” Royal Aircraft Establishment, Tech. Rep., 1955.

[29] M. Gad-el-Hak, *Separation Control*. Cambridge: Cambridge University Press, 2000, pp. 150–188. DOI: `10.1017/CBO9780511529535.010`.

[30] A. M. O. Smith, “High-lift aerodynamics,” *Journal of Aircraft*, vol. 12, no. 6, pp. 501–530, 1975. DOI: `10.2514/3.59830`. eprint: `https://doi.org/10.2514/3.59830`. [Online]. Available: `https://doi.org/10.2514/3.59830`.

[31] L. Prandtl, “Über flüssigkeitsbewegungen bei sehr kleiner reibung,” *Verhandlg. III. Intern. Math. Kongr. Heidelberg*, pp. 484–491, 1904.

[32] H. Schlichting, K. Gersten, E. Krause, and H. Oertel, *Boundary-Layer Theory*, 9th. Springer, 2017.

[33] F. M. White, *Viscous Fluid Flows*, 3rd. McGraw-Hill, 2006, ISBN: 9780072402315.

[34] F. H. Clauser, “Turbulent boundary layers in adverse pressure gradients,” *Journal of the Aeronautical Sciences*, vol. 21, no. 2, pp. 91–108, 1954. DOI: `10.2514/8.2938`. eprint: `https://doi.org/10.2514/8.2938`. [Online]. Available: `https://doi.org/10.2514/8.2938`.

[35] H. J. Herring and J. F. Norbury, “Some experiments on equilibrium turbulent boundary layers in favourable pressure gradients,” *Journal of Fluid Mechanics*, vol. 27, no. 3, pp. 541–549, 1967. DOI: `10.1017/S0022112067000527`.

[36] Y. Maciel, K.-S. Rossignol, and J. Lemay, “Self-similarity in the outer region of adverse-pressure-gradient turbulent boundary layers,” *AIAA Journal*, vol. 44, no. 11, pp. 2450–2464, 2006. DOI: `10.2514/1.19234`. eprint: `https://doi.org/10.2514/1.19234`. [Online]. Available: `https://doi.org/10.2514/1.19234`.

[37] T. v. Kármán, “Mechanische aenlichkeit und turbulenz,” *Nachrichten von der Gesellschaft der Wissenschaften zu Göttingen, Mathematisch-Physikalische Klasse*, vol. 1930, pp. 58–76, 1930. [Online]. Available: `http://eudml.org/doc/59299`.

[38] D. E. Coles and E. Hirst, “Computation of turbulent boundary layers,” 1968. [Online]. Available: `https://api.semanticscholar.org/CorpusID:61064940`.

[39] A. E. Perry and W. H. Schofield, “Mean velocity and shear stress distributions in turbulent boundary layers,” *The Physics of Fluids*, vol. 16, no. 12, pp. 2068–2074, Dec. 1973, ISSN: 0031-9171. DOI: `10.1063/1.1694267`. eprint: `https://pubs.aip.org/aip/pfl/article-pdf/16/12/2068/12358488/2068\_1\_online.pdf`. [Online]. Available: `https://doi.org/10.1063/1.1694267`.

[40] R. L. Simpson, “Turbulent boundary-layer separation,” *Annual Review of Fluid Mechanics*, vol. 21, no. 1, pp. 205–232, 1989. DOI: `10.1146/annurev.fl.21.010189.001225`. eprint: `https://doi.org/10.1146/annurev.fl.21.010189.001225`. [Online]. Available: `https://doi.org/10.1146/annurev.fl.21.010189.001225`.

[41] R. L. Simpson, Y.-T. Chew, and B. G. Shivaprasad, “The structure of a separating turbulent boundary layer. part 1. mean flow and reynolds stresses,” *Journal of Fluid Mechanics*, vol. 113, pp. 23–51, 1981. DOI: `10.1017/S002211208100339X`.

[42] V. A. Sandborn and C. Y. Liu, “On turbulent boundary-layer separation,” *Journal of Fluid Mechanics*, vol. 32, no. 2, pp. 293–304, 1968. DOI: `10.1017/S0022112068000728`.

[43] R. L. Simpson, J. H. Strickland, and P. W. Barr, “Features of a separating turbulent boundary layer in the vicinity of separation,” *Journal of Fluid Mechanics*, vol. 79, no. 3, pp. 553–594, 1977. DOI: `10.1017/S0022112077000329`.

[44] G. Godard and M. Stanislas, “Control of a decelerating boundary layer. part 1: Optimization of passive vortex generators,” *Aerospace Science and Technology*, vol. 10, no. 3, pp. 181–191, 2006, ISSN: 1270-9638. DOI: `https://doi.org/10.1016/j.ast.2005.11.007`. [Online]. Available: `https://www.sciencedirect.com/science/article/pii/S127096380500163X`.

[45] G. B. Schubauer and W. G. Spangenberg, “Forced mixing in boundary layers,” *Journal of Fluid Mechanics*, vol. 8, no. 1, pp. 10–32, 1960. DOI: `10.1017/S0022112060000372`.

[46] J. Lin, “Control of turbulent boundary-layer separation using micro-vortex generators,” in *30th Fluid Dynamics Conference*, 1999. DOI: `10.2514/6.1999-3404`.

[47] J. C. Lin, “Control of low-speed turbulent separated flow over a backward-facing ramp,” Doctor of Philosophy (PhD) Dissertation, Old Dominion University, Mechanical & Aerospace Engineering, 1992. DOI: 10.25777/40cn-pj52. [Online]. Available: https://digitalcommons.odu.edu/mae_etds/260.

[48] L. J. Lina and I. Reed Wilmer H, “A preliminary flight investigation of the effects of vortex generators on separation due to shock,” National Advisory Committee for Aeronautics, Nov. 1950.

[49] P. Ashill, J. Fulker, and K. Hackett, “Research at dera on sub boundary layer vortex generators (sbvgs),” in *39th Aerospace Sciences Meeting and Exhibit*. 2001. DOI: 10.2514/6.2001-887. eprint: https://arc.aiaa.org/doi/pdf/10.2514/6.2001-887. [Online]. Available: https://arc.aiaa.org/doi/abs/10.2514/6.2001-887.

[50] W. R. Pauley and J. K. Eaton, “Experimental study of the development of longitudinal vortex pairs embedded in a turbulent boundary layer,” *AIAA Journal*, vol. 26, no. 7, pp. 816–823, 1988. DOI: 10.2514/3.9974. eprint: https://doi.org/10.2514/3.9974. [Online]. Available: https://doi.org/10.2514/3.9974.

[51] K. P. Angele and F. Grewe, “Streamwise vortices in turbulent boundary layer separation control,” in *11th International Symposium on Application of Laser Techniques to Fluid Mechanics, Lisbon*, Experiments in Fluids, 2002.

[52] S. Lee, M. K. Goettke, E. Loth, J. Tinapple, and J. Benek, “Microramps upstream of an oblique-shock/boundary-layer interaction,” *AIAA Journal*, vol. 48, no. 1, pp. 104–118, 2010. DOI: 10.2514/1.41776. eprint: https://doi.org/10.2514/1.41776. [Online]. Available: https://doi.org/10.2514/1.41776.

[53] H. Babinsky, Y. Li, and C. W. P. Ford, “Microramp control of supersonic oblique shock-wave/boundary-layer interactions,” *AIAA Journal*, vol. 47, no. 3, pp. 668–675, 2009. DOI: 10.2514/1.38022. eprint: https://doi.org/10.2514/1.38022. [Online]. Available: https://doi.org/10.2514/1.38022.

[54] F. K. Lu, Q. Li, and C. Liu, “Microvortex generators in high-speed flow,” *Progress in Aerospace Sciences*, vol. 53, pp. 30–45, 2012, ISSN: 0376-0421. DOI: https://doi.org/10.1016/j.paerosci.2012.03.003. [Online]. Available: https://www.sciencedirect.com/science/article/pii/S0376042112000280.

[55] Z. Sun, F. F. J. Schrijer, F. Scarano, and B. W. van Oudheusden, “Decay of the supersonic turbulent wakes from micro-ramps,” *Physics of Fluids*, vol. 26, no. 2, p. 025 115, Feb. 2014, ISSN: 1070-6631. DOI: 10.1063/1.4866012. eprint: https://pubs.aip.org/aip/pof/article-pdf/doi/10.1063/1.4866012/16038587/025115_1_online.pdf. [Online]. Available: https://doi.org/10.1063/1.4866012.

[56] W. J. Gretta and C. R. Smith, “The Flow Structure and Statistics of a Passive Mixing Tab,” *Journal of Fluids Engineering*, vol. 115, no. 2, pp. 255–263, Jun. 1993, ISSN: 0098-2202. DOI: 10.1115/1.2910133. eprint: https://asmedigitalcollection.asme.org/fluidsengineering/article-pdf/115/2/255/5900152/255_1.pdf. [Online]. Available: https://doi.org/10.1115/1.2910133.

[57] M. S. Acarlar and C. R. Smith, “A study of hairpin vortices in a laminar boundary layer. part 1. hairpin vortices generated by a hemisphere protuberance,” *Journal of Fluid Mechanics*, vol. 175, pp. 1–41, 1987. DOI: 10.1017/S0022112087000272.

[58] M. Sajben, C. P. Chen, and J. C. Kroutil, “A new passive boundary-layer control device,” *AIAA Paper*, no. 76-700, 1976.

[59] A. M. Kuethe, “Boundary layer control of flow separation and heat exchange,” US3741285A, U.S. Patent No. 3741285, 1973.

[60] J. Lin, F. Howard, and G. Selby, “Exploratory study of vortex-generating devices for turbulent flow separation control,” in *29th Aerospace Sciences Meeting*. 1991. DOI: 10.2514/6.1991-42. eprint: https://arc.aiaa.org/doi/pdf/10.2514/6.1991-42. [Online]. Available: https://arc.aiaa.org/doi/abs/10.2514/6.1991-42.

[61] A. W. Lang, M. T. Bradshaw, J. A. Smith, *et al.*, “Movable shark scales act as a passive dynamic micro-roughness to control flow separation,” *Bioinspiration & Biomimetics*, vol. 9, no. 3, p. 036 017, 2014. DOI: 10.1088/1748-3182/9/3/036017.

[62] P. Motta, M. L. Habegger, A. Lang, R. Hueter, and J. Davis, “Scale morphology and flexibility in the shortfin mako isurus oxyrinchus and the blacktip shark carcharhinus limbatus,” *Journal of morphology*, vol. 273, no. 10, pp. 1096–1110, 2012. DOI: `10.1002/jmor.20047`.

[63] D. Bechert and W. Reif, “On the drag reduction of the shark skin,” in *23rd Aerospace Sciences Meeting*. 1985. DOI: `10.2514/6.1985-546`. eprint: `https://arc.aiaa.org/doi/pdf/10.2514/6.1985-546`. [Online]. Available: `https://arc.aiaa.org/doi/abs/10.2514/6.1985-546`.

[64] G. V. Lauder, D. K. Wainwright, A. G. Domel, J. C. Weaver, L. Wen, and K. Bertoldi, “Structure, biomimetics, and fluid dynamics of fish skin surfaces,” *Phys. Rev. Fluids*, vol. 1, p. 060 502, 6 Oct. 2016. DOI: `10.1103/PhysRevFluids.1.060502`. [Online]. Available: `https://link.aps.org/doi/10.1103/PhysRevFluids.1.060502`.

[65] M. Kadivar, D. Tormey, and G. McGranaghan, “A review on turbulent flow over rough surfaces: Fundamentals and theories,” *International Journal of Thermofluids*, vol. 10, p. 100 077, 2021, ISSN: 2666-2027. DOI: `https://doi.org/10.1016/j.ijft.2021.100077`. [Online]. Available: `https://www.sciencedirect.com/science/article/pii/S266620272100015X`.

[66] P. W. Bearman and J. K. Harvey, “Golf ball aerodynamics,” *Aeronautical Quarterly*, vol. 27, no. 2, pp. 112–122, 1976. DOI: `10.1017/S0001925900007617`.

[67] N. Timmer and L. Veldhuis, “The impact of skinsuit zigzag tape turbulators on speed skating performance,” *Applied Sciences*, vol. 11, no. 3, 2021, ISSN: 2076-3417. DOI: `10.3390/app11030988`. [Online]. Available: `https://www.mdpi.com/2076-3417/11/3/988`.

[68] B. Song and J. K. Eaton, “The effects of wall roughness on the separated flow over a smoothly contoured ramp,” *Experiments in Fluids*, vol. 33, pp. 38–46, 2002. DOI: `10.1007/s00348-002-0411-1`.

[69] W. Wu and U. Piomelli, “Effects of surface roughness on a separating turbulent boundary layer,” *Journal of Fluid Mechanics*, vol. 841, pp. 552–580, 2018. DOI: `10.1017/jfm.2018.101`.

[70] C. F. Colebrook, C. M. White, and G. I. Taylor, “Experiments with fluid friction in roughened pipes,” *Proceedings of the Royal Society of London. Series A - Mathematical and Physical Sciences*, vol. 161, no. 906, pp. 367–381, 1937. DOI: `10.1098/rspa.1937.0150`. eprint: `https://royalsocietypublishing.org/doi/pdf/10.1098/rspa.1937.0150`. [Online]. Available: `https://royalsocietypublishing.org/doi/abs/10.1098/rspa.1937.0150`.

[71] F. Howard, W. Goodman, and M. Walsh, “Axisymmetric bluff-body drag reduction using circumferential grooves,” in *Applied Aerodynamics Conference*. 1983. DOI: `10.2514/6.1983-1788`. eprint: `https://arc.aiaa.org/doi/pdf/10.2514/6.1983-1788`. [Online]. Available: `https://arc.aiaa.org/doi/abs/10.2514/6.1983-1788`.

[72] F. G. Howard and W. L. Goodman, “Axisymmetric bluff-body drag reduction through geometrical modification,” *Journal of Aircraft*, vol. 22, no. 6, pp. 516–522, 1985. DOI: `10.2514/3.45158`. eprint: `https://doi.org/10.2514/3.45158`. [Online]. Available: `https://doi.org/10.2514/3.45158`.

[73] F. G. Howard and W. L. Goodman, “Drag reduction on a bluff body at yaw angles to 30 degrees,” *Journal of Spacecraft and Rockets*, vol. 24, no. 2, pp. 179–181, 1987. DOI: `10.2514/3.25893`. eprint: `https://doi.org/10.2514/3.25893`. [Online]. Available: `https://doi.org/10.2514/3.25893`.

[74] E. Mercker and J. Wiedemann, “On the correction of interference effects in open jet wind tunnels,” *SAE Transactions*, vol. 105, pp. 795–809, 1996, Accessed 24 Aug. 2025. [Online]. Available: `http://www.jstor.org/stable/44720797`.

[75] J. B. Barlow, J. Rae William H., and A. Pope, *Low-Speed Wind Tunnel Testing*, 3rd ed. New York: Wiley-Interscience, 1999, ISBN: 978-0471557746.

[76] E. Maskell, “A theory of the blockage effects on bluff bodies and stalled wings in a closed wind tunnel,” Aeronautical Research Council, London, Reports & Memoranda No. 3400, 1963.

[77] B. F. R. Ewald, Ed., *AGARDograph 336: Wind Tunnel Wall Corrections*. North Atlantic Treaty Organization, 1998.

[78] Y. Zhang, F. Avallone, and S. Watson, "Leading edge erosion detection for a wind turbine blade using far-field aerodynamic noise," *Applied Acoustics*, vol. 207, p. 109 365, 2023, ISSN: 0003-682X. DOI: `https://doi.org/10.1016/j.apacoust.2023.109365`. [Online]. Available: `https://www.sciencedirect.com/science/article/pii/S0003682X23001639`.

[79] A. Suryadi and M. Herr, "Wall pressure spectra on a du96-w-180 profile from low to pre-stall angles of attack," *21st AIAA/CEAS Aeroacoustics Conference*, 2015. DOI: `10.2514/6.2015-2688`. [Online]. Available: `https://arc.aiaa.org/doi/abs/10.2514/6.2015-2688`.

[80] R. Merino-Martínez, A. Rubio Carpio, L. T. Lima Pereira, *et al.*, "Aeroacoustic design and characterization of the 3d-printed, open-jet, anechoic wind tunnel of delft university of technology," *Applied Acoustics*, vol. 170, p. 107 504, 2020, ISSN: 0003-682X. DOI: `https://doi.org/10.1016/j.apacoust.2020.107504`. [Online]. Available: `https://www.sciencedirect.com/science/article/pii/S0003682X20306083`.

[81] R. D. Keane and R. J. Adrian, "Optimization of particle image velocimeters: II. multiple pulsed systems," *Measurement Science and Technology*, vol. 2, no. 10, pp. 963–974, 1991, ISSN: 0957-0233. DOI: `10.1088/0957-0233/2/10/013`.

[82] A. Sciacchitano, "Uncertainty quantification in particle image velocimetry," *Measurement Science and Technology*, vol. 30, no. 9, p. 092 001, 2019. DOI: `10.1088/1361-6501/ab1db8`.

[83] A. Sciacchitano, B. Wieneke, and F. Scarano, "Piv uncertainty quantification by image matching," *Measurement Science and Technology*, vol. 24, no. 4, p. 045 302, 2013. DOI: `10.1088/0957-0233/24/4/045302`.

[84] B. Wieneke, "Piv uncertainty quantification from correlation statistics," *Measurement Science and Technology*, vol. 26, no. 7, p. 074 002, 2015. DOI: `10.1088/0957-0233/26/7/074002`.

[85] J. D. Anderson, *Fundamentals of Aerodynamics*, 6th. New York: McGraw-Hill Education, 2017, ISBN: 978-1259129919.

[86] W. Terra, A. Sciacchitano, and F. Scarano, "Aerodynamic drag of a transiting sphere by large-scale tomographic-piv," *Experiments in Fluids*, vol. 58, no. 6, p. 83, 2017. DOI: `10.1007/s00348-017-2331-0`.

[87] A. Uzun and M. R. Malik, "Direct numerical simulation of flow past a gaussian bump at a high reynolds number," *Theoretical and Computational Fluid Dynamics*, vol. 39, p. 30, 2025. DOI: `10.1007/s00162-025-00749-x`.

A

Separation control effectiveness - supplementary plots

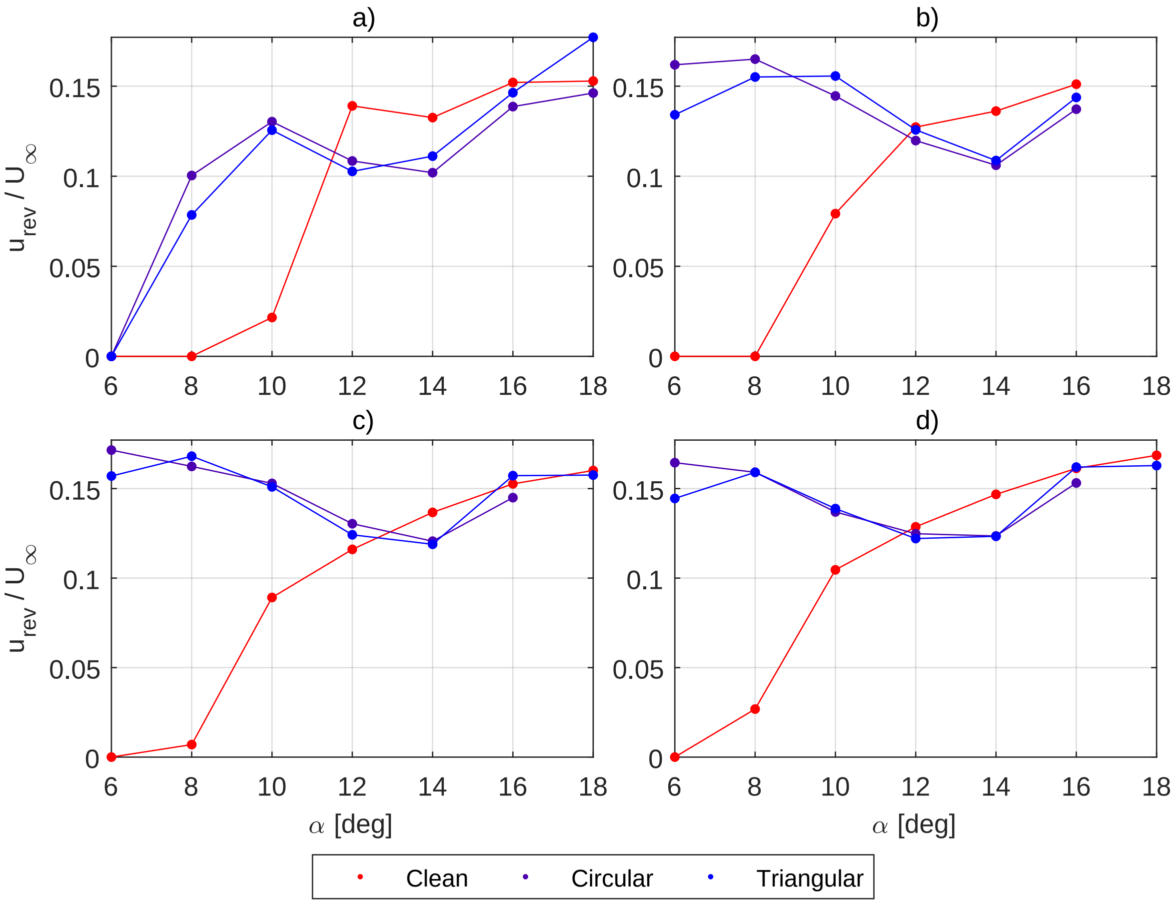

Figure A.1: Maximum reverse flow magnitude in the separation bubble at a) $Re = 1.32 \times 10^5$, b) $Re = 2.64 \times 10^5$, c) $Re = 3.30 \times 10^5$, and d) $Re = 3.96 \times 10^5$

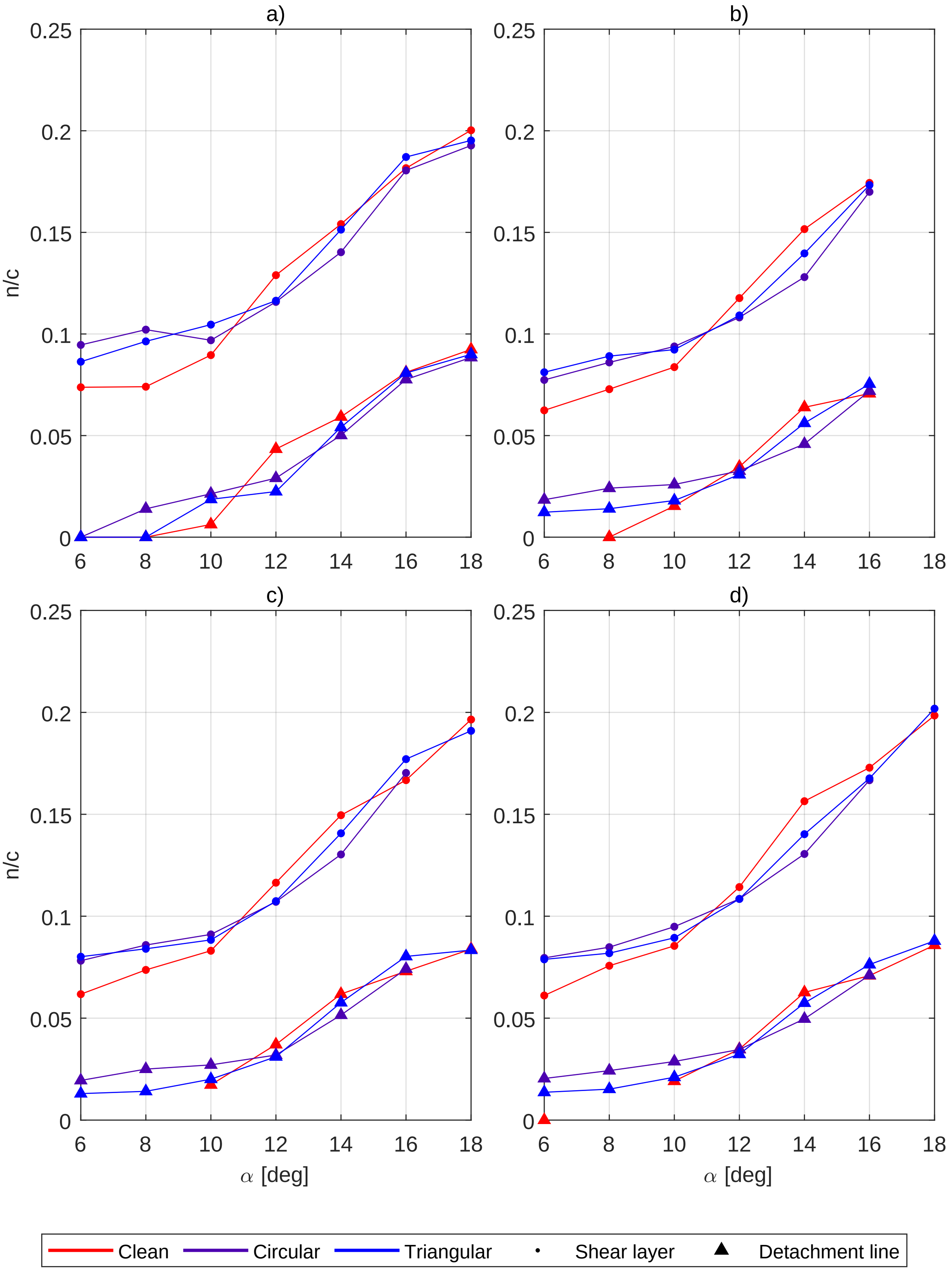

Figure A.2: Height of the shear layer and separation bubble measured half-way inside the separation bubble a) $Re = 1.32 \times 10^5$, b) $Re = 2.64 \times 10^5$, c) $Re = 3.30 \times 10^5$, and d) $Re = 3.96 \times 10^5$

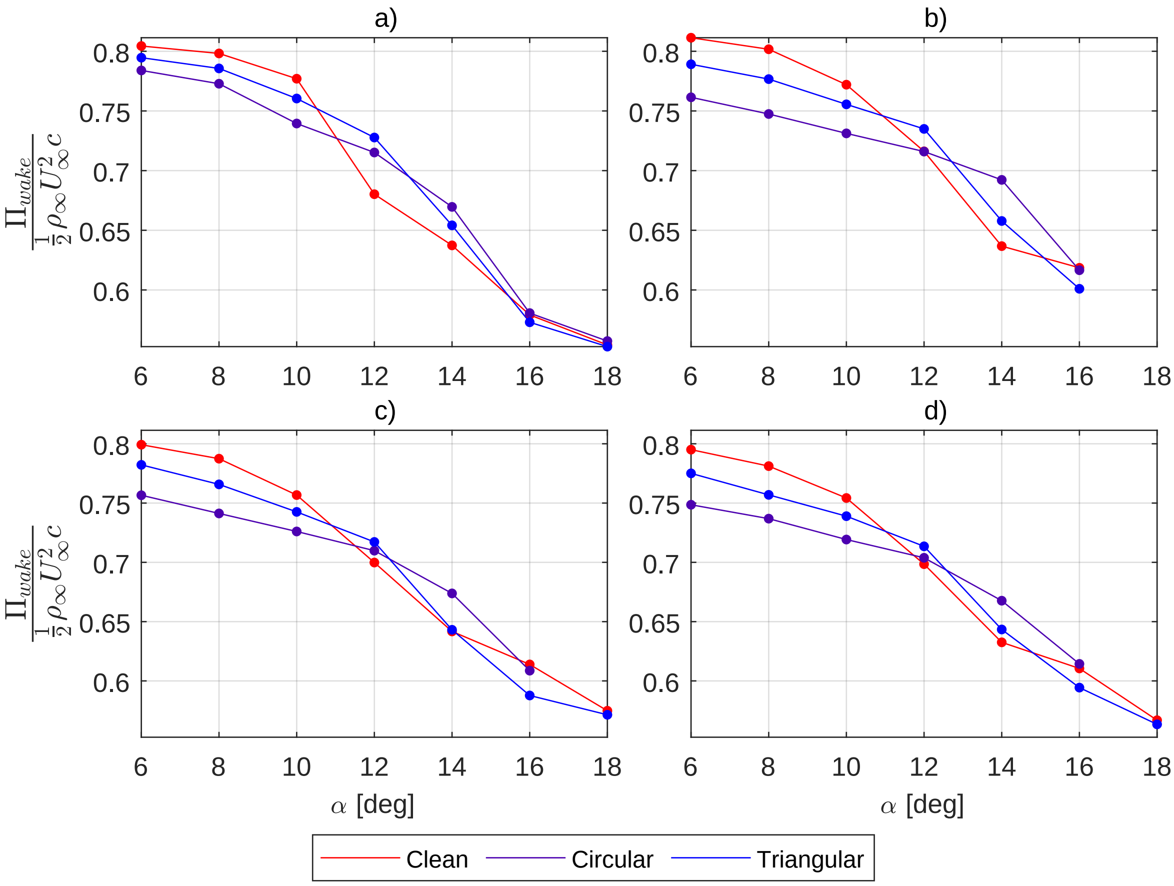

Figure A.3: Momentum outflow at the wake boundary at a) $Re = 1.32 \times 10^5$, b) $Re = 2.64 \times 10^5$, c) $Re = 3.30 \times 10^5$, and d) $Re = 3.96 \times 10^5$

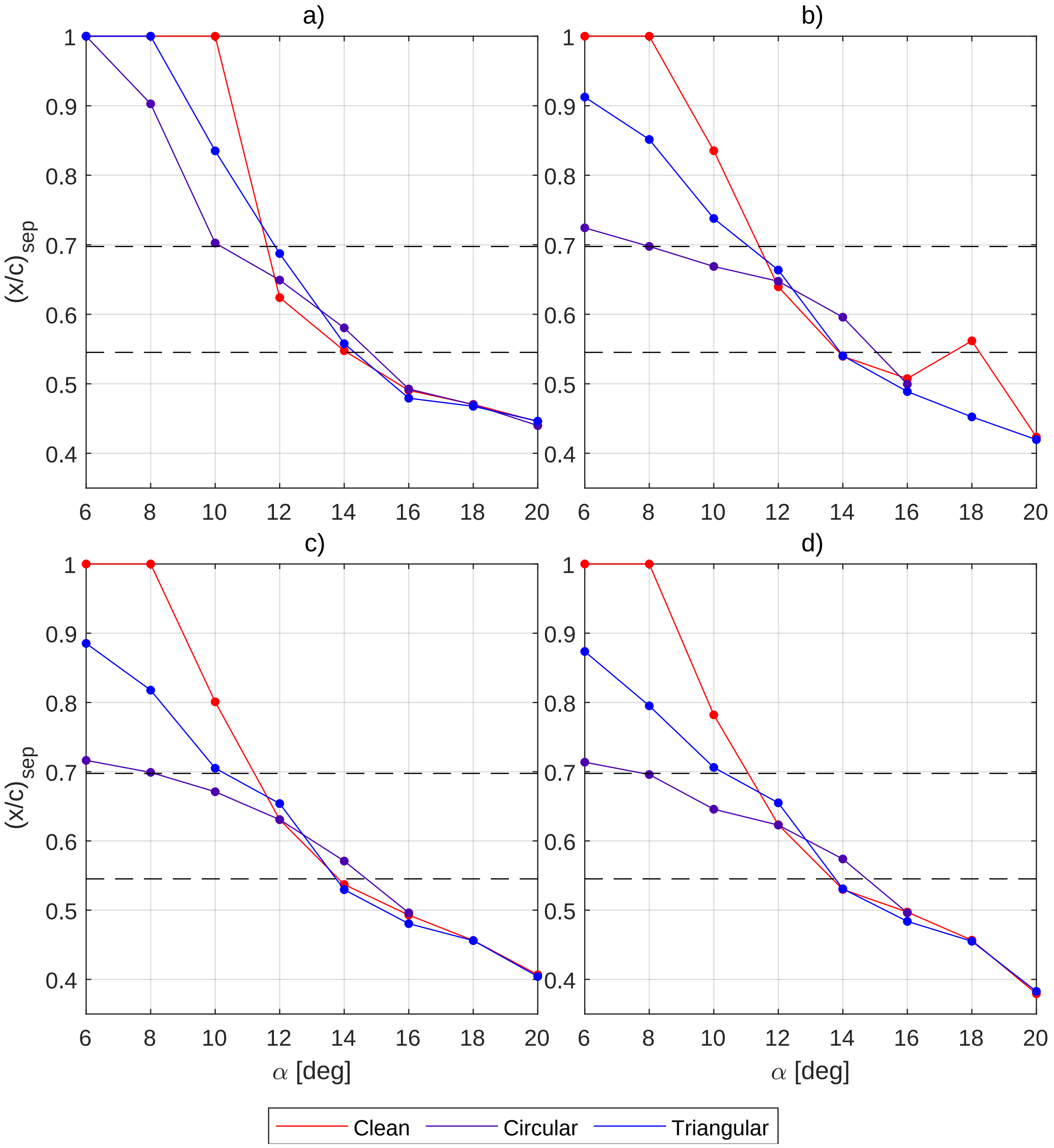

Figure A.4: Detachment point for different angles of attack at a) $Re = 1.32 \times 10^5$, b) $Re = 2.64 \times 10^5$, c) $Re = 3.30 \times 10^5$, and d) $Re = 3.96 \times 10^5$

B

Uncertainty quantification - supplementary plots

B.1. Clean configuration color plots

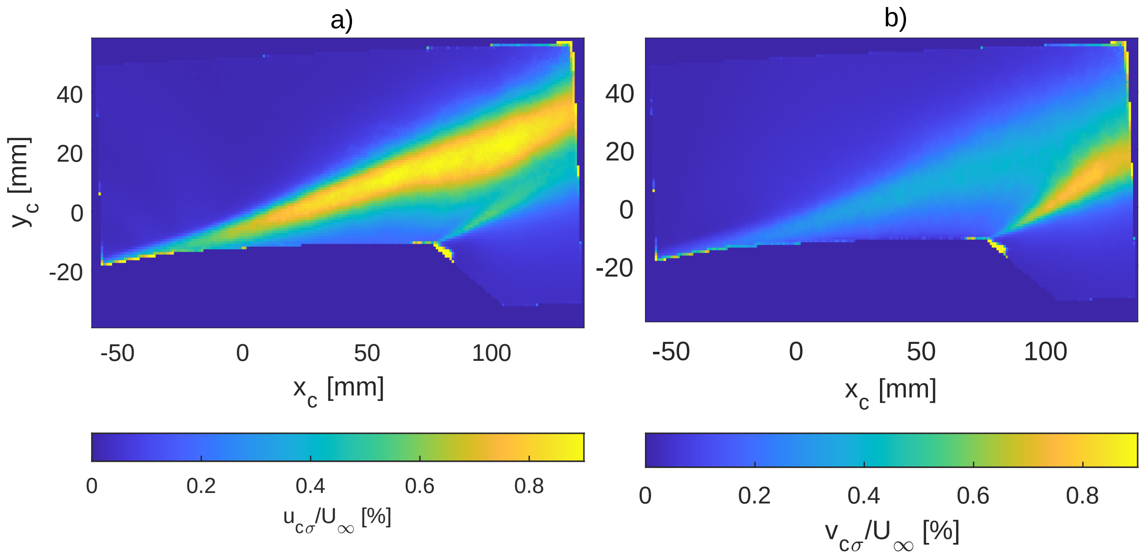

Figure B.1: Color plots of the velocity uncertainty for $\alpha = 12^o$ at $Re = 1.32 \times 10^5$ in FOV coordinates. Both uncertainty components are plotted as a) u_c and b) v_c

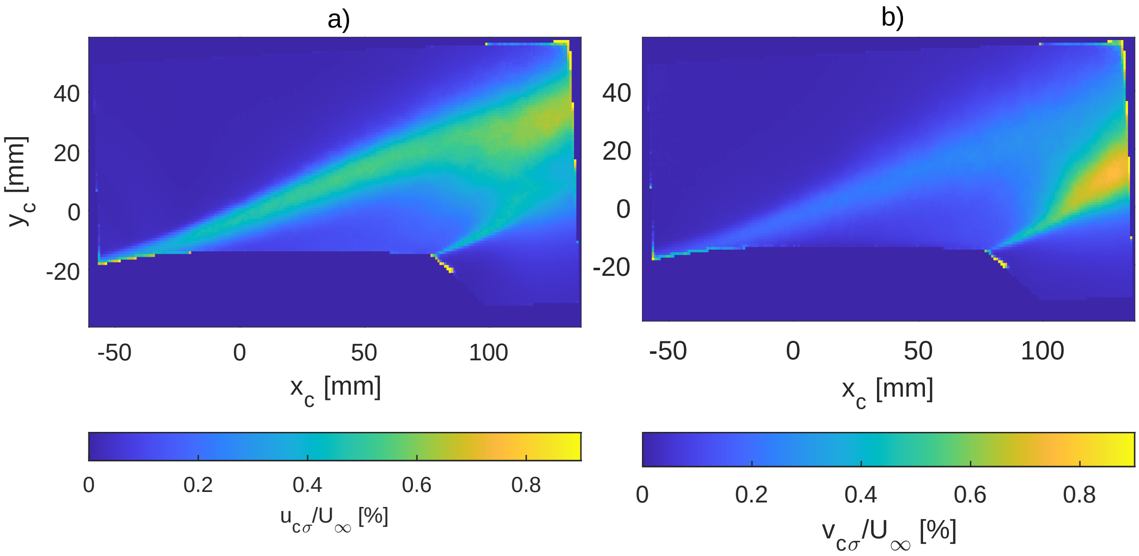

Figure B.2: Color plots of the velocity uncertainty for $\alpha = 14^o$ at $Re = 1.98 \times 10^5$ in FOV coordinates. Both uncertainty components are plotted as a) u_c and b) v_c

B.2. Uncertainty bounds contour plots - all cases

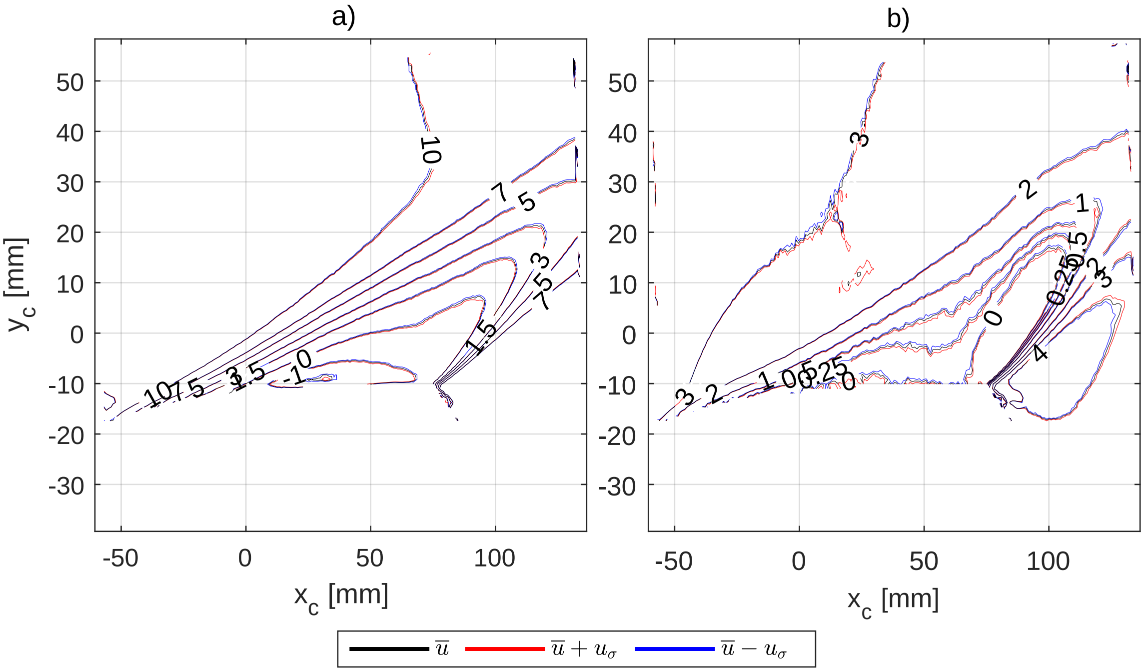

Figure B.3: Contour plot of the mean flow components with uncertainty bounds $\alpha = 12^o$ at $Re = 1.32 \times 10^5$, clean configuration. The uncertainty components are plotted in a) u_c b) v_c

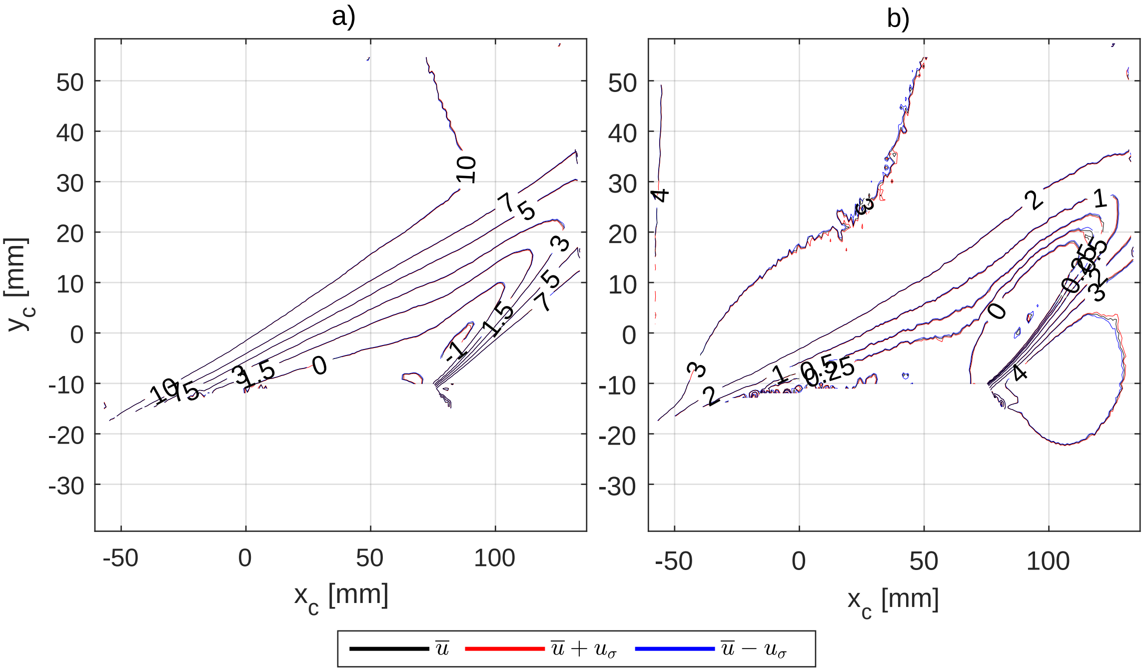

Figure B.4: Contour plot of the mean flow components with uncertainty bounds $\alpha = 12^o$ at $Re = 1.32 \times 10^5$, circular configuration. The uncertainty components are plotted in a) u_c b) v_c

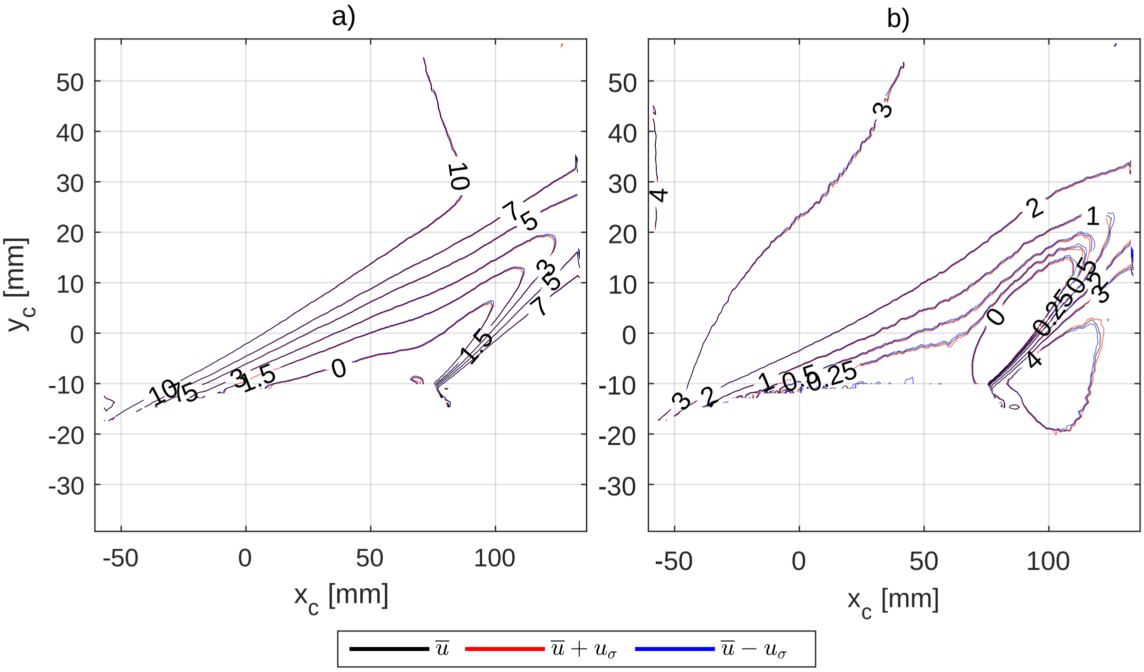

Figure B.5: Contour plot of the mean flow components with uncertainty bounds $\alpha = 14^o$ at $Re = 1.98 \times 10^5$, triangular kirigami configuration. The uncertainty components are plotted in a) u_c b) v_c

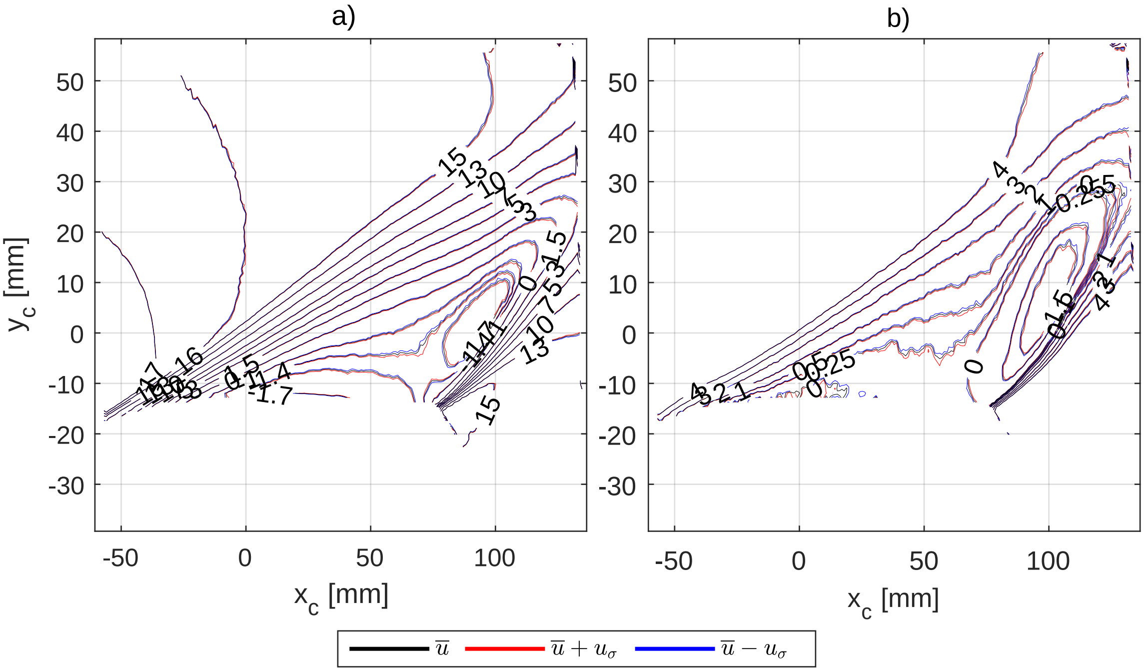

Figure B.6: Contour plot of the mean flow components with uncertainty bounds $\alpha = 14^o$ at $Re = 1.98 \times 10^5$, clean configuration. The uncertainty components are plotted in a) u_c b) v_c

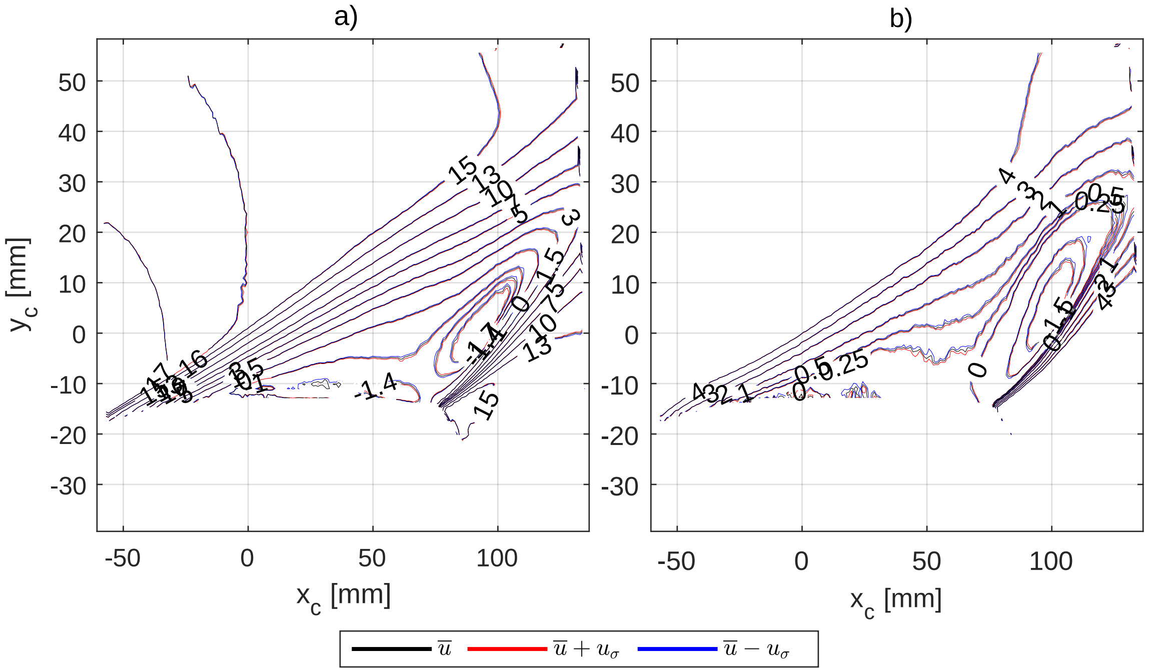

Figure B.7: Contour plot of the mean flow components with uncertainty bounds $\alpha = 14^o$ at $Re = 1.98 \times 10^5$, triangular kirigami configuration. The uncertainty components are plotted in a) u_c b) v_c

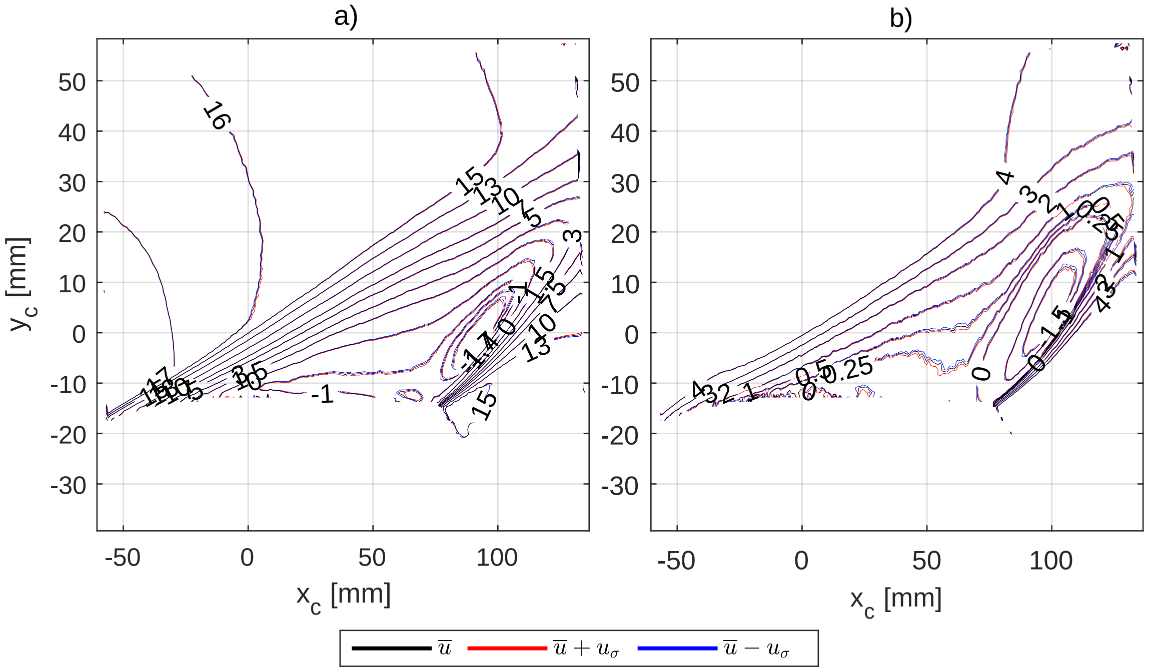

Figure B.8: Contour plot of the mean flow components with uncertainty bounds $\alpha = 14^o$ at $Re = 1.98 \times 10^5$, triangular kirigami configuration. The uncertainty components are plotted in a) u_c b) v_c